# UC San Diego

## UC San Diego Electronic Theses and Dissertations

### Title

Computational and Experimental Investigation of Vortex Cooling of a Gas Turbine Blade Using 3-D Stereo-Particle Image Velocimetry and Liquid Crystals

### Permalink

https://escholarship.org/uc/item/2cf8s3cp

### Author

Galeana, Daisy

### Publication Date

2022

Peer reviewed|Thesis/dissertation

eScholarship.org Powered by the California Digital Library
University of California

UNIVERSITY OF CALIFORNIA SAN DIEGO

SAN DIEGO STATE UNIVERSITY

# Computational and Experimental Investigation of Vortex Cooling of a Gas Turbine Blade Using 3-D Stereo-Particle Image Velocimetry and Liquid Crystals

A dissertation submitted in partial satisfaction of the requirements for the degree Doctor of Philosophy

in

Engineering Science (Mechanical and Aerospace Engineering)

by

Daisy Galeana

Committee in charge:

University of California San Diego
- Professor Prabhakar Rao Bandaru, Co-Chair
- Professor John Scott MacCartney
- Professor Daniel Tartakovsky

San Diego State University
- Professor Asfaw Beyene, Co-Chair
- Professor Samuel Kassegne

2022

Copyright

Daisy Galeana, 2022

All rights reserved.

The Dissertation of Daisy Galeana is approved, and it is acceptable in quality and form for publication on microfilm and electronically.

_____

_____

_____

_____
Co-Chair

_____
Co-Chair

University of California San Diego

San Diego State University

2022

## DEDICATION

To my children Jasmine and Giovanni Trevino for their endless support, unconditional love, and patience. You inspire me to be a better person, mother, and professional. You were by my side from day one, giving me hugs and kisses to keep me going. I love you with all my heart.

To my mother, Rosa E. Martinez, for bringing me to this country that opened the door to unparalleled opportunities. She kept searching for better opportunities for all her children. She taught me that work ethic, perseverance, and sacrifice pay off in the long run. To my siblings, Gema Galeana, Florentino Galeana, and Marco E. Munoz for their support and cheer. To Marcos Munoz, Sergio (Big Checho) Perez and all family members who helped with my kids while I had to study-- thank you.

To my greatest mentor, Dr. Tony Ceja, for teaching me everything: you are a well of knowledge and positive energy. To my dear friend and mentor Theresa M. Garcia for believing in me from day one. I could have never completed all my studies without your unconditional support.

To my friends, Maria del Rosario Ocampo Ramirez, Heather McGregor, Kendric Stephens, Barbara Rutledge, Andy Russell, Andrew Tucker, Claudia Du Carme, Mark Keith, Alma Melendez, Joel Otsuka, Robert Corey Huffman, Miriam, and Larry Figueroa, Elena Cuevas, Thelma Chavez, Natasha Forbes-Celise, Alberto Martinez Gallardo (Comandante), Robyn Thomas, Ruchira S. Sharma, Alicia Miranda, John Thomas Panique, and Araceli Garcia for their unlimited time spent in conversations on why getting a Ph.D. is worth it. To all my friends that took the time to take me out for coffee so I could continue with my studies-- thank you.

## TABLE OF CONTENTS

## LIST OF SYMBOLS

| | |
|---|---|
| $D$ | circular chamber diameter |
| $D_H$ | hydraulic diameter of one swirl chamber inlet |
| $H$ | height |
| $k$ | turbulent kinetic energy, $m^2/s^2$ |
| $L$ | cylindrical chamber length |
| $\dot{m}$ | mass flow, kg/s |
| $P$ | pressure |
| $R$ | radial distance measured from chamber centerline |
| $Re$ | Reynolds number |
| $r$ | radial distance |
| $S_N$ | swirl number |
| $Vz$ | axial velocity |
| $V_\phi$ | circumferential velocity |
| $W$ | air inlet width |
| $r, \phi, z$ | cylindrical coordinates |
| $\rho$ | density |
| $\mu$ | absolute viscosity |

| | |
|---|---|
| $\nu$ | kinematic viscosity |
| $\omega_z$ | circumferential component of vorticity |

## LIST OF FIGURES

## LIST OF TABLES

## ACKNOWLEDGMENTS

I would like to acknowledge my SDSU advisor, Professor Asfaw Beyene, for all the time he spent helping navigate the world of the Ph.D. As chair of my committee, his guidance, advice, and patience have proven to be invaluable. I could not have asked for a better advisor.

I would also like to acknowledge my UCSD advisor, Professor Daniel M. Tartakovsky, for welcoming me to his team. Without him on my committee, this journey would not have been possible.

As well, I would like to acknowledge my UCSD Co-Chair Professor Prabhakar Rao Bandaru for his help and support.

Finally, I acknowledge Solar Turbines Incorporated, for allowing me to use their test facilities and equipment to conduct my research. Without their support, I would not have accomplished so much.

Chapter 2, in part, has been submitted for publication of the material as it may appear in the Proceedings of ECOS 2022 – The 35$^{th}$ International Conference on Efficiency, Cost, Optimization, Simulation and Environmental Impact of Energy Systems, 2022. Beyene, Asfaw PhD, and Mebrat, Ashenafi Abebe, 2022. The dissertation author was the primary investigator and author of this chapter.

# VITA

## EDUCATION

| | |
|---|---|
| 1997-2000 | Associate Engineer, Solar Turbines Incorporated |
| 1998 | Bachelor of Science, San Diego State University |
| 2000-2003 | Certification Engineer, B/E Aerospace, Inc. |
| 2003 | Master of Science, University of Miami |
| 2004-2005 | Project Manager/Test Engineer, L'Garde, Inc. |
| 2005-2006 | Senior Engineer, Goodrich Aerostructure |
| 2006-2014 | Principal Test Engineer-Software, Solar Turbines Incorporated |
| 2014-2018 | Principal Development Test Engineer, Solar Turbines Incorporated |
| 2018-2020 | Regional Technical Manager for Mexico and Latin America, Solar Turbines Incorporated |
| 2020-2022 | Program Manager for Diversity, Equity, and Inclusion, Solar Turbines Incorporated |
| 2022-Pres | Senior Principal Manufacturing Engineer Lead, Solar Turbines Incorporated |
| 2022 | Doctor of Philosophy, University of California San Diego and San Diego State University |

## PUBLICATIONS IN PEER REVIEWED JOURNAL

(1) Galeana, D. and Beyene, A., "Gas Turbines Blade Heat Transfer and Internal Swirl Cooling Flow Experimental Study Using Liquid Crystals and Three-Dimensional Stereo-Particle Imaging Velocimetry," ASME Journal of energy Resources Technology, October 2021, Vol. 143.

(2) Galeana, D. and Beyene, A., "A Swirl Cooling Flow Experimental Investigation on a Circular Chamber Using Three-Dimensional Stereo-Particle Imaging Velocimetry," ASME Journal of energy Resources Technology, April 2020, Vol. 142.

## CONFERENCE PROCEEDINGS

(1) Galeana, D. and Beyene, A., “Computational and Experimental Study of Vortex Cooling Using CFD, 3-D PIV, and Liquid Crystals,” Proceedings of ECOS 2022 – The 35th International Conference on Efficiency, Cost, Optimization, Simulation and Environmental Impact of Energy Systems, July 2-7, 2022, Copenhagen, Denmark.

(2) Galeana, D. and Beyene, A., “Experimental Heat Transfer Study Using Liquid Crystals on a Swirl Flow in a Cylindrical Chamber with and without Elbow,” Proceedings of ECOS 2021 – The 34th International Conference on Efficiency, Cost, Optimization, Simulation and Environmental Impact of Energy Systems, June 27 – July 2, 2021, Taormina, Sicily, Italy.

(3) Galeana, D. and Beyene, A., “Liquid Crystals and 3D Stereo-PIV Used for Heat Transfer and Swirl Cooling Flow Study in a Circular Chamber with and without Elbow,” Proceedings of ECOS 2019 – The 32nd International Conference on Efficiency, Cost, Optimization, Simulation and Environmental Impact of Energy Systems, June 23-28, 2019, Wrocław, Poland.

(4) Galeana, D. and Beyene, A., “Study of Circular Chamber with Elbow Using Swirl Cooling Flow by 3-D Stereo-PIV,” 2019 AIAA Aviation and Aeronautics Forum and Exposition, January 8, 2019, San Diego, California, USA.

(5) Galeana, D. and Beyene, A., “Experimental Approach on a Swirl Flow and Heat Transfer Coefficient Using a 3-D Stereo-PIV and Liquid Crystals,” Proceedings of the 5th International Conference on Heat Transfer and Fluid Flow (HTFF'18), August 16-18, 2018, Madrid, Spain.

(6) Galeana, D. and Beyene, A., “Internal Swirl Cooling Flow Characterization of a Turbine Blade Leading Edge by Means of 3-D Stereo-PIV,” ASME 2018 Turbo Expo, Turbomachinery Techinical Conference & Exposition, Presented by the ASME International Gas Turbines Institute, June 11-15, 2018, Oslo, Norway.

(7) Galeana, D. and Beyene, A., “Experimental Investigation of Heat Transfer and Swirl Cooling Flow in a Circular Chamber Using Liquid Crystals and 3-D Stereo-PIV,” Proceedings of ECOS 2018 – The 31st International Conference on Efficiency, Cost, Optimization, Simulation and Environmental Impact of Energy Systems, June 17-22, 2018, Guimarães, Portugal.

(8) Galeana, D. and Beyene, A., “Experimental Study of Swirl Cooling Flow on a Circular Chamber Using 3-d Stereo-PIV,” Power & Energy Conference & Exhibition, ASME, June 24-28, 2018, Lake Buena Vista, Florida, USA.

(9) Galeana, D. and Beyene, A., “Influence of an Elbow on a Circular Chamber with Swirl Cooling Flow by 3-D Stereo-PIV,” SoCal Fluids XII, April 14, 2018, Los Angeles, California, USA.

## FIELD OF STUDY

Major Field: Mechanical and Aerospace Engineering

Studies in Fluid Mechanics
Heat Transfer
Thermodynamics
Professor Asfaw Beyene, Co-Chair
Professor Prabhakar Rao Bandaru, Co-Chair

ABSTRACT OF THE DISSERTATION

Computational and Experimental Investigation of Vortex Cooling of a Gas Turbine Blade Using 3-D Stereo-Particle Image Velocimetry and Liquid Crystals

by

Daisy Galeana

Doctor of Philosophy in Engineering Sciencce (Mechanical and Aerospace Engineering)

University of California San Diego, 2022

San Diego State University, 2022

Professor Asfaw Beyene, Co-Chair
Professor Prabhakar Rao Bandaru, Co-Chair

One of the limiting factors for the advance of gas turbines has been the turbine inlet temperature. Advancements in efficiency gas turbines engines are often measured by increasing level of turbine inlet temperature and rising optimal compressor pressure ratio. To overcome these limiting factors, a big focus has been on new schemes of internal

cooling designs of turbine blades, using pressurized air from the engine compressor. The challenge related to improving the efficiency come with the need to maximize the efficiency of the internal cooling of the turbine blade to withstand the high turbine inlet temperature. Understanding the fluid mechanics and heat transfer of internal blade cooling is therefore of paramount importance.

This dissertation presents the impact of vortex flow cooling on the heat transfer of a gas turbine blade cooling passage to understand the mechanics of internal blade cooling. The vortex flow is generated through continuous injection of tangential flow. The experimental investigation is presented first with 3-D Stereo-Particle Image Velocimetry (Stereo-PIV) and second Thermochromic Liquid Crystal (TLC). The study provides an evaluation of the developments of vortex cooling methodology utilizing 3-D Stereo-PIV and TLC. The objective of the experimental models is to determine the critical swirl number that has the potential to deliver the maximum axial velocity results with the highest heat transfer at three different Reynolds numbers, 7,000, 14,000, and 21,000. Additionally, a 3-D domain fluent setup employing a steady-state pressure-based solver with a standard k-epsilon turbulence model was applied.

The cyclindrical chamber with seven air inlets with elbow produced the optimum results. As part of the results relatively low heat transfer rates were observed near the upstream end of the cylindrical chamber, resulting from a low momentum vortex flow as well as crossflow effects. The TLC heat transfer results exemplify how the Nusselt Number (Nu) measured favorably at the midstream of the chamber. Experimental results are consistent with the Computational Fluid Dynamics analysis (CFD) results. Introducing air through the inside of the blade utilizing seven air inlets can remove as much heat from

the blade surface, increasing heat transfer, and subsequantly increasing turbine rotor inlet temperature.

# CHAPTER 1 INTRODUCTION

The thermal efficiency of a gas turbine engine increases with the increase of the pressure ratio and firing temperature. In fact, without real gas properties, there is no efficiency increase with temperature, only specific power. One strategy for improving efficiency in gas turbines by increasing the firing temperature above the threshold, i.e., increasing the turbine rotor inlet temperature (TRIT), is mitigating the material failure by internal cooling of the rotor blades. Significant research has been ongoing for decades to design an internal cooling system for the first-stage blades, in particular, to achieve higher firing temperature. Effective internal cooling of rotating blades is a significant challenge, compounded by wake-induced turbulence and unfavorable area ratios between inner and outer surfaces [1] [2]. This can cause formidable challenges to turbine internal cooling, particularly to the blade leading-edge. It is a common practice to cool high-pressure turbine blades using air from the compressor. Coolant air is routed to the turbine blades where it passes through the blade's internal passages lowering the blade's temperature [1].

## 1.1 Foundation

A few years ago, during a conversation with a high-ranking engineer at Solar Turbines Incorporated, the need to do additional research was mentioned with regard to further developing the concept based on vortex flow cooling where air is supplied tangentially to the inner wall of the leading edge flow path through a slot or row of discrete

holes parallel to the channel axis. The vortex flow cooling methodology comprises of cooling air channeling through the blade's internal passages lowering the metal temperature, therefore the experimental cylindrical chamber is made of acrylic allowing detailed measurements and includes seven discrete tangential air inlets designed to create the vortex flow. The objective of this dissertation is to understand the vortex flow cooling behavior, to find the optimum geometry in relation to the critical Swirl Number ($S_N$), and to gain knowledge of the velocity field in the vortex flow cooling chamber. Furthermore, addressing the physical behavior of a more effective internal cooling technique for the blade leading edge, while at the same time taking in consideration the sensitivity of manufacturing tolerances, the cost to manufacture, and durability for long-term operation.

## 1.2 Background and Related Studies

### 1.2.1 Gas Turbines

In today's gas turbine engines, the turbine inlet temperatures may be much higher than the melting temperatures of the blade materials [3]. Therefore, various cooling techniques are applied on the turbine blade to keep the working temperature within a safety limit [4] [5] [6] [7]. In the arena of gas turbines, swirl flow cooling methodology uses coolant air from the compressor routed into the turbine blades where the coolant air passes through the blade's internal passages, and as a result, lowering the temperature [8] [9]. Adding complexity to the demanding task of managing high temperature without its accompanying penalties is the driving desire for a long-term life cycle without frequent inspections and overhauls. Analytical and experimental modeling in the leading-edge area of the blade, with regard to internal swirl cooling systems, could result in optimization

of turbine blade designs with respect to heat transfer, cost, and performance, as well as reduced downtime [10] [11] [12]. A gas turbine has three or more turbine stages, the first-stage is the closest to the combustor exit temperature where the local temperatures are the highest. The first-stage blade must have internal flow cooling; however, the second- and third-stage blades may not have internal cooling passages.

### 1.2.2 Gas Turbine Blade First Stage Internal Cooling Techniques

The life cycle of a blade in the hot section of the gas turbine, herein called turbine blade, is most affected by the high operating temperatures, constant centripetal loading, and thermally induced stresses during start-up and shutdown. The first and second stage rows of blades of the turbine are typically the most critical components, as these turbine blades operate at a gas temperature of around 1,204$^{o}$C, a very high temperature [8] [13] [14]. Additionally, permanent material deformation results from the turbine blades withstanding high temperatures and constant mechanical stresses, which limits the turbine blade life cycle [15] [16]. These factors can cause local plastic yielding while also contributing to material creep [17]. As the gas turbine inlet temperature increases, the heat transferred to the turbine blade also increases. Previous research has proposed several techniques to improve the convective heat transfer for internal cooling of gas turbine airfoils in recent years, including rib turbulators, pin fins, dimpled surfaces, impingement cooling, and swirl flow cooling [7] [18] [19] [20] [21].

In 1998, Glezer et al. [16] presented experimental results comparing three separate studies and led to a better understanding of the screw-shaped swirl cooling technique for heat transfer in internal swirl flow, where heated walls were applied and a

screw-shaped cooling swirl was generated, introducing flow through discrete tangential slots. The first was the heat transfer magnitudes in a rotating cylindrical channel, with discrete rectangular jets located along the channel tangentially to its inner surface. The second was the hot annular cascade heat transfer capabilities in a screw-swirl cooled turbine blade without rotation. Third and last was the mapping of the temperatures from the screw-swirl cooled blade in the actual engine environment with rotation. Glezer et al. [16] mentioned Coriolis forces play an important role in enhancing the internal heat transfer when their direction coincides with a tangential velocity vector of the swirl flow. A key discovery is that the centrifugal and coolant density ratio-driven buoyancy forces do not appear to produce an effect on the overall average heat transfer; instead, they lead to the redistribution of the local heat transfer along the passage. The internal passage geometry has room for improvement with relation to location and size of the tangential slots; as well, the ratio of both had an important impact on achieving the best potential performance of the screw-shaped swirl for the internal blade leading-edge cooling. Glezer et al. [15] reported results of the internal cooling structure of a turbine blade in which the main concept was based on a cooling air supplied tangentially to the leading-edge channel’s inner wall through one slot or row of discrete holes. The model had tangential impingement jets and included an air discharge path through the tip of the channel, replicating the turn into the blade tip passage. Results clearly indicate that formation of a screw-type vortex flow in a channel produces significant heat transfer augmentation and provides great potential for the blade leading-edge cooling. Glezer et al. [16] also created three distinct vortex or screw-cooling configurations and collected a flow visualization and heat transfer measurements using a thermochromic liquid crystal technique. Results

showed that the Nusselt number generally decreases with the distance from the injection slot in all five considered cases yet changes more noticeably in the axial direction. Interestingly, the Nusselt number was found to vary less than 7% circumferentially from its center core. Additionally, the first section of the flow showed gradual increases in both tangential and axial velocities, while the second section of the flow revealed a highly swirl flow, resulting in high heat transfer. Lastly, low-level flow indicates the flow had already begun making a turn toward the tip passage, where no tangential air injection existed [22] - [23]. Although Glezer's studies extends understanding of the physical behavior of flows in swirl chambers, the maximum number of air inlets that offers both heat transfer and fluidmechanics results were not found.

In 2000, Hedlund et al. [24] published that the local surface Nusselt numbers increase when increasing Re number (the range in this study was 6,000 to about 20,000). As a result, local swirl chamber heat transfer and flow structure are connected to increased advection, as well as notable alterations to vortex behavior near the concave surfaces of the swirl chamber. In the study, one model examined the isothermal chamber where the flow results were attained, and the second measured the Nusselt number, using infrared thermography in aggregation with thermocouples, energy balances, and impromptu calibration procedures. One key outcome was that, along with the Nusselt number, the changes of surface heat transfer downstream of each inlet increased sharply when compared to other locations. Hedlund et al. [24] observe that as the turbulent flow becomes more pronounced, the axial and circumferential velocities get larger and intensify the turning of the flow from each inlet. Hedlund employed much lower Re numbers and a different geometry than the one presented here. The surveys of Re

numbers presented in this current study has a low Re of 14,000 and as high as 21,000, which are more inline to the current turbine needs.

Studies show that the blade's internal cooling techniques are effective and considerable regarding long term life, which can address these expectations in tandem with advanced blade alloys [25] [26]. Extreme thermal loads, in conjunction with large inertia and dynamic forces, and compounded by unfavorable area ratio between the outer and inner surface, pose formidable challenges in turbine cooling and endurance. Furthermore, the deviation of the stagnation point during off-design operation complicates the problem even more [16] - [21]. The pairing of external heat transfer rate with wake-induced turbulence also complicates efforts to fully understand the phenomenon. Experiments conducted by Ligrani et al. [4], Moon et al. [1], and Glezer et al. [15] introduced an internal cooling structure as one way to attend to high temperature management in gas turbine cooling. Extensive study by Hedlund et al. [24] focused on exotic geometries that are not manufacturing-friendly, an option that undoubtedly adds to the cost of production. Others, such as Zhang et al. [27], studied jet impingement cooling, proven to be highly effective for turbine nozzles but not for rotating blades. Overall each research added improvement of the turbine blade internal flow cooling, however, none of those studies paid a particular attention to the flow and thermal behavior near the internal concave surface of the cylindrical chamber utilizing all three CFD, 3-D stereo-PIV, and Liquid crystals on the same geometry.

### 1.2.3 Vortex Flow Cooling: Swirl Number, Reynolds Number, and Nusselt Number

The vortex flow cooling technique is described as the continuous injection flow inside a turbine blade leading edge. Hedlund et al. [28] also studied the internal injection design of the vortex chamber and the effect with and without controlled inlet forcing. Their results indicate that controlled inlet forcing is suitable for inducing different vortex pair developments, where secondary flow and mixing are formed by vortices without sizable qualitative changes. In an experiment that included two swirl chambers, Thambu et al. [29] and Chang et al. [30] presented the local flow behavior and heat transfer results. The two swirl chambers modeled passages that cool the leading edges of turbine blades. The swirl flow results from an isothermal swirl chamber show that a higher Reynolds number generates larger axial components of velocity and increases the swirl flow from each inlet. Important findings are that the Nusselt number (Nu) increases when, due to advection, Reynolds number increases, and that the vortex changes characteristics near the concave surfaces of the chamber. Haiyong at al. [31], Han et al. [32], and Hendlund et al. [24] conducted flow imaging studies of swirl flow in a cylinder with a singular tangential injection slot. Reynolds numbers were limited to the 19,000 - 28,500 range. The photographs show the cylinder longitudinal and circular cross sections revealing 3-D flow structures. While insightful, these findings do not calculate the strength of the vortical structures, nor mention the relationship between the size and structure to the rate of swirl decay, or the actual number of tangential slot inlets.

In 2015, Zhang et al. [27] studied experimental flow reversal phenomena associated with confined decaying vortex type flow. The evaluation of the measured static

pressure distribution revealed a region of positive pressure gradient indicating, at certain flow conditions, the existence of flow reversal. The flow reversal was characterized by a reverse flow region between a stagnant or forward moving central core and a forward flow region adjacent to the tube wall. One major key finding was that flow reversal depends on the conditions imposed just upstream of the injection location as well as the vortex intensity. Kumar et al. [33] performed flow visualization studies of swirl flow in a cylinder with a singular tangential injection slot. Photographs were taken of circular and longitudinal cross sections of the cylinder which revealed three-dimensional flow structures. Results were presented with Reynolds numbers ranging from 19,000 to 28,500. A rapidly spreading helical stream was observed to be the primary flow. The helix partly surrounded a secondary flow that had a vortex center migrating with stream wise direction. A major key finding was that axial symmetry does not hold in confined vortex flow with tangential injection. While enlightening, Kumar's findings did not quantify the strength of the aforementioned vertical structures, nor did they relate their size and structure to the rate of vortex decay or a varying number of tangential slot inlets. Yang et al. [34] performed a similar investigation; the difference was that they examined a turbulent flow field in a tube heated uniformly from the wall. A similar tangential injection scheme was used, and the key significant finding was that no difference in the flow field and turbulence intensities was found between the adiabatic and the diabatic experiments. Yang et al. [35] proved that mixing caused by pushing the colder and heavier fluid to the wall, and hotter and lighter fluid to the center as a result of centrifugal force, is not a major mechanism for heat transfer enhancement.

Experimental research conducted by Moon et al. [1], Glezer et al. [16], Zhu et al. [36], and Yang et al. [37] document that when internal vortex flow cooling methodology is used to deliver air flow into the leading-edge tangentially to the inner curved surface, significant heat transfer intensification can be achieved. First initiated by Kreith et al. [22], many continued to expand on these studies. Hedlund et al. [24] [28] [38] [39], completed experimental studies based on a variety of devices and complex geometries to develop a vortex internal flow. As reported by Lin et al. [40], Sheen et al. [41], and Takeishi et al., [42], experimental models employing a screw vortex flow technique were designed, but only using one or two inlets and one exit. These models unveil that the reasonably uniform heat transfer delivery of the screw shape internal cooling structure along the leading-edge curvature makes this concept more advantageous than impingement cooling and as well, at a lower manufacturing cost than that of other structures. Additionally, Moon et al. [1] used a practical range of Reynolds (Re) numbers from 4,418 to 8,286 for a turbine internal flow, yet the Re number is higher for today's gas turbine requirements. The paper presented results of the internal cooling structure of a turbine blade where the main concept was based on a cooling air supplied tangentially to the leading-edge channel's inner wall through one slot or row of discrete holes. The model had tangential impingement jets and included an air discharge path through the tip of the channel to replicate the turn into the blade tip passage. Results clearly show that the formation of a screw-type vortex flow in a channel produces significant heat transfer augmentation and provides promising potential for blade leading-edge cooling. Bakirci et al. [43] also created vortex configurations, collecting flow visualization and heat transfer measurements with a Thermochromic Liquid Crystal (TLC) technique. Camci et al. [44]

[45] [46] studied TLC cases, results showed that the temperature generally does not show a significant effect of rotational speed on the TLC. In one study by Ren et al. [47] the Nusselt number was found to vary less than 7% circumferentially from its center core. Also, the first section of the flow showed gradual increases in both tangential and axial velocities, while the second section of the flow revealed a highly vortex flow, resulting in high heat transfer. Finally, low-level flow indicated that the flow had already began making a turn toward the tip passage, where no tangential air injection existed. A key finding, in which the overall average dimensionless heat transfer coefficients were associated by a power function of the Reynolds number, is that the pressure loss coefficient across the tangential slot was independent of the slot Reynolds number for a given geometry.

Other similar studies concentrated on the lengthwise continuous tangential injection, studying only the local tangential jet velocity, and not the turbulent chamber flow vortex structure [48] [49] [50]. Their research concentrates on the internal cooling blade method, which comprises a vortex cooling design that tangentially delivers air to the inner wall through a row of discrete holes parallel to the channel axis. Findings include temperature variation within the blade material, causing thermal stress; therefore, it must be limited to protect blade life. Generally, a few recent efforts, reported that a significant increase in heat transfer is achievable with leading edge vortex cooling and preferable to impingement with cross flow [51] [52] [53] [54]. Their studies are executed at practical Reynolds number ranges, where flow and heat transfer are almost five times higher than that of heat transfer in a smooth channel. The successful qualitative analysis from Moritz et al. [55] does not provide measurable understanding into the nature of velocity

distributions nor the critical swirl number, and neither do they address any concerns of the primary vortex precession.

The evolution of concentrated vortex and wall jet style vortex flows were described, but only for swirl numbers less than 0.18. Despite the very small range of vortex intensity studied, this investigation provides the first major successful use of LDV for investigating vortex flow phenomena. Yang et al. [60] revealed that leading edge vortex flow cooling can achieve significant heat transfer augmentation. Results illustrate flow and heat transfer studies at practical Reynolds number ranges; heat transfer improvement is more effective than impingement with cross flow and is almost five times higher than heat transfer in a smooth channel. Despite providing a successful qualitative analysis, the authors do not offer quantitative insight into the nature of critical flow structures, velocity distributions, nor address any uncertainties regarding primary vortex precession, even at Reynolds numbers as high as 20,000. Additionally, no computational investigations are performed for comparison to the experimental results.

In 2007, Yang et al. [51] published an experimental study measuring heat transfer enhancement in a circular duct with lengthwise continual injection. Using Thermochromic Liquid Crystal (TLC) techniques, local heat transfer coefficients for different channel diameters to jet slot heights were experimentally measured. Overall average dimensionless heat transfer coefficients were correlated by a power function of the Reynolds number. One key finding was that the pressure loss coefficient across the tangential slot was independent of the slot Reynolds number for a given geometry. Wassermann et al. [61] investigation is one of the few looking at lengthwise continuous injection, but only investigates local tangential jet velocities and not the turbulent tube flow

vortex structure. No computational methods of investigation are presented for comparison. Furthermore, Tieyu et al. [62] presented a study of heat transfer in a channel with a straight portion followed by a portion with mild curvature. Results demonstrated these transitional phenomena showed the effects of curvature, stream-wise development, and flow tripping where the study exhibited Nu numbers from concave and convex surfaces. Finally, it was determined that high thermal performance can be accomplished only by increasing surface areas for convective heat transfer and by enhancing convective heat transfer coefficients, with minimal increases in streamwise pressure drop penalties and skin-friction coefficients. Wang et al. [63] in the succeeding few years, compared multiple heat transfer augmentation techniques, including vortex flow in a tube with multiple inlets.. In these assessments, a composite schematic diagram of flow features near the second inlet of a vortex chamber is presented. Large scale motions from core swirl flow, as well as secondary flows due to Görtler vortex pairs, and shear layers that form on either side emerging from the inlet duct, can be seen.

By reviewing studies related to vortex flow developments, one critical observation is evident: the departure from experimental investigations is a recent trend. Instead, in the case of the vortex decay investigations, there is a significant increase in computational analyses, motivated by fast, cost effective, and simple means of qualifying data. A meticulous approach is taken when building a reliable computational model and ensuring their results are compatible with realistic (i.e., experimental) data.

Most of the state-of-the-art turbine blade internal cooling technologies have limitations in which turbine cooling effects cannot be easily visualized and evaluated. The study of the internal flow phenomenon in a three-dimensional (3-D) format is a formidable

challenge [64] [65] [23] [66]. Accurate predictions of a gas turbine blade's internal cooling flow path components and heat transfer, especially the first stage blades are essential, particularly as TRIT increases [67] [68]. The gain in efficiency as a result of increasing pressure ratio is compromised by the cooling flow deducted from the compressor air, which is otherwise routed for combustion. As a result, the engine efficiency begins to drop above a particular temperature for a pre-established cooling system. An optimum cooling path exists that improves the blade's internal cooling while protecting the material and increasing the thermal efficiency without excessive bleeding of air from the compressor, which includes film and transpiration cooling with an increase in the specific power of a gas turbine [69] [70].

Vortex cooling flow is essential to future blade design and the optimization of gas turbines. Before such methods are utilized, an enhanced understanding of three-dimensional (3-D) flow field behavior must be obtained. In the years of research summarized here, it is clear that the development of more effective internal cooling techniques is required, paying particular attention to the internal cooling for the blade leading edge. Utilizing advanced technology such as 3-D Stereo-PIV to highlight the true behavior of the air particles, combined with liquid crystal measurements, this research advances this field of studies toward the next generation of internal cooling techniques [71] [72] [73] [74]. Local flow fields, swirl number, and Nusselt number at each air inlet are all emphasized; therefore, this study differs from others as it provides a more accurate flow field, helping to predict areas where heat transfer can be maximized -- something that was not possible 20 years ago. The most optimal results have been achieved when

the internal vortex flow cooling is allowed to transport radially, creating a three-dimensional vortex flow in the cylindrical chamber.

Hedlund, et al. [24] investigated the Reynolds numbers based on inlet duct characteristics; an important finding was that the variation of surface Nu numbers and time averaged flow characteristics were present due to arrays of Görtler vortex pairs, especially near each of the two inlets, where Nu numbers are highest. The Nusselt Number, Nu, is defined as the ratio of convective to conductive heat transfer, as shown in Eq. (*1-1*).

$$Nu = \frac{hD}{k} \tag{1-1}$$

Lee et al. [79] investigation of a screw-shaped vortex cooling technique using a lengthwise continuous tangential injection model. The diameter to jet slot height ratio was proven to be the most important geometric parameter. This team managed to collect flow visualization at Reynolds numbers from 900 to 19,000, capturing mean velocity components, static pressure, and total pressure as well as the presence of Görtler vortices near the walls. Noot, et al. [80] continued the numerical analysis this time with and without controlled inlet forcing. Results suggested that controlled inlet forcing can be used to induce different vortex pair development, and secondary flow and mixing was formed by the vortices without significant qualitative changes. The same year, Hedlund, et al. [24] presented experimental results from a local flow behavior and heat transfer experiment: two vortex chambers that model passages were used to cool the leading edges of turbine blades; flow results were obtained in an isothermal vortex chamber. Higher Re also produced larger axial components of velocity and increased turning of the

flow from each inlet. As well, the Nu number increased with increasing Re, due to increased advection and equally important changes to vortex characteristics near the concave surfaces of the vortex chambers. The expected advantages of comparing various techniques for enhancing convective heat transfer rates in gas turbine engine passages used for internal cooling of turbine airfoils is a better heat transfer augmentation to maintain safe and long operation [81] [82]. Several discoveries were observed: one showed that the lowest thermal performance parameters were measured in flows through passages with pin fins and some types of rib turbulators; and the second, that relatively high thermal performance parameters produced by vortex cooling chambers are a result of friction factor ratios as high as 25 and mixing that occurs over a broad range of length scales.

Turbine blade internal flow cooling techniques based on film protection of the leading edge, ribs, pin-fins, and other more exotic geometries provide adequate cooling effectiveness, yet all previous research show how a number of negative effects rised from them, for example increased of local stress concentration, additional aerodynamic penalties, and concerns about engine durability associated with potential of plugging of the small film holes, specially for long-term operation in an industrila enviroment. Can a more effective internal cooling techniques be explored utilizing the latest technologies? Would a specific number of air inlets be applied with a closer range of Re numbers on a non-traditional blade cooling?. The first part of the research, the CFD analysis is to be compared to the experimental results. Followed by the study of vortex flow cooling in a cylindrical chamber that simulates the internal flow path of a turbine blade, incorporates three-dimensional (3-D) Stereo-Particle Image Velocimetry (Stereo-PIV) focused on the

flow field. Third, the research segment involves a second cylindrical chamber painted with liquid crystal to evaluate the heat transfer. Cylindrical chambers are designed and tested to correlate the effects of the velocity distribution on the Nusselt Number.

## 1.3 Contributions

This thesis investigates the internal vortex flow cooling design for a gas turbine blade. Studying a novel internal cooling design using CFD, 3-D stereo-PIV, and liquid crystals for a gas turbine blade first stage is analyzed. The results from the simulation are compared to experimental data, which is collected and analyzed herein.

- Development of a novel CFD analysis, utilizing a meshing in both solid and fluid domains, and incorporating generic turbulence modeling in the fluid as well as finite strain in the solid.
- Design and construction of a larger scaled gas turbine blade internal cooling passage for experimental purposes, including velocity field mapping and calibration of data acquisition equipment.
- Experimental collection of performance data for two test articles, geometrically identical, one cleared and one painted with liquid crystals, in a wide range of flow conditions with associated performance comparison.
- Validation of the reverse flow in simulations of the performance of both vortex flow cooling with and without the elbow.
- Application of validated 3-D stereo-PIV and liquid crystals, indicating possible advantages of the internal cooling design.

- The possibility of flow separation was simulated, predicted, and validated using this experiment, Galeana, et al. [83]. Experimental input data were provided for the analyses which showed that higher pressure input can contribute to lowering the temperature at the exit from the chamber, favoring the cooling process.

The high temperatures that are now available in the turbine section are due to improvements of blade cooling techniques like the one presented here and the metallurgy of the baldes in the turbine. The outcome of this research will be a first study of the vortex flow as cooling in a 3-D methodology and compared to the liquid crystals results in search of the most advantageous Nu number, and could have significant implications on future design, particularly in heat transfer scenarios.

### 1.3.1 Thesis Outline

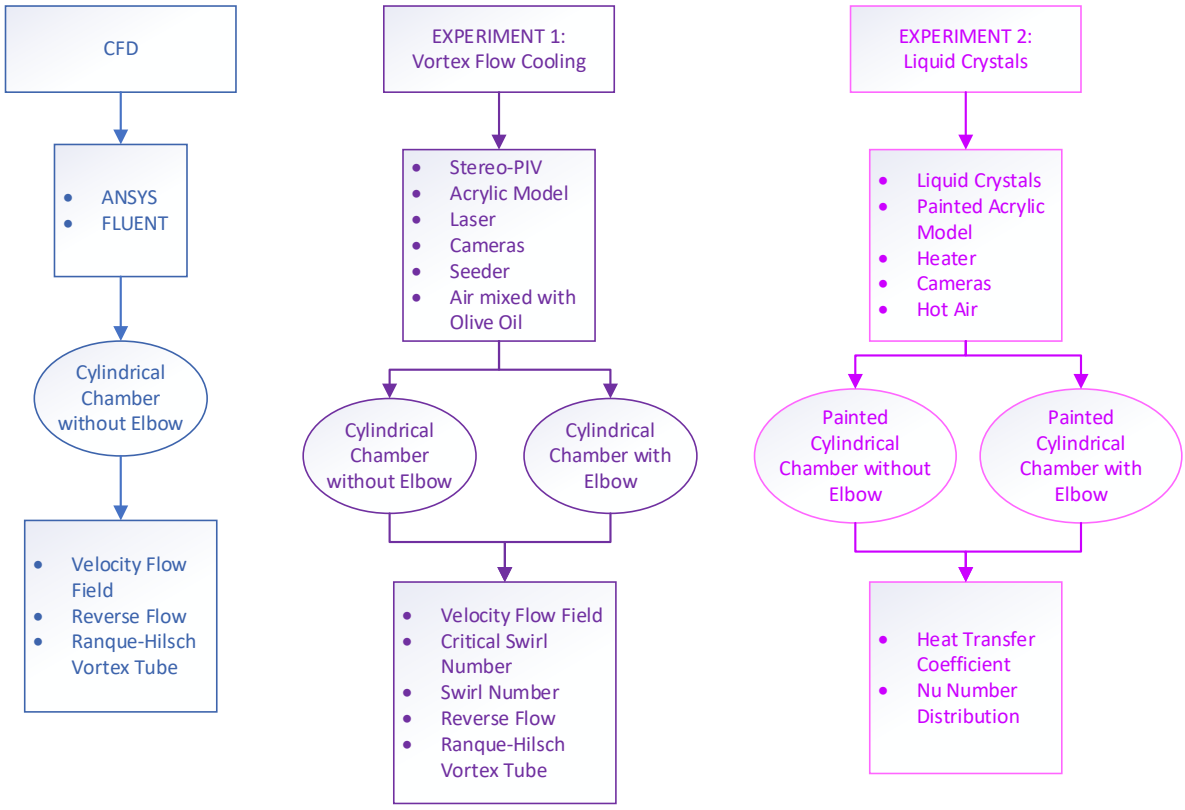


Figure 1-1: Thesis Outline for CFD, Vortex Flow Cooling, and Liquid Crystals.

### 1.3.2 Computational Fluid Dynamics (CFD) Analysis

The assembling was done in ANSYS and CFD analysis was carried out with three parameters, namely Re number, pressure, and temperature. CFD allows observation of the vortex flow properties at locations that may not be accessible to measuring instruments. CFD analysis was conducted using 3-D domain and turbulent flow approximations. The internal vortex flow cooling of the blade was simulated on three aspects, flow pressure, temperature changes, and velocity. The results of the CFD simulations were then compared with the experimental data. There is a slight difference

when comparing results considering that ideal conditions could not be maintained experimentally.

The experimental work gives the most advantageous swirl number and Nu number. The same can be done using CFD analyses but takes more time and resources to compute.

### 1.3.3 Experiment Plan

A crucial factor for gas turbine performance, and one of the most challenging engineering intricacies regarding improving energy efficiency, is maximizing the internal cooling of the turbine blade to withstand the high turbine inlet temperature. Consequently, the need to increase power density and performance has driven TRIT higher and higher, requiring a full understanding of wide-ranging design and analysis, including fluid mechanics and heat transfer to meet the constraints of higher temperatures (i.e., exceeding 1093$^{o}$C). Inspiring this research are the challenges inherent in developing a turbine blade with a simple passable internal cooling flow system that can withstand the high temperatures on the leading edge.

The experiment plan is the vortex flow cooling in a cylindrical chamber produced through dynamic and passive methods, namely through chambers and tangential inlets and guided radial and axial vortex. The objective of the first experiment, as described in Figure 1-2, is to assess the actual capacity of the vortex flow cooling using the 3-D stereo-PIV and determine the best vortex flow operating parameters. The investigation focuses on the continuous vortex flow maintained through nonstop tangential air injection. An experimental setup has been designed to obtain 3-D stereo-PIV detailed measurements

of the vortex flow. The second part of the investigation concentrates on liquid crystal heat transfer experimentation to measure the effect of the velocity distribution and evaluate *Nu*. The final part of the investigation is the vortex flow study using CFD analysis, where the results from CFD simulations are analyzed and compared against the experimental results.

The aim of this research is to gain an understanding of the flow structure and the velocity field in the leading-edge of the vortex flow cooling chamber. Stereo-PIV techniques rely on the illumination, recording, reconstruction and cross-correlation of tracer particle distributions in multiple measurement planes. Initial testing has shown that the flow field is characterized by a circumferential flow around the tube axis. Enhanced understanding of the flow field will help to predict regions of increased heat transfer in the vortex chamber. With a stronger grasp of flow behavior and the resulting effect on heat transfer, a new parametrization can be used to calculate optimal geometries that will give higher gas turbine efficiencies and lengthier turbine blade life cycles.

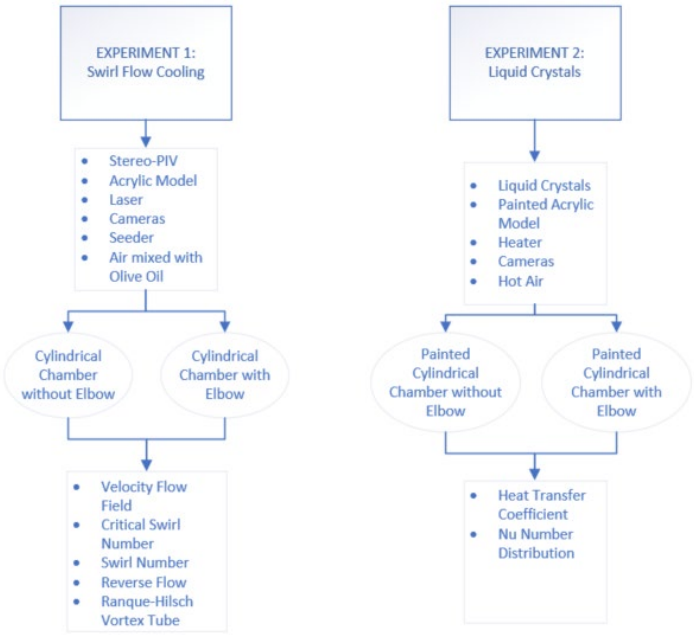


Figure 1-2: Experiment organization plan.

#### 1.3.3.1 Vortex Flow Cooling

The first part of the investigation is the experimental study and was accomplished by developing a cylindrical chamber with and without an elbow that simulates the leading edge of the turbine blade internal cooling design. Commonly used in many types of systems requiring temperature control, vortex flow cooling as an effective method of heat transfer enhancement has a vast range of industrial applications. The focus is on the gas turbine first stage blade leading edge, as shown in Figure 1-3.

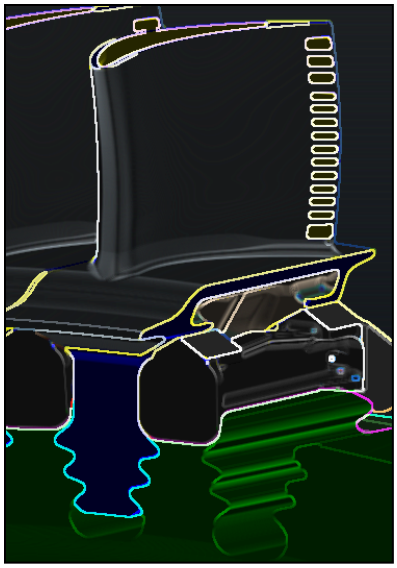

Figure 1-3: Gas turbine blade first stage.

The objective of this first part of the dissertation is to understand the vortex flow behavior, to find the optimum geometry in relation to the critical Swirl Number ($S_N$), and to gain knowledge of the velocity field in the vortex flow cooling chamber. The geometry of the cylindrical chamber, with multiple air inlets at fixed locations to induce vortex flow, is unique and different from any large geometries used in other existing investigations [15]- [20]. Furthermore, the utilization of PIV has proven to be a very effective tool for flow velocity measurements, even in the most demanding conditions, including the gas turbine engine environment [84]. Additionally, researchers agree, as mentioned in Moon, et.al. [1], that extending this technique to the third dimension is challenging while obtaining the same level of accuracy for the out-of-plane velocity. Furthermore, utilizing PIV in the third dimension while obtaining the same level of accuracy for the out-of-plane velocity is a large challenge [14]. The test Reynolds numbers are based on air inlet height, of the blade internal cooling design, ranging from 7,000 to 21,000. The first part of the experiment used stereo-PIV at nominal Reynolds number, ± 50%, and ran the experiment with and

without the elbow to compare velocity flow fields. The experimental results of the first part of the investigation revealed the $S_N$ distribution at different axial positions z/D for all three Reynolds numbers obtained from the measured velocity field. The experiment was run with the same test setup several times to find the critical $S_N$; the $S_N$ for all conditions decreases within the chamber length due to wall friction and dissipation. The central hypothesis is that the optimal design is a cylindrical chamber with elbow and seven air inlets, a hypothesis formulated based on our own preliminary data produced using stereo-PIV in a chamber with 14 air inlets. Once a favorable design was found, optimum conditions for the experiments were defined, first using the vortex flow cooling, and secondly, using liquid crystals for Nu distribution.

The experimental setup in this research is designed to improve the vortex flow cooling mechanism by allowing detailed measurements, using 3-D stereo-PIV, of the flow field characteristics, the internal cooling area highlighted in Figure 1-4. The main focus is the flow behavior of the seven, discrete, tangential air inlets at three Reynolds numbers: 7,000, 14,000, and 21,000. 3-D stereo-PIV is a very effective tool for calculating flow velocity vectors, even in challenging conditions such as the gas turbine environment.

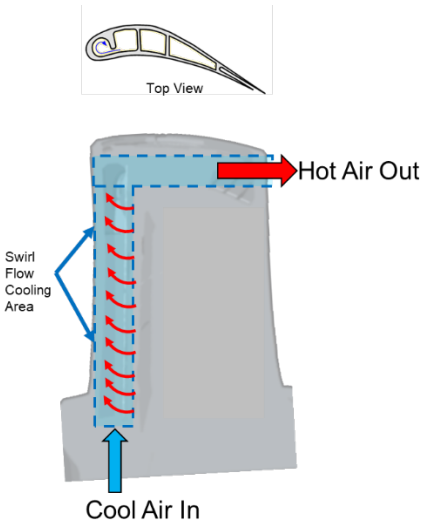


Figure 1-4: Turbine blade leading edge internal cooling design.

The focus of this study is vortex flow cooling methodology, specifically how cooling air is directed to the turbine blades as it circulates through the blade's internal passages to decrease leading-edge temperature, in Figure 1-4. The impact of decreasing the blade temperature is a highly effective technique required for long term endurance to satisfy the bulk metal temperatures. The pressure-driven flow on the vortex cooling flow is evident with the change of direction of the flow rotation. Figure 1-5 illustrates passages where continuous injection occurs and creates a vortex flow in the turbine blade leading edge. The experimental setup was built to concentrate on the flow field characteristics, which are easy to capture via an acrylic walled model, allowing better measurement of the flow field. The vortex chamber configuration came from maximizing diameter-to-air inlets width ratio, as it is the most critical geometric factor per Glezer's experimental design. Seven, discrete, tangential air inlets permit the air to come across at three different Re numbers. In the case of heat transfer design, two common types of vortex flow exist: continuous and decaying. In this study, continuous vortex flow is used for both the vortex flow cooling

and heat transfer, which is maintained by means of continuous injection of tangential flow. Although each air inlet generates intense vortex flow, it deteriorates with downstream distance.

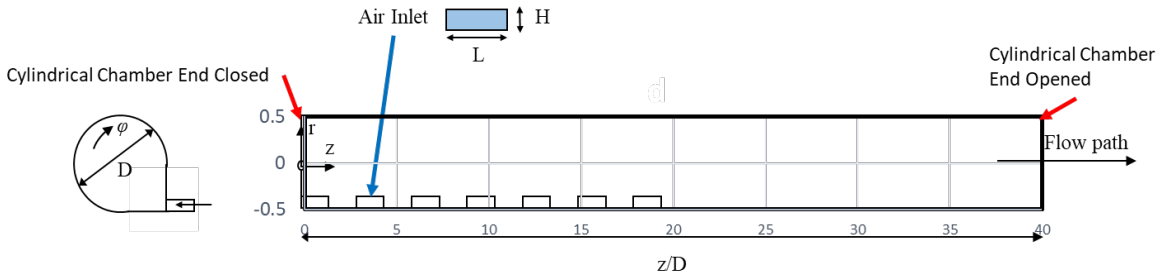


Figure 1-5: Cylindrical chamber geometry with seven air inlets.

The experimental results presented here are from the internal vortex flow cooling utilizing 3-D Stereo-PIV, performed with the practical range of Re numbers simulating the internal flow of a turbine blade. A few advantages of using Stereo-PIV over other flow measurement methods include capturing the velocity flow field and more precise direction information of multiple particles. All fluid particles are captured on the same plane, nearly instantaneously and non-intrusively; with other methods, this is nearly impossible.

Previous research has shown many techniques to improve the convective heat transfer for internal cooling of turbine airfoils in recent years, including rib turbulators, pin fins, dimpled surfaces, impingement cooling, and swirl chambers [56] - [69]. The current state-of-the-art in turbine blade cooling technology lacks a means for turbine cooling effects to be visualized and evaluated. Although the stated techniques are effective, we are seeking better results, requiring the vortex flow to be better understood.

### 1.3.4 Thermochromic Liquid Crystal (TLC) and Heat Transfer

The heat transfer results are presented from a surface Nusselt number distribution on a second acrylic cylindrical chamber coated with Thermochromic Liquid Crystal (TLC) that produces a green hue for a controlled narrow temperature range. TLC comprises materials that change their reflected color as a function of temperature when illuminated by white light and materialize as visible light in different wavelengths. Images are acquired using a video camera and software for image analysis, and videos of tests record the color change over time. The video file data are combined with temperature probe data to produce heat transfer coefficient results. Then, in-house software calculates the heat transfer coefficients from green time data, thermocouple temperatures, and model material properties by using a semi-infinite thermal solution.

# CHAPTER 2 COMPUTATIONAL FLUID DYNAMICS (CFD)

## 2.1. CFD Study of the Cylindrical Chamber to Simulate Vortex Flow Cooling

CFD applications have been used to predict the loadings and flow distributions of blade rows, including end wall regions for over four decades. As a tool it is recognized that CFD can achieve major solutions, yet still has limitations in predicting turbine heat transfer, in large part because of the limitation of modeling turbulence and vortices, uncertainty of boundary conditions, and the inherent flow unsteadiness in turbomachinery. The geometrical model for the vortex flow cooling system was developed using SOLIDWORKS 2020. The simulation domain was 3D, with seven rectangular inlets with a dimension of 44.45 x 22.68 mm each, and two outlets with a diameter of 40 and 80 mm. A coaxial connection, shown in Figure 1-3, was preferred for a one-side closed chamber with a single outlet having a diameter of 40 mm. The elbow was not included in this study case. Usually, connecting with the elbow or making a coaxial connection has little or no impact on the results. The advantage of not using an elbow is matching the experiment boundary conditions to compare velocity field flow.

The large-diameter pipe is the cylindrical chamber where the computational model simulates the flow separation of the incoming pressurized air into hot and cold streams, as it was revealed in the experiment [85] [86]. Since the working fluid, air, was assumed to be an ideal gas, ideal gas equations determine all the properties and parameters. The input parameters, pressure, and temperature were obtained from experimental data,

Table 2-1. All inlet temperature remains at 302K determined at Re = 14,000. The cold exit pressure was left as that of the ambient, i.e., 0 Pa, for both cases. It is assumed that the system operates in ambient and at sea level conditions.

Table 2-1: Input boundary conditions.

| Location | Pressure (Pa) |
|---|---|
| Inlet_1 | 399.9 |
| Inlet_2 | 382.6 |
| Inlet_3 | 353.7 |
| Inlet_4 | 707.4 |
| Inlet_5 | 708.78 |
| Inlet_6 | 710.15 |
| Inlet_7 | 1295.5 |
| Hot outlet | 714.98 |

A 3-D domain fluent setup employing a steady-state pressure-based solver with a standard k-epsilon turbulence model was applied [87]. The energy equations were activated to handle the temperature effect with the gravitational acceleration accounted for. The coupled pressure velocity scheme was chosen for equation discretization. Other than the turbulence kinetic energy special discretization, all the variables were set as a second order-upwind scheme. The flow Courant number was set at 50 for convergency purposes. However, the under-relaxation factors were left as the default values.

## 2.2. CFD Study of the Cylindrical Chamber without Elbow to Simulate Vortex Flow Cooling

### 2.2.1. Domain and Discretization

The geometrical model is shown in Figure 2-1 (a) and (b). The right end of the chamber is closed with the assumption that the hot stream will turn to the right.

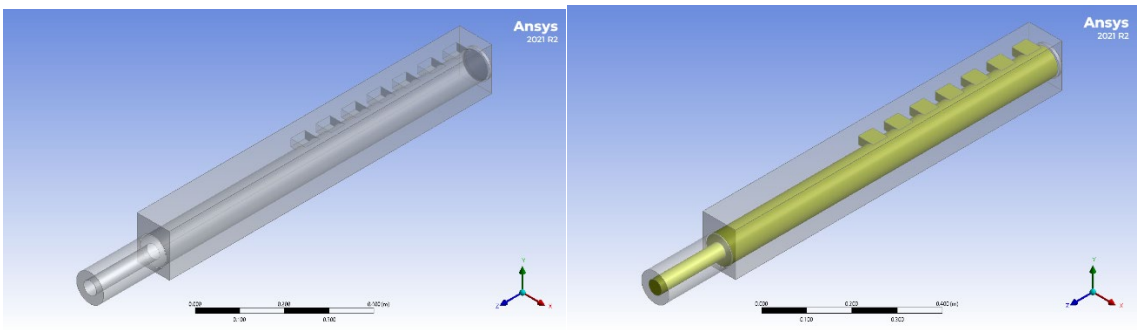


(a) (b)

Figure 2-1: (a) Vortex cooling system and (b) Fluid domain of compressed air.

The physical domain was discretized by using the ANSYS 2021 R2 version with an element size of 5 mm. The boundaries of the model are presented in Figure 2-2. The cell zones are the fluid domain and the cylindrical camber. In addition, the main boundaries to be used as inlets and outlets include the single outlet shown by the red arrows, and the seven inlets shown by blue arrows.

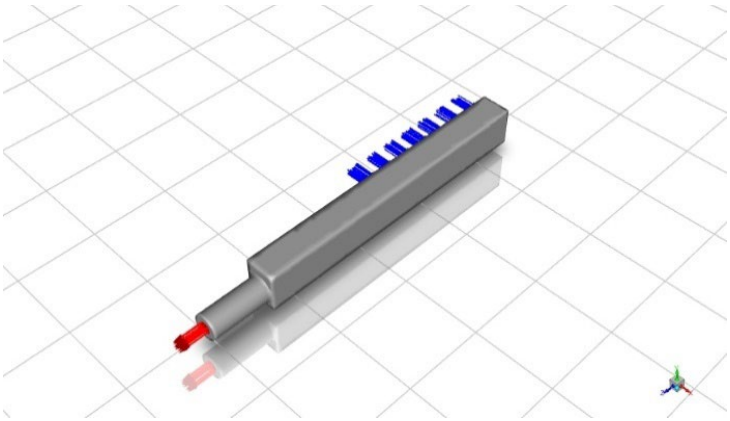

Figure 2-2. The flow direction of the model.

### 2.2.2. Simulation Results and Discussion

#### 2.2.2.1. Velocity

Results presented in Figure 2-3(a)-(c), are the velocity streamlines at the first, second, and third inlets. All those inlets have the same result with the previous condition; i.e., the reversed flow.

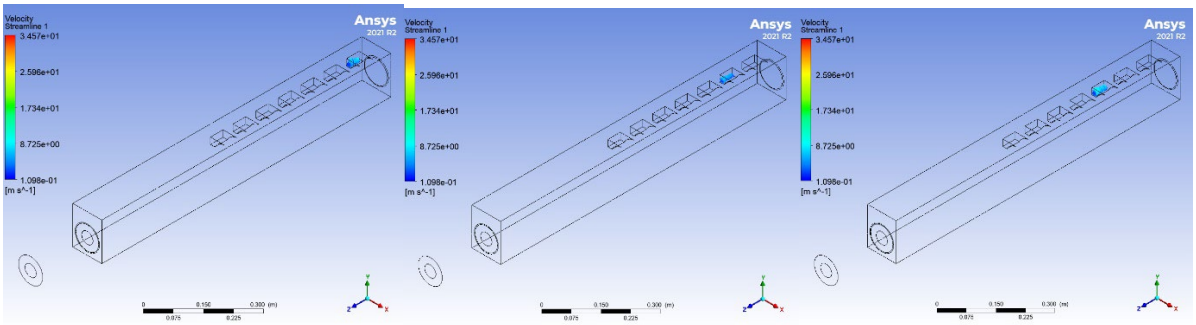


(a) (b) (c)

Figure 2-3. Velocity streamline at inlets 1 (a), 2 (b) and 3 (c).

The velocity streamlines for the whole fluid domain are presented in Figure *2-8*. The largest velocity value is noticed at inlet 7 at 30.457 m/s. There are three reversed

flow cases at the inlets 1, 2 and 3. The velocity is minimum near to the closed end of the chamber.

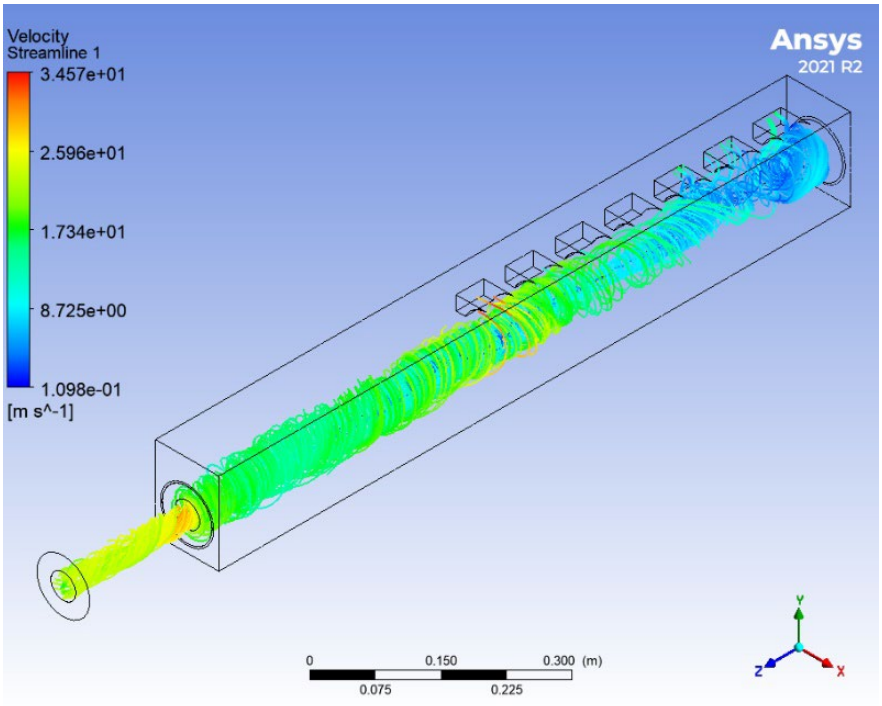


Figure 2-4. Velocity streamline of the fluid domain.

#### 2.2.2.2. Pressure

The pressure distribution along the cylindrical chamber is given in Figure 2-5. The highest pressure is observed in front of inlet seven reading 979 Pa. However, after air inlet seven the cross-section of the chamber, the pressure distribution shows significant drop resulting in -30.870 Pa.

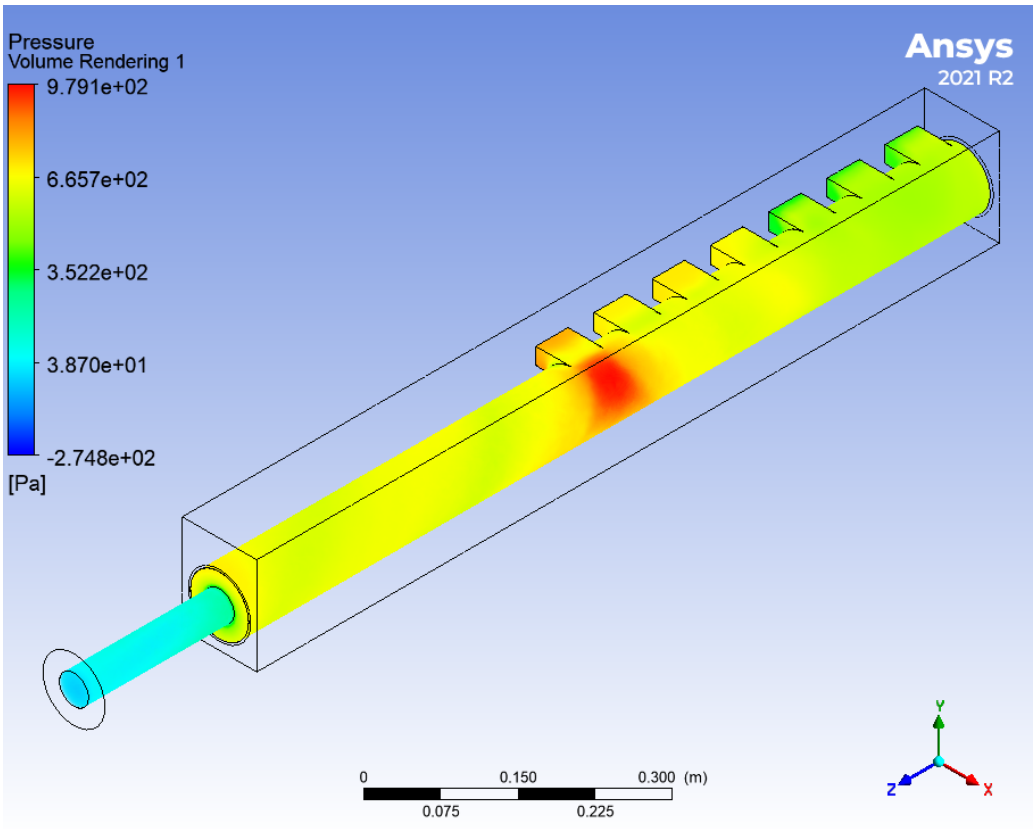


Figure 2-5. Pressure contour of the vortex chamber and tube.

#### 2.2.2.2 Temperature

The lowest temperature of 301.4°C was calculated at inlet 7 and air inlets one thru six, as shown in red in Figure 2-6, were calculated as the hottest regions. The temperature rises and drops at the closed end and tube outlet is 0.033 and 0.351 °C, respectively. The longest part of the vortex chamber adjacent to the tube helps the fluid to obtain a longer residence time. Therefore, the fluid accelerated in the tube executing a number of rotations. The temperature contour in Figure 2-6 indicates separate cold temperatures to the left and hot to the right fluid regions.

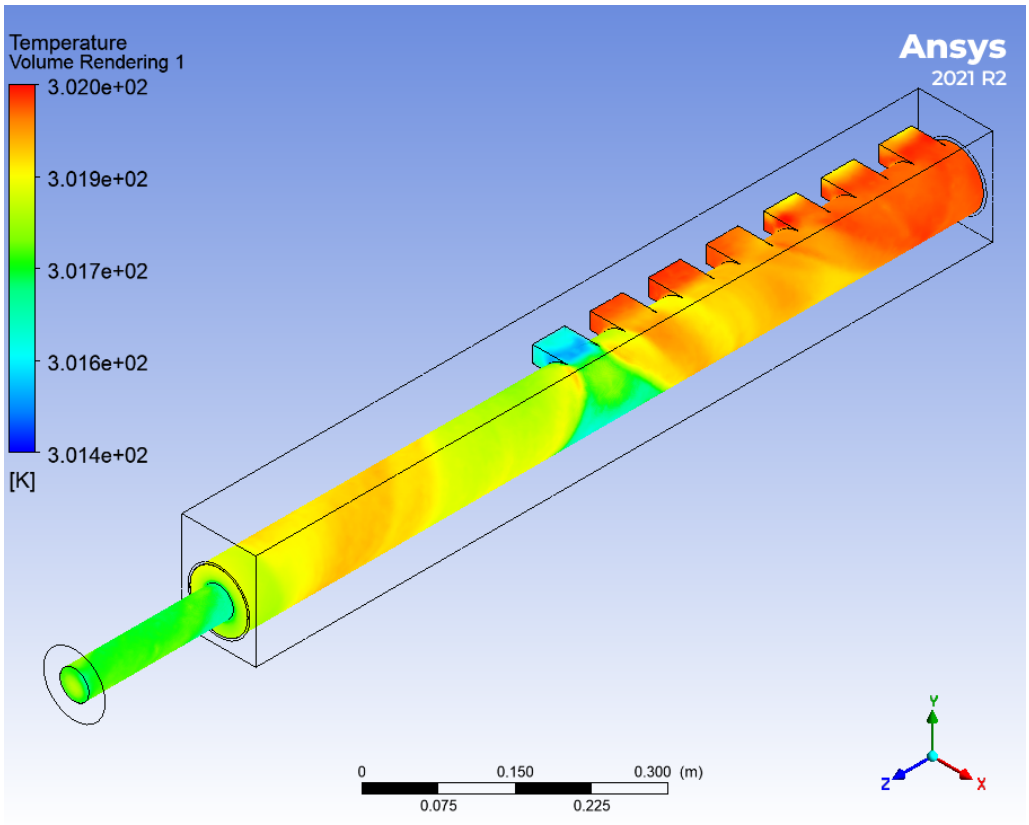


Figure 2-6. Temperature distribution contour of right-end-closed vortex chamber and tube.

#### 2.2.2.3 Mass Flow Rate

The conservation of mass was satisfied. Inlets 1, 2 and 3 have a negative value of mass flow, showing the reversed flow situation as seen in Figure 2-4. Overall, the total mass inflow rate for the closed scenario is 0.0535 kg/s. Velocity, viscosity, density, and Re number are given in Table 9.

Table 2-2. Summary of mass flow rate at the inlets and outlets.

| Location | Inlet 1 | Inlet 2 | Inlet 3 | Inlet 4 | Inlet 5 | Inlet 6 | Inlet 7 | Hot outlet |
|---|---|---|---|---|---|---|---|---|
| Flow Rate, kg/s | 0.0481 | 0.0471 | 0.0528 | 0.0606 | 0.0730 | 0.0860 | 0.1087 | -0.4761 |

Table 2-3. Value of outlet variables and Reynold's number.

| Location | Velocity [m/s] | Viscosity [kg/m.s] | Density [kg/m$^{3]}$ | Re |
|---|---|---|---|---|
| Outlet | 22.3767 | 0.0000713 | 1.16995 | 14687 |

### 2.3. Summary and Discussion

The purpose of this simulation was to evaluate the feasibility of a gas turbine blade vortex flow cooling. In this simulation, a cylindrical chamber scenario with one-side open and one closed was evaluated for the possibility of flow separation to cold and hot air. The vortex cooling system contains seven inlets and one outlet. The air that enters the cylindrical chamber through the seven air inlets has different pressure values where the maximum and minimum values are at the last and first air inlet, respectively. Nevertheless, the inlet temperature for all inlets remained constant at about 302K.

The vortex cooling effect was significant at air inlet seven with the highest velocity flow field. After air inlet seven downstream of the chamber, it is observed that due to change of diameter, the rotating air spent a longer time inside the chamber before

accelerating. The hottest region is near the closed end. A unique feature of this cylindrical chamber design is the airstream separated coming from inlets 5, 6 and 7. The amount of cold air leaked into the chamber via inlets 1, 2, and 3 was 0.0248431 kg/s. There was a visible velocity flow field region separated by temperature difference to the left and to the right. The drop of temperature was 0.351 $^{o}$C at this location and the temperature rise near the closed end region was 0.033 $^{o}$C.

One recommendation for future work, in order to yield a separated flow, is that the design should be modified to increase the inlet pressure; for example, creating a diffuser, or the incoming air must be diffused in the plenum to compress the air prior to the airinlets. However, the best alternative is increasing the incoming air pressure much higher than the current working pressure without changing the geometry.

Figure 2-7 describes how the compressed air particle rotated in the chamber and suddenly accelerated as it reached the orifice. The sudden acceleration of air will drop the temperature and pressure at the downstream side of the chamber since the working fluid is assumed as an ideal gas.

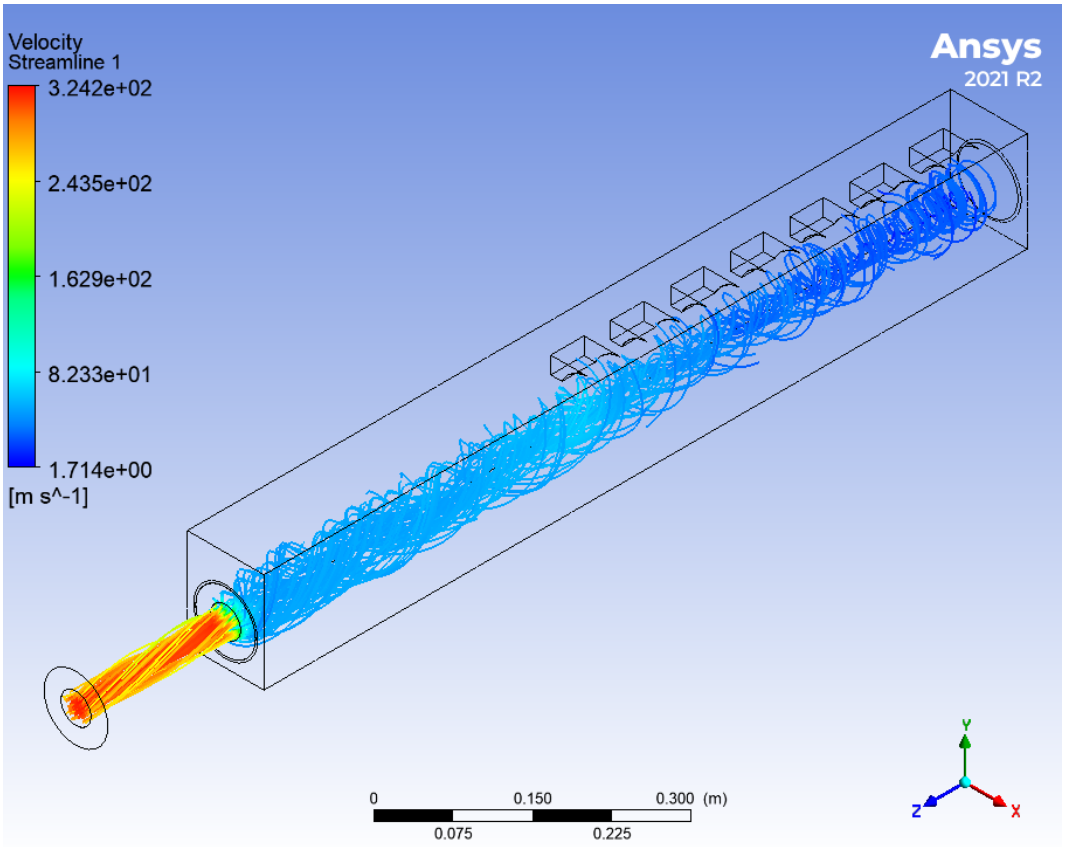


Figure 2-7. Velocity streamline of the fluid domain.

Velocity, viscosity, density, Re number and other variables were evaluated at the outlets. The Re number recommended is 97,937 stile laminar flow regime. The values are given under Table 13.

Table 2-4. Value of outlet variables and Reynold's number

| Location | Velocity [m/s] | Viscosity [kg/m.s] | Density [kg/m$^{3]}$ | Re |
|---|---|---|---|---|
| Outlet | 285.111 | 0.000158 | 1.35407 | 97737 |

Figure 2-8 and Figure 2-9 compare the axial temperature and pressure distribution for the right-end-closed vortex chamber for experiment to a modified scenario discussed

above. The axial temperature and pressure distribution of experimentally obtained pressure looks like a horizontal straight line. The change is invisible for the existing working condition of the vortex cooling chamber. However, if the incoming air is compressed too much, the drop in temperature and pressure is notable. Near the closed-end the temperature and pressure is more or less a horizontal line.

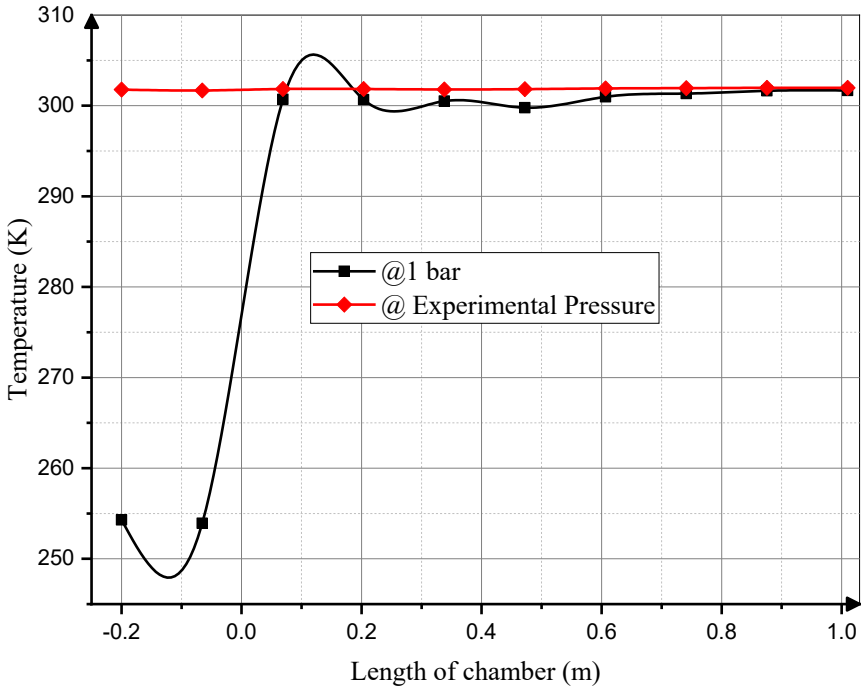


Figure 2-8. Comparison of axial temperature distribution for test results with simulation result at 100 kPa (1bar) pressure inlet (right-end-closed).

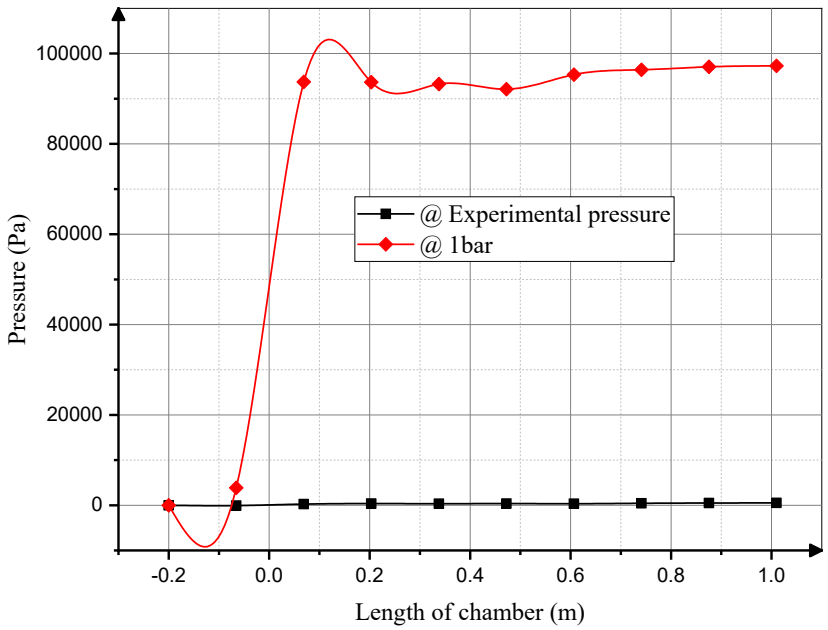


Figure 2-9. Comparison of axial pressure distribution for right-end-closed chamber (experimental versus simulation); the simulation is for 100 kPa (1bar).

While the compressed air is rotating more and more the pressure distribution shows a peak above 100 kPa, shortly after coming down to 90 kPa, and downstream staying around 98 kPa. The moving wave obtained its peak just near the orifice for both temperature and pressure, Figure 2-8 - Figure 2-9. The air accelerates suddenly when it reaches the constriction with peak value of temperature, as the pressure decreases. The temperature and pressure increase slightly at the end of the chamber.

The CFD study resulted in an impressive agreement with the experimental results. One important observation is the reverse flow separation was simulated, predicted, and validated on both CFD and experimentally. Experimental results comprised critical input into CFD for careful analyses, showing that higher pressure input can contribute to lowering the temperature at the exit from the chamber, favoring the cooling process.

## 2.4. Acknowledgement

Chapter 2, in part, has been submitted for publication of the material as it may appear in the Proceedings of ECOS 2022 – The 35th International Conference on Efficiency, Cost, Optimization, Simulation and Environmental Impact of Energy Systems, 2022. Beyene, Asfaw PhD, and Mebrat, Ashenafi Abebe, 2022. The dissertation author was the primary investigator and author of this chapter.

# CHAPTER 3 EXPERIMENTAL PROCEDURES

## 3.1. Vortex Flow Cooling Experimental Setup

While two-dimensional modelling of multiphase phenomena has been dominant to date, current systems, such as LaVision PIV, allow for a better understanding of models with more complex, three-dimensional systems. In the case of internal vortex flow cooling, turbine blade multi-flow models have gained early success and acceptance; therefore, utilizing and expanding the use of such models is encouraging. Thirty years ago, 3-D flow measurements research was effectively impossible to measure, and now, collecting more accurate data is quite feasible, using the latest technologies such as 3-D Stereo-PIV. A combination of 3-D Stereo-PIV technology and cylindrical chamber-instrumented test articles are required to provide the data necessary to verify that all the challenging velocity flow field requirements are satisfied.

The vortex flow visualization is conducted by DaVis, a product of LaVision. DaVis is a comprehensive software for intelligent (laser) imaging applications for non-reactive and reactive flow fields, material surface imaging and tracking and (ultra) high-speed imaging. The 3-D Stereo-PIV technique is used to measure the flow field, providing valuable flow visualization, given that full-field velocity measurements can be obtained without disturbing the flow. Tracer particles must accurately follow the fluid flow to be able to obtain accurate, full-field, velocity profiles. The Stereo-PIV system consists of several

subsystems including a high-power laser, which is used as the illumination source, an optical set-up including a number of lenses to turn the laser light into a laser sheet, and two, high-speed cameras to capture images of the illuminated plane.

The post-processed data is completed in DaVis, velocity calculations are conducted in MATLAB, and TechPlot is used for data visualization. MATLAB (Matrix Laboratory) is a multi-paradigm, numerical computing environment and programming language. MATLAB is used to call functions and subroutines written in as a .dat file, allowing MATLAB to clean up DaVis raw data. Then, it calculates crucial flow field variables for every .dat file. Finally, it creates a file containing newly formatted data that can later be used by another software like Tecplot 360. This step allows all raw data to be converted and visualized in Tecplot 360. Tecplot 360 is a Computational Fluid Dynamic (CFD) and numerical simulation software package used in post-processing simulating results. The combination of the two software programs offers powerful flow visualization options.

### 3.1.1. Acrylic Cylindrical Chamber Geometry without Elbow

An experimental test article is made of a clear acrylic cylindrical chamber to allow visualization of vortex flow phenomena, with seven discrete tangential air inlets, designed to allow detailed measurements of the swirl flow field. The cylindrical chamber, with its chosen coordinates and location of vortex flow measurements, is shown in Figure *3-1*. The test article is instrumented with standard thermocouples and pressure transducers where measurements are collected at chosen coordinates; see Figure *3-1*. To allow a clear inside visualization of the flow phenomena, clear acrylic material is utilized for the

entire test article. The vortex flow is measured at 33 different cross-sectional locations along the length of the chamber, including the midplane of the air inlets, as shown in Figure *3-1*.

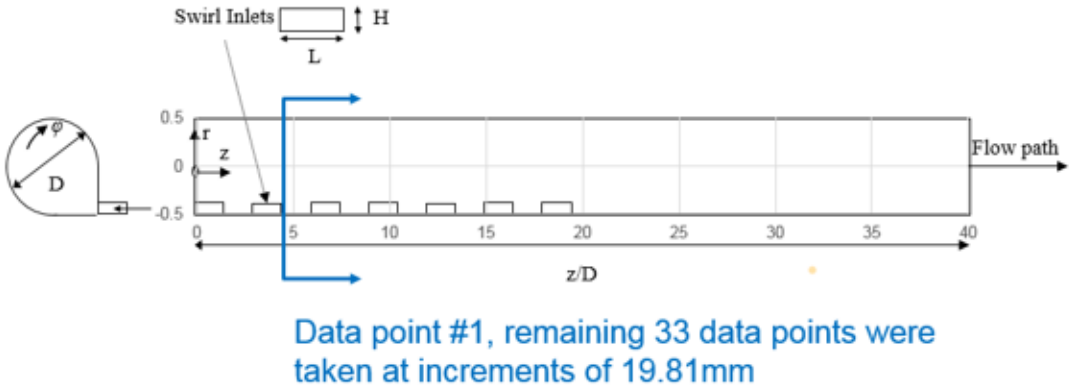


Figure 3-1: Data point number one location.

The test article includes seven air inlets that are in fixed locations, to induce vortex flow cooling. One end of the chamber is closed, and the other end is open to the atmosphere, as shown in Figure *3-2*. The chamber length is 1.07 m where inner and outer diameters are 0.075 m and 0.088 m, respectively. The air is mixed with olive oil particles provided by oil particle seeder (LAVision); both start with a constant temperature.

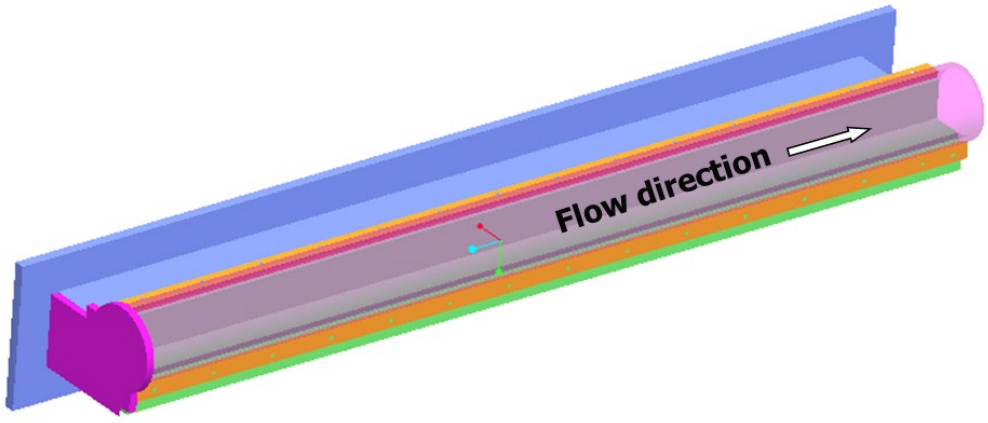

Figure 3-2: Test article: clear acrylic cylindrical chamber.

The Reynolds number is based on the hydraulic diameter of the air inlet, which in this case is 0.011 m. The test article is designed with seven, fixed air inlets to ensure the cooling air mass flow is the same at each inlet. Once the air is mixed with olive oil droplets, it is circulated and forced into the rectangular planum. As the mixed air exits the plenum, see Figure *3-2*, it passes into seven rectangular cross-sectional air inlets ducts. All seven air inlets are tangentially connected to the chamber's inner circumference and are supported with five-hole pressure probes. This assembly allows the vortex flow to have principal axial and circumferential components of velocity; the cumulative flow outline through the cylinder is comparable to a helix [4] [6] [7] [11]. To collect pressure and temperature measurements, in-house developed instrumentation is used. The acrylic cylindrical chamber contains seven thermocouples on its inner surface immediate to the air flow, located 0.134 m just below this surface to provide the measurements of local surface temperature. Transparent acrylic was chosen maximizing axial and circumferential flow visibility along the test surface, which included minimizing the "olive oil smearing" of spatial variation along the test surface as shown in Figure *3-2*. Acrylic also works well for infrared imaging as its surface emissivity ranges from 0.60 to 0.65 [10]. Two high-resolution cameras and processes by DaVis software are used to take the particle images. The vortex flow is measured at 33 different cross-sectional locations, including the midplane of the air inlets, and only measurements conducted with inlet pressure of 172.37 kPa are processed.

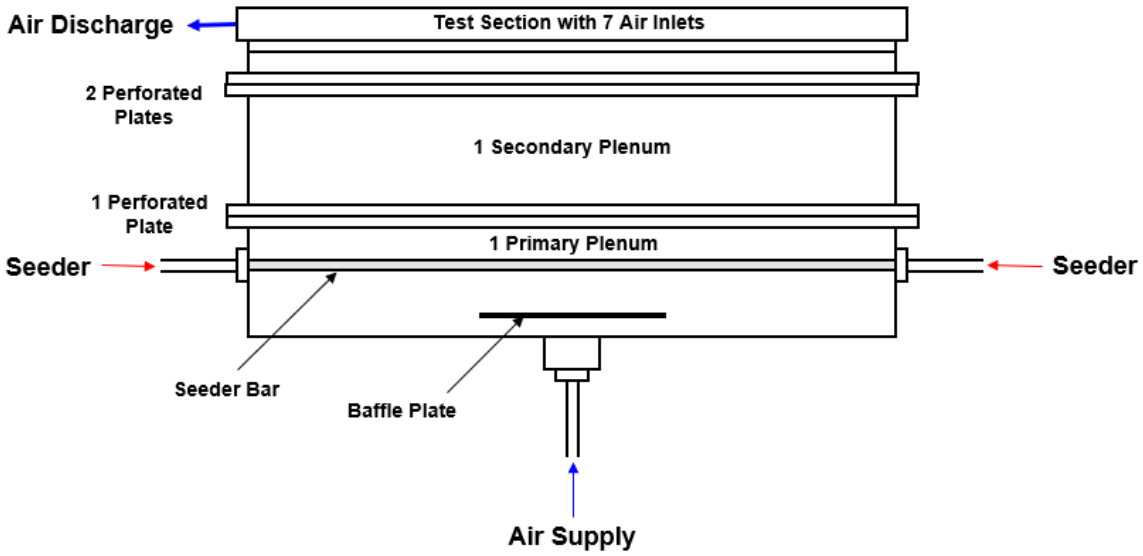


Figure 3-3: Plenum assembly.

### 3.1.2. Acrylic Cylindrical Chamber Geometry with Elbow

The test setup is the same as the one used in the experiment without an elbow, this time with addition of an elbow. The elbow is made of PVC, three-dimensional, printed and cylindrical, and is designed to allow the flow to behave in the same direction as in the turbine blade internal cooling pathway. A detailed cylindrical chamber instrumented with standard thermocouples and pressure transducers is used for air and vortex flow measurements at chosen coordinates. Both the outlet and inlet locations are shown in schematic drawing in Figure 1-4, where one end of the chamber is closed, and the other end is open to the atmosphere. The test fluid consists of air mixed with olive oil at a constant temperature, and provided by a facility-compressed air source, drawing at ambient pressure and temperature. It then forces air through the plenum, as shown in Figure *3-3*. The oil particles for velocity measurements are sourced from a seeding particle generator (LaVision), same as in the experiment without the elbow.

The elbow is designed to be attached to the cylindrical chamber with a 90$^{o}$ curvature, to simulate the turbine blade. The elbow has a 6.35 mm thickness and a 76.2 mm inner diameter, as shown in *Figure 3-4*. The cylindrical chamber to elbow is a quarter circle transition flow path length designed to be as short as possible, because elbow length already includes the scaled distance from cylindrical chamber exit to inner wall of transition elbow. The elbow geometry begins cylindrical and transitions into a rectangular exit flow path area designed to closely match that of the turbine blade trailing edge.

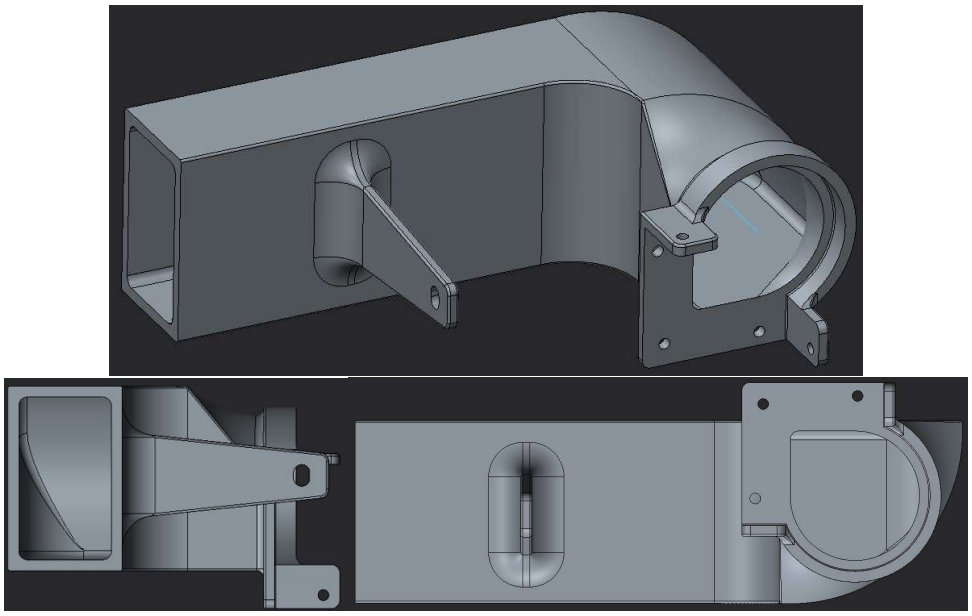

Figure 3-4: 3-D printed elbow design.

Particle images are taken using two high-resolution cameras and processed by DaVis software as shown in Figure *3-7*. The vortex flow in the cylindrical chamber is measured at 33 different cross-sectional locations along the length of the chamber, including the midplane of the air inlets.

### 3.1.3. Three-Dimensional Stereo-Particle Imaging Velocimetry

The three-dimensional stereo-particle imaging velocimetry (3-D stereo-PIV) is a technique that provides instantaneous velocity vector measurements in the cross-section of the cylindrical chamber test article. While two-dimensional modelling of multiphase phenomena has been prevailing to date, current systems such as LaVision PIV, allow for a better understanding of models with more complex, three-dimensional systems. That it is not intrusive, allows the application of PIV in high speed vortex flows, and boundary layer studies of fluids gives this technique its strength. Utilizing and expanding the use of such models is promising in the case of internal vortex flow cooling, as turbine blade multi-flow models have gained early success and acceptance. Thirty years later it is now possible what was once impossible: to collect more accurate data using the latest technologies such as 3-D Stereo-PIV. In combination with 3-D Stereo-PIV, state-of-the-art, cylindrical, vortex chamber-instrumented test articles are required to provide the verification data necessary to satisfy all the challenging requirements. An oil particle seeder (LAVision) is used to provide the particles for velocity measurements while the clear acrylic cylindrical chamber allows visualization of the flow phenomena.

### 3.1.4. 3-D Stereo-PIV Calibration

The Stereo-PIV calibration is a tedious process and time-consuming; one must pay attention to avoid creating a misalignment, which will lead to velocity errors in the peak. The calibration process is among the software, target plate, and both cameras. A 3-D target plate was designed and installed at the middle of the cylindrical chamber's length, as shown in Figure 3-5. In the software the 3D calibration plate was selected called

106-10, also under calibration plate parameters selected using the front and back side of the plate. Followed by pointing both cameras to view the same cross-sectional area. To correctly align the calibration target plate in the exact same plane as the laser sheet is not an easy task. Subsequently, the LaVision algorithm was utilized for easier calibration (self-calibration), which consists of rotating and translating the same plane view for higher accuracy. Next, the recorded targeted plate is used to calculate the misalignment between calibration plate and laser sheet. The last step is to correct the mapping function accordingly, and then the recorded images are evaluated, as shown in Figure 3-6.

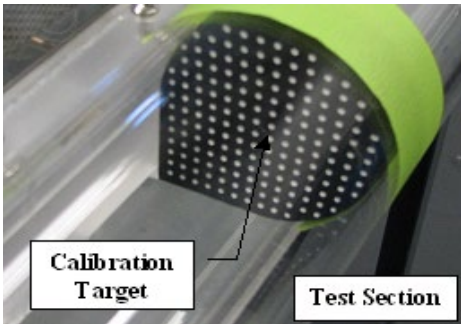


Figure 3-5: Calibration target plate

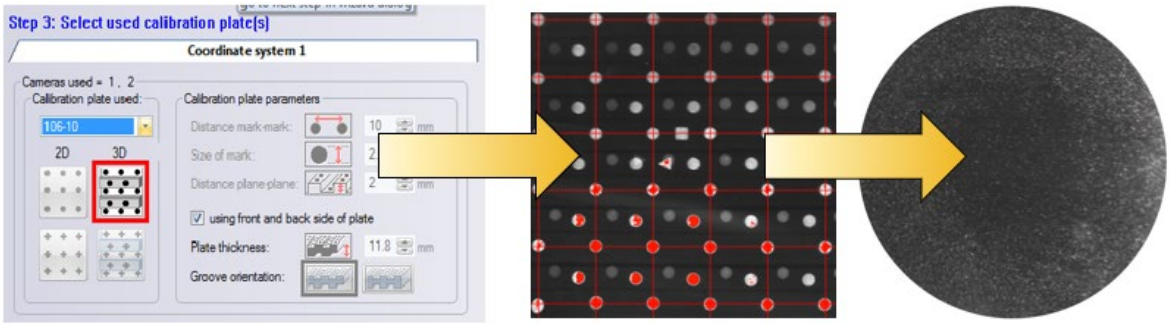


Figure 3-6: Calibration mapping against the recorded images.

To eliminate all calibration errors, because the particle images themselves are used for the final calibration, a traverse system with a step motor was installed to carry

the laser and the two cameras. The setup allowed to take 33 data points along the length of the test article with only one round of calibration.

### 3.1.5. Hardware

The main piece of the laboratory setup for the vortex flow cooling experiment is LaVision Stereo-PIV system, which includes a LaVision PC, two ImagerproX cameras, two Nd-YAG lasers, and LaVision particle seeder as shown in Figure 3-7 and Figure 3-8. The cameras are mounted on a stand equipped with stepper motors, allowing it to travel freely along the chamber length. The fluid is seeded with olive oil particles that have diameters in the range of 1-3 μm and specific gravity of 0.703, see Figure 3-8. These oil tracer particles are chosen because they are small enough that they have little inertia; validating the tracer particle motion best reflects the actual flow path. The seeding particles in the fluid distribute the laser light, which is captured by the video acquisition system. The Nd-YAG laser from New Wave Research is a Pegasus PIV with a wavelength of 527 nm and maximum energy of 20 mJ per pulse. The Nd-YAG laser serves as the illumination source for the PIV system and is manipulated through the appropriate use of optical instruments to produce a laser sheet of 2 mm thickness on the chamber's bottom wall. This setup allows the illumination of planes parallel to the vertical axis. Two high-speed and high-resolution CCD cameras (Vision Research, Phantom v7.3. 800_600 pixels, 12 bit) capture images of the illuminated PIV particles at a rate of 100 frames per second. With that frame rate, 2000 images are acquired over a period of 10 seconds, similar to the measurement duration in the experiment done by other researchers [12-13].

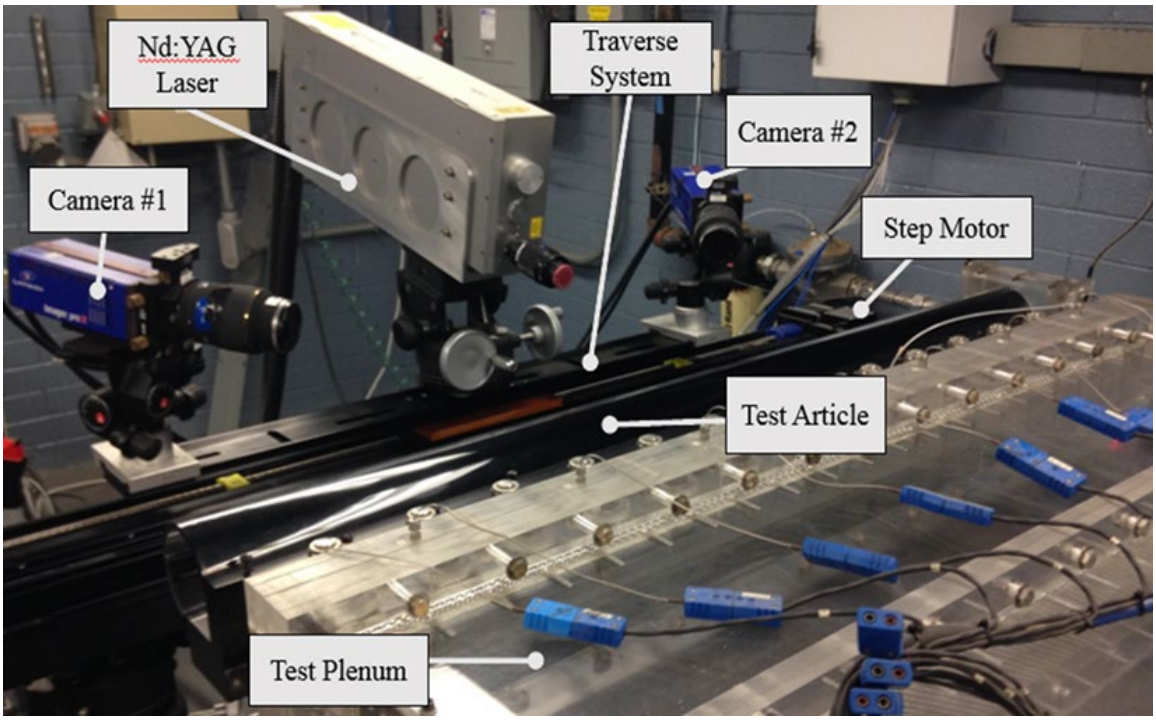


Figure 3-7: Hardware setup.

Figure 3-8: LaVision Olive oil seeder.

### 3.1.6. Software: DaVis, MATLAB, and Tecplot 360

DaVis is utilized to collect PIV data, all data points are taken and collected in one data file. Data file exports time-average velocity and is post-processed in DaVis to be transferred into MATLAB. MATLAB cleans up DaVis raw data and allows the calculation of crucial flow field variables. All velocity calculations are conducted in MATLAB, followed by a file structure that prepares data for visualization in Tecplot 360, which is used for data visualization. One advantage of using Tecplot 360 is that it provides powerful flow

visualization options. Created some macros to automate visualization procedures. To create smooth transitions in between data points, a data interpolation scheme was employed.

### 3.2. Thermochromic Liquid Crystal (TLC) Experimental Setup

In experiment number two, the heat transfer results are measured in a second cylindrical chamber and collected continuously after the system is heat-soaked to the required temperature. An acrylic cylindrical chamber, made with the exact same dimensions as the test article used in experiment number 1, is coated with TLC paint that produces a green hue for a controlled narrow temperature range. The heating mesh located between the plenum and the vortex chamber uses a high current and low voltage wire mesh. The mesh heater is installed in the airflow passage at the inlet to the test section with cables connected from the power supply to the copper connection bars. After the full test article setup is connected, mass flow ($\dot{m}$) is established, the current is switched on to heat up the heating mesh, and the air leaving the heater rises at once to the required temperature. All the while, cameras are recording the color change. Estimated temperatures of the green times are represented in seconds as an intensity image as each pixel turns green. Some images contain noise; therefore, the resulting mappings must be post-processed by removing unnecessary information from the images once both green times have been extracted and TLC data reduction is reached. The program combines three home-grown programs in one application, which assists with tasks such as finding the start time and probe location. These are handled graphically, instead of fathoming index locations on an image. Input consists of a video recording of green time changes, a temperature probe file, and input parameters. Videos of tests record the color

change over time, and the data collected from these video files are combined with temperature probe data to produce heat transfer coefficient results. The focus is on the part of the video when the image regions change to a green color (also called green times) at a given time.

### 3.2.1. TLC Painted Acrylic Cylindrical Chamber Geometry

The test article for the heat transfer is the same as that of the cylindrical chamber for vortex flow measurements; the chosen coordinate system is shown in Figure 1-4. The same seven inlets are in the fixed locations. Inlet and outlet are shown in the schematic drawing in Figure 1-4. The chamber's left-hand side is closed, and the right-hand side is open to the atmosphere. The cylindrical chamber is made of clear acrylic and painted with TLC to allow visualization of color change phenomena during the required time range. As the air enters the plenum, as shown in Figure 3-9, it passes into a rectangular heating mesh, leading to rectangular cross-sectional air inlets with individual hydraulic diameters ($D_H$) of 0.011 m. These inlets are connected to the principal vortex chamber so that one surface is tangent to the chamber inner circumference.

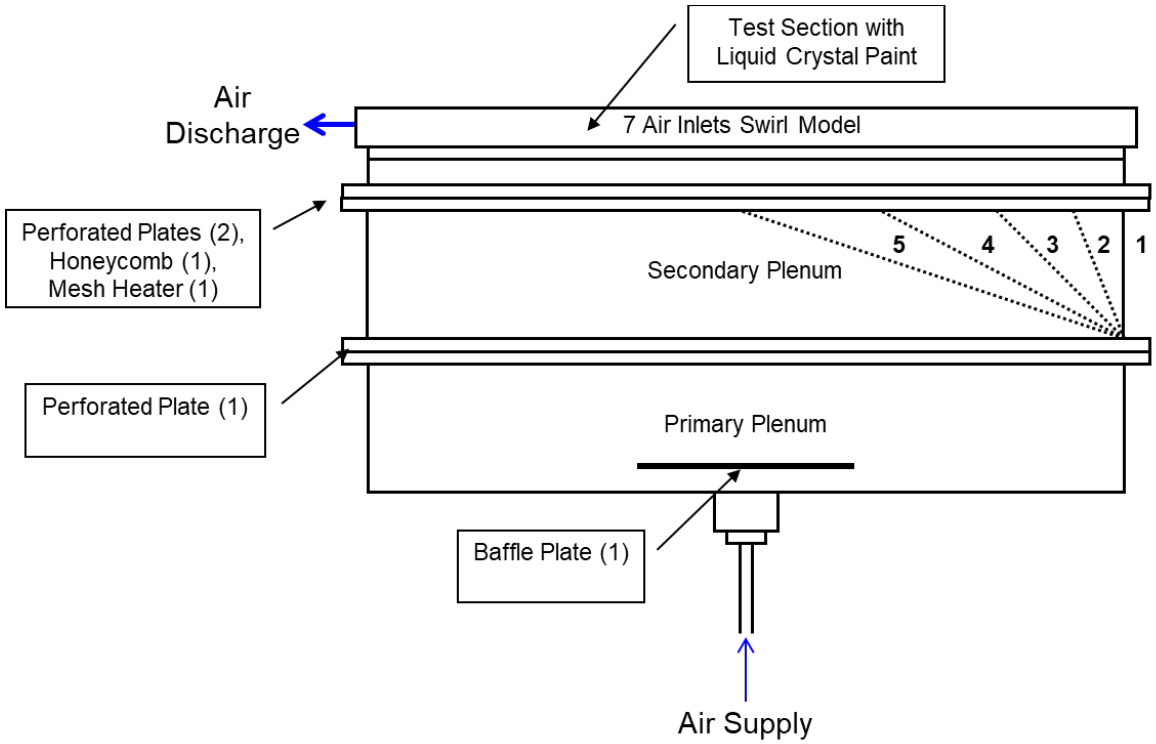


Figure 3-9: TLC painted test article with plenums attached.

### 3.2.2. TLC Painting Process

The TLC helps focus on the most desirable surface area by painting the cylindrical chamber with black and liquid crystal paints that facilitate measurement accuracy to 1 micron. The acrylic cylindrical chamber is painted with SPB100 black primer paint and then with eight layers of R35C1W TLC (liquid crystal paint) from Liquid Crystal resources. Seen in *Figure 3-10*, the surface area optics suitable for the spatial resolution are painted, first the cylindrical chamber is coated with liquid crystal paint, followed by black paint. A coupon is built, following the same process, for calibration purposes, is coated with liquid crystal paint, and followed by black paint.

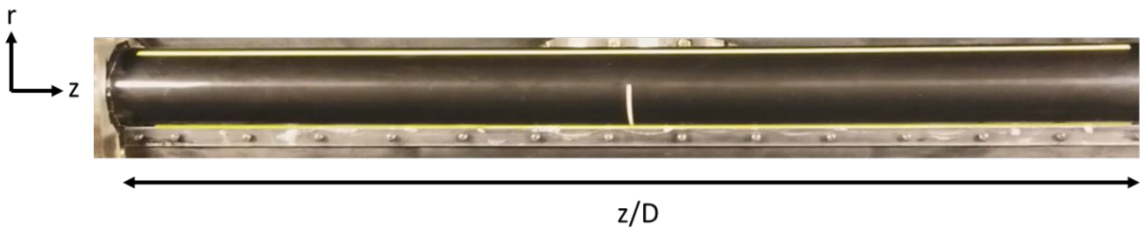


Figure 3-10: TLC painted test article.

### 3.2.3. TLC Calibration Process

Calibrating the liquid crystal paint allows accurate post-process analysis of the liquid crystal paint on the test article for thermal testing. A copper coupon plate is created with an embedded T-type thermocouple bonded on a Peltier-thermoelectric module (Peltier Bridge) heater (Tellurex C2-50-1514). The instrumented copper plates are attached to the thermoelectric module with 3M thermally conductive epoxy adhesive (TC-2810). The coupons are painted with SPB100 black primer paint and then with eight layers of R35C1W liquid crystal paint from Liquid Crystal resources. Black felt is used to block any background images so the video camera view can capture only the coupon. Setting an LED light indicates when the switch is in test mode and at the same time breaks the thermocouple circuit to correlate the data and video time stamp. An EX1048 temperature scanner is used to collect the data, and the thermocouples are connected to it, followed by connections to the thermoelectric module to the power supply with a multimeter in parallel with the power supply to detect voltage. Supplying two volts to the thermoelectric module, while simultaneously flipping the test switch on the thermo flow bench, correlates the time between the EX1048 data and video. Once the coupon is visually inspected and has fully transitioned in color, the power supply is stopped and powered off. These steps

are repeated at least three times. The estimated temperatures for the entire input domain of the green time image are generated from probe data and then mapped.

### 3.2.4. TLC Data Collection

An in-house software to synchronize the entire liquid crystal experiment. The data is collected by continuously polling after the system is heat-soaked to the required temperature. The data acquisition step size is 0.5 seconds and the VXI is set to a time interval of 0.2 seconds. The video file is converted to an AVI file, imported into the "Liquid Crystal Imagine Analyzer (LCIA)," as shown in Figure 3-12, a Solar Turbines Incorporated program, and set to an intensity threshold of 0.7. Contact resistance and temperature drop through the wall are determined experimentally from the calibration process and green time is measured simultaneously. Using seven calibrated thermocouples equally separated across the length of the cylindrical chamber, the temperature of the air entering the cylindrical chamber is measured. All measurements are collected when the cylindrical chamber is at steady state and when the heating mesh on the plenum reaches 35°C.

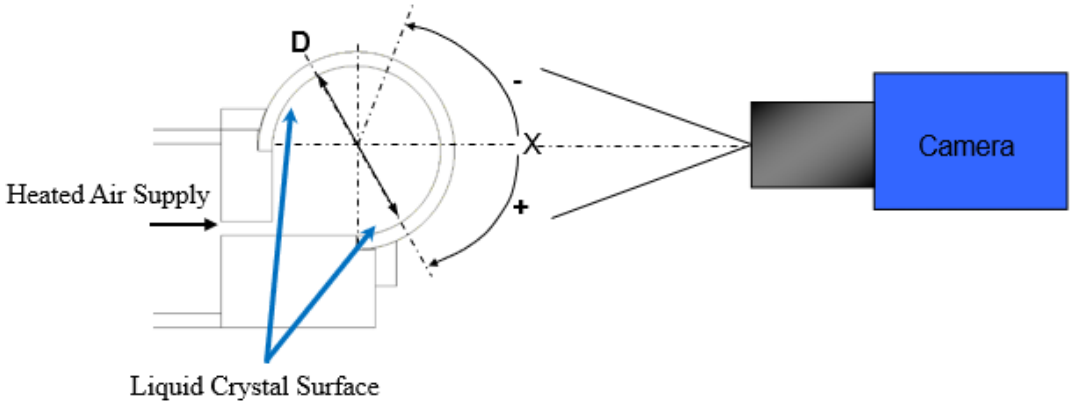


Figure 3-11: Camera location to collect the color changes of the liquid crystals.

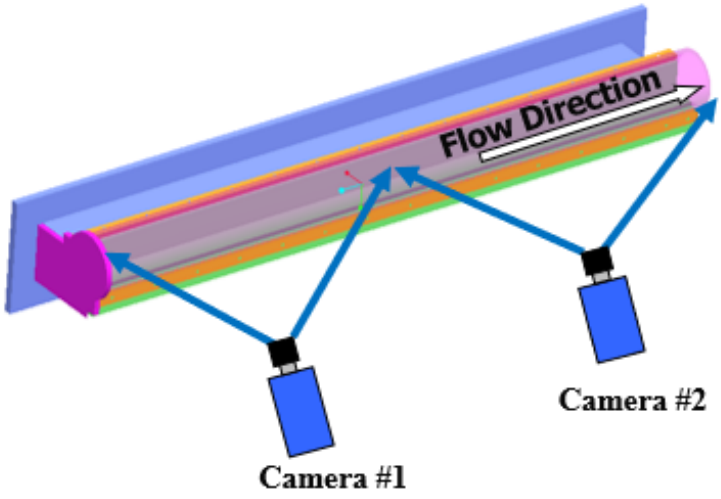


Figure 3-12: Painted test article heat transfer data collection by two cameras.

Once the green time image is calculated, then the probe locations are associated with columns of temperature readings in the temperature probe data file. Noise is edited out with an eraser image mask, followed by the region of interest definition using a polygon mask. These final images are then exported as JPEG image files. Cameras recording in DV format are set up to view the liquid crystal coated surface of the test article, capturing 10 samples per second. The air flow rate is set as the liquid crystal transitions at 35$^{o}$C and regulator pressure at 6.89 KPa. Once the system is heat soaked, cameras start recording. When the paint has fully transitioned to blue, the cameras and data acquisition system are stopped manually.

### 3.2.5. Hardware

For the heat transfer experiment number two, the TLC data are collected using two Sony video cameras connected to two PCs with IEEE 1394 cables; one VXI EX1048 (VXI)

temperature scanner, as shown in Figure 3-12. An ADN Series of AC-DC power supplies total power range of 120 to 480 Watts.

# CHAPTER 4 EXPERIMENTAL PROCEDURES

To establish the effectiveness of the current acrylic cylindrical chamber, 33 data points were taken at the cross-sectional area at the middle of the air inlets and between air inlets. Furthermore, cameras must be perfectly perpendicular to the measurement plane to achieve the best images. The easiest way to achieve this is to ensure the cameras are perpendicular to their stands and then make the stand parallel to the cylindrical chamber.

## 4.1. Vortex Flow Cooling Study with and without Elbow

The cylindrical chamber is attached to the plenum and Olive oil seeder and mounted on a non-rotating horizontal stage which is driven by a stepper motor and a Warner electric linear actuator. Each motor, camera, and laser are connected to an indexer which in turn communicates with a computer and LaVision software. The test article section is aligned to the laser, two cameras, stepper motor, and traverse system, as shown in Figure 3-7. It is important to note, for the purpose of later discussion, that similar to the actual engine blade, the coolant supply plenum is dead ended, while the cylindrical chamber, simulating a leading edge, is a through flow channel with a 90$^{o}$ turning elbow. The air is opened to mix with the seeder olive oil droplets at a set mass flow after one minute, the laser is turned on, lights are turned off, and then LaVision takes one data point at a time. Each step is measured by an optical encoder mounted in the

rear end of the shaft that allows each step to be exactly 19.81mm. Data points are taken at each step by the two high-speed and high-resolution CCD cameras capturing images of the illuminated PIV particles at a rate of 100 frames per second. With that frame rate, 2000 images are acquired over a period of 10 seconds, as shown in Figure 4-1. The datapoint reported here is from one cross-sectional area of the cylindrical chamber, capturing the vortex flow at a z/D location.

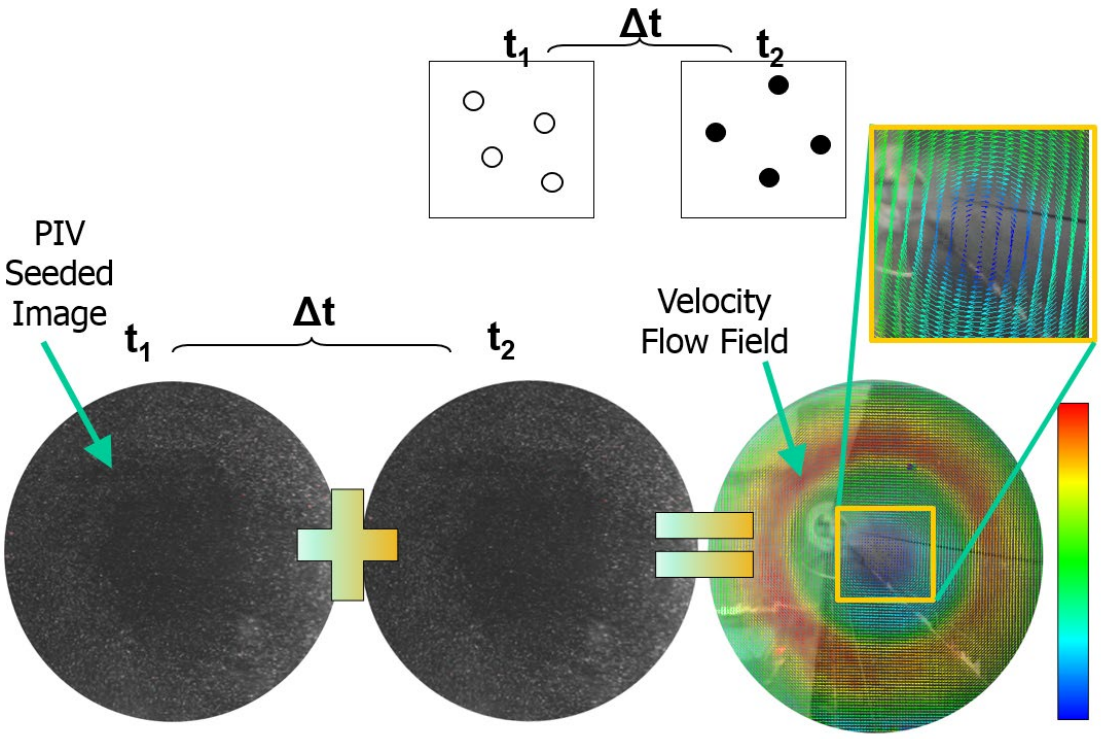


Figure 4-1: PIV seeded image and velocity flow field

Given this test section configuration, there were the following parametric variations available. Reynolds number varied by changing the mass flow and/or pressure. The Reynolds number is defined in terms of the total mass flow and cylindrical chamber diameter, as shown by Eq. (*4-1*), where $Q_s$ is the mass flow and $D_H$ is the hydraulic diameter of the air inlet.

$$Re_s = \frac{Q_S D_H}{\upsilon A} \quad (4\text{-}1)$$

## 4.2. TLC Heat Transfer Experiment

The TLC painted cylindrical chamber is attached to the plenum and aligned to the two high speed cameras. A heat exchanger is located between two of these plenums; as the air flows through the plenums air gets heated before it enters the air inlets. An in-house software is applied to synchronize the entire liquid crystal experiment. After the system is heat soaked to the required temperature, the data are collected by continuously polling. The data acquisition step size is 0.5 seconds and the VXI is set to a time interval of 0.2 seconds. The video file is converted to an AVI file, imported into the "Liquid Crystal Imagine Analyzer (LCIA)," as shown in Fig. 6, a Solar Turbines Incorporated program, and set to an intensity threshold of 0.7.

Once the green time image is calculated, then the probe locations are associated with columns of temperature readings in the temperature probe data file. Noise is edited out with an eraser image mask, followed by the region of interest definition using a polygon mask. These final images are then exported as JPEG image files. Cameras recording in DV format are set up to view the liquid crystal coated surface of the test article, capturing 10 samples per second. The air flow rate is set as the liquid crystal transitions at 35oC and regulator pressure at 6.89 KPa. Once the system is heat-soaked, cameras start recording. When the paint has fully transitioned to blue, the cameras and data acquisition system are stopped.

With the measured temperature distribution and the LCIA calculated heat transfer coefficients, the determination of the local Nusselt number proceeds as follows. Spatially

resolved temperature distributions along the cylindrical chamber concave surface are determined using infrared imaging in conjunction with thermocouples, energy balances, and digital image processing. This experiment is accomplished as the camera views the test article surface changing colors, from black to green. Reflection and radiation from surrounding laboratory sources are minimized using a black blanket, which covers the plenums. During this procedure, the cameras are focused, and rigidly mounted and oriented relative to the test article surface in the same way as when liquid crystals change colors, as shown in Figure 3-11. The Nu number for a forced convection in turbulent pipe flow is defined in (*4-2*).

$$Nu_D = \frac{\left(\frac{f}{8}\right)(Re_D - 1{,}000)Pr}{1+12.7\,(f/8)^{1/2}\,(Pr^{\frac{2}{3}}-1)} \qquad (4\text{-}2)$$

# CHAPTER 5 UNCERTAINTY ESTIMATES

Uncertainty estimates are based on 95 percent confidence levels and determined using procedures described by B. Weineke [84]. Uncertainty of temperatures measured with thermocouples is ±0.15°C. The uncertainties of total pressure and static pressure (relative to atmospheric pressure) are ±0.40% and ±0.20% in Pascals, respectively. Nusselt number uncertainty is about 10%, determined using infrared imaging in conjunction with thermocouple measurements, energy balances, digital image processing, and in situ calibration procedures. It does not include uncertainty related to installation and experimental setup. Reynolds number uncertainty is ±410, or about 2.5 percent for Reynolds number equal to 14,000.

# CHAPTER 6 EXPERIMENTAL RESULTS AND DISCUSSION

## 6.1. Experimental Results of Cylindrical Chamber with and without Elbow

The ability to utilize advanced techniques such as Stereo-PIV is essential for the detailed characterization of the flow field associated with turbine blade internal cooling systems. The flow field measurements from a vortex chamber are presented for three Re = 7,000, 14,000, and 21,000. In reference to the targeted Re numbers in Table 6-1, the actual Re numbers were calculated from the measured flow rate, resulting in Re = 6,911, 13,639, and 20,228, respectively. The data points were taken at 33 locations at a distance of 19.81 mm from each other, as shown in *Figure 6-1*. Data were collected at both locations, in between air inlets and at the middle of the air inlets (i.e., data point #2 and data point #4, respectively) to show the complicated flow and its variation. Three Re numbers and flow rate measurements from 7,000 to 21,000 were plotted for all velocity profiles and for the TLC experiment as listed in Table 6-1. The nominal Reynolds number represents the average flow rate; also, ±50% is presented.

*Table 6-1: Reynolds Number and Mass Flow Rate.*

| Test Case | Reynolds Number | Flow Rate (kg/s) |
|---|---|---|
| +50% | 21,000 | 0.06291 |
| Nominal | 14,000 | 0.04179 |
| -50% | 7,000 | 0.02108 |

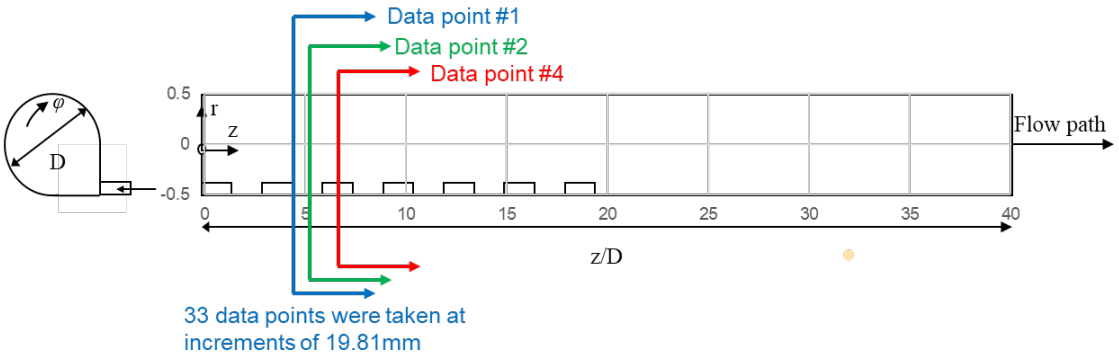


Figure 6-1: Data point locations in increments of 19.81 mm.

The length of the cylindrical chamber is divided in small slides to capture the vortex flow details. From z/D 0 – 4.5 there were no data points taken because the left side of the cylindrical chamber was not visible enough to capture the cross-sectional area of the flow field. A total of 33 data points were taken, the first data point located z/D = 4.5. Figure *6-2* presents examples of the data points taken along the length of the cylindrical chamber. Data points presented in this section come from all 33 data points taken and in case of the Tecplot 360 visualization, data interpolation is applied from data point to data point. Interpolation is a type of estimation method of constructing new data points within the range of a discrete set of known data points. Tecplot 360 uses linear interpolation, which generally takes two data points to solve Eq. (*6-1*).

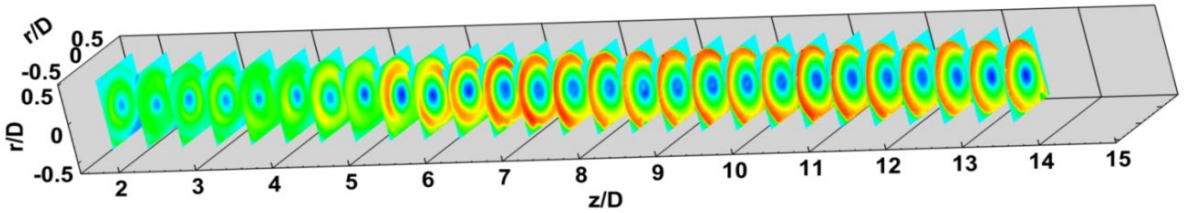


Figure 6-2: Cross-sectional area of data points.

$$y = y_a + (y_b - y_a)\frac{x - x_a}{x_b - x_a} \; at \; the \; point \; (x, y) \quad (6\text{-}1)$$

## 6.2. Cylindrical Chamber without Elbow Results and Discussion

### 6.2.1. Swirl Number Results

Swirl Number, $S_N$, is the flux of angular momentum divided by the flux of axial momentum, as shown in ( *6-2*). Three Re numbers (nominal and ±50%) are presented at Re = 7,000, 14,000, and 21,000. The data points are taken at 33 locations within 19.81 mm distance from each other throughout the length of the cylindrical chamber. All data are collected in the middle of the air inlets and in between air inlets, as shown in Figure 6-1.

$$S_N = \frac{\int_{r=0}^{R} \rho V_\emptyset V_z 2\pi r^2 dr}{R \int_{r=0}^{R} \rho V_z^2 2\pi r dr} \quad (6\text{-}2)$$

The Swirl Number ($S_N$), from the vortex flows, is normally classified as vortex flows in which the tangential velocity distribution is constant. When the fluid friction is low, and the radial flux of angular momentum is high, the fluid executes a vortex motion. Studies by Hedlund et al. [8] and Moon et al. [2] define the swirl number as the relation of the flux of angular momentum and the flux of axial momentum (with respect to the vortex chamber cylinder axis), as seen in Eq. ( *6-2*).

The end goal of the research centers on a critical discussion of the data needed to obtain the radial variations of the axial and angular momentum. The $S_N$ study is conducted for three different air flow rates corresponding to a Reynolds number range of 7,000 to 21,000, as shown in Figure 6-3, which shows the air inlets have a large effect on the $S_N$,

as the vortex peaks are higher at each air inlet. The $S_N$ is particularly high near the second air inlet, which is located at z/D from 1 to 3, due to the proximity of the first two air inlets to one vortex chamber and its face, which restricts the axial component of the flow. Consequently, the axial flow momentum result is comparatively small in this portion of the chamber giving high $S_N$.

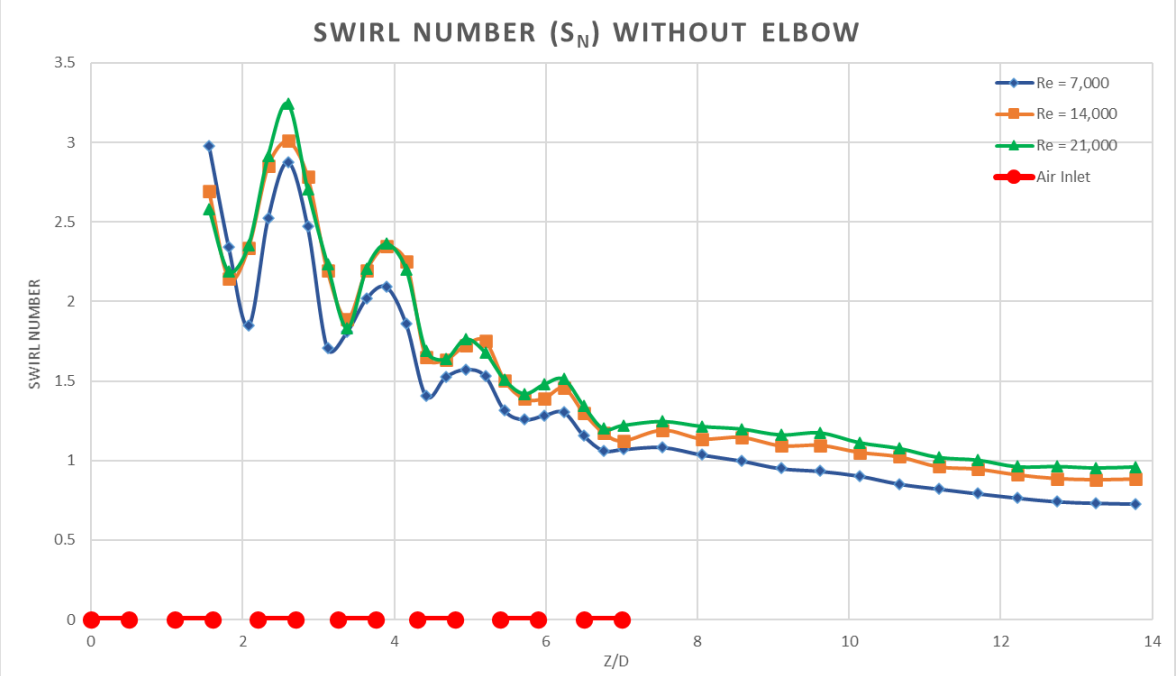


Figure 6-3: Swirl Number of cylindrical chamber without elbow.

The $S_N$ values shown in Figure 6-3 decrease at downstream chamber axial locations as z/D increases and regional axial velocities become more extensive. The $S_N$ increase at each air inlet is further observed; vortex peaks are much higher at these locations than those with no air inlets. At z/D from 1 to 3, where the second air inlet is located, the $S_N$ is particularly high. One reason is because of the proximity of the first two air inlets to one vortex chamber and face restricts the axial component of the flow. Consequently, the axial flow momentum is relatively small at this location, given a high

vortex number along the air inlet length. Downstream, where z/D = 7-15, $S_N$ magnitudes seem to steadily decrease as the exit of the chamber is approached. The $S_N$ values measured near the third inlet located at z/D = 2-4 are consistent with this trend, due to the influence of the flow turning just after it leaves the air inlet, and because of velocities in the axial direction. The maximum $S_N$ produced at Re = 21,000 is 3.3, indicating that at these locations a high flux circumferential momentum relative to flux axial momentum exists.

### 6.2.2. Circumferential Velocity Distribution

The experimental measurements of the circumferential and axial velocities distribution were collected with Stereo-PIV, solved by MATLAB, and plotted using Techplot 360. The circumferential velocity decreases and maximum circumferential velocity shifts towards the center of the vortex chamber with downstream distance. At the outer wall region, the axial velocity is higher and increases within the chamber length. By the second half of the chamber length, the axial velocity reaches its maximum. Another observation is that the magnitude of the vorticity increases closer to the wall and downstream chamber length. Also, the turbulent kinetic energy in the axial rms is similar to the tangential rms, with the exception being the axial rms is generally lower throughout the chamber length. The vortex increases are visible from air inlet numbers two through seven and, as predicted, later $S_N$ decreases as there are no more air inlets. Research shows that the $S_N$ is largely dependent on tangential injection. Such variations are entirely consistent with surveys of time-averaged circumferential velocity, axial velocity, circumferential vorticity, and turbulent kinetic energy. Also, flow near the inlets is observed to intensify $S_N$ produced by the shear layer near the edge of the air inlet.

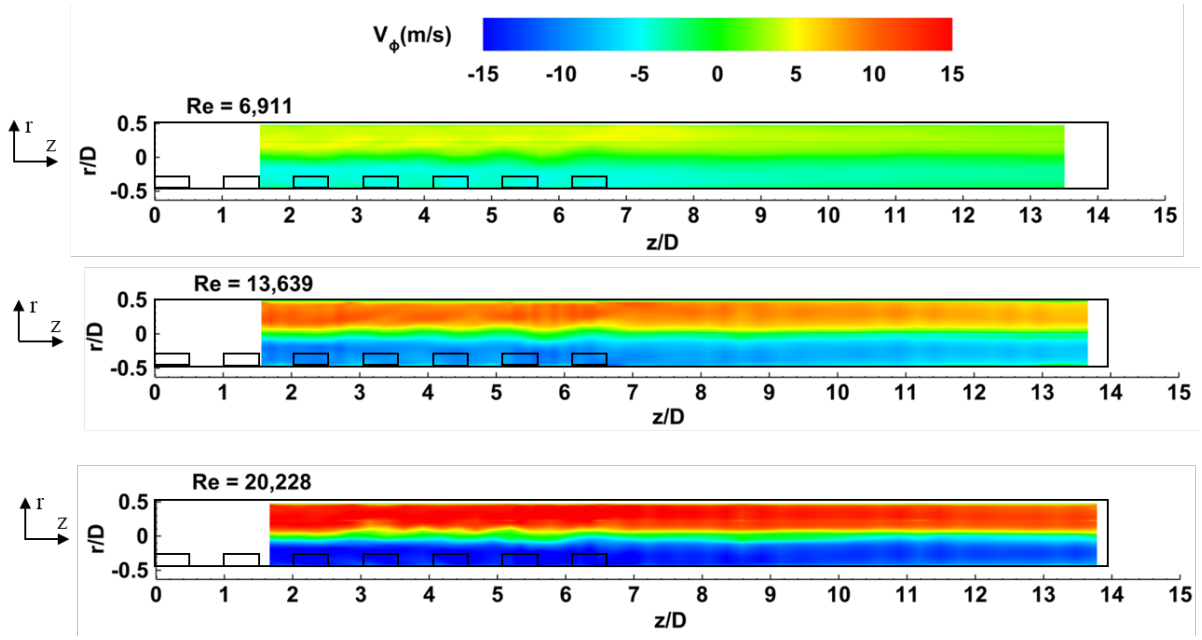


Figure 6-4: Circumferential velocity distribution of cylindrical chamber without elbow at all three Re numbers.

The circumferential velocity, Vϕ, results showed that velocity grows with increasing radial distance, making it the biggest element of the velocity vector. Also, results show Vϕ decreases near the chamber wall. The three Re numbers are plotted and their Vϕ ranges from -15 to 15 m/s shown in Figure 6-4. One observation is that the maximum velocity magnitude decreases with distance from air inlets as the result of the viscous and turbulent dissipation. Another observation is that the maximum Vϕ shifts towards the center of the tube with downstream distance.

### 6.2.3. Axial Velocity Distribution

As the Re number increases, the axial velocity, $V_Z$, intensifies, measuring higher on the outer wall region, as shown in Figure 6-5. From upstream to downstream, the $V_Z$ ranges from -2 to 7 m/s in all three Re numbers, as is expected in a cylindrical chamber.

The outer wall region velocity increases across the length, reaching a maximum velocity at the second half of the vortex chamber. Another observation is the high $V_Z$ in the direction of the outer wall region. Between the core and the chamber wall in the outer wall region, an inertia-driven vortex was observed and measured a flow field pattern that is critically different between high to low Re numbers.

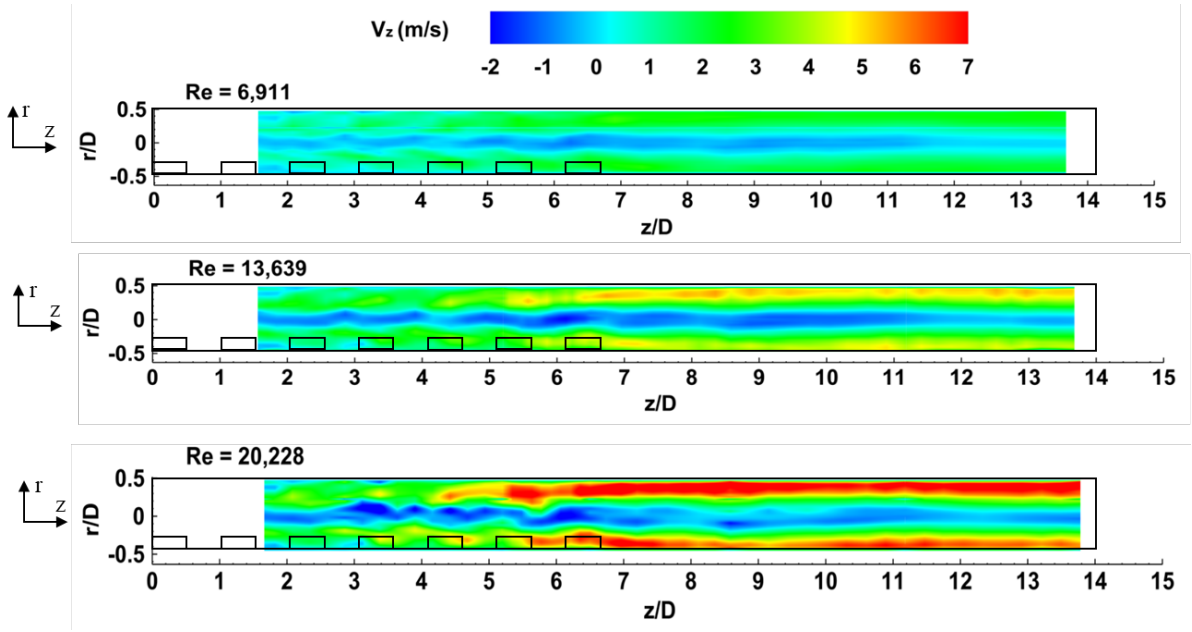


Figure 6-5: Axial velocity distribution of cylindrical chamber without elbow at all three Re numbers.

### 6.2.4. Reverse Vortex Flow at the Center of the Cylindrical Chamber

With this geometry, the vortex flow cooling has important axial and circumferential components of velocity, and the overall flow pattern through the cylindrical chamber behaves similar to a vortex tube, also known as the Ranque-Hilsch vortex tube, a mechanical device that separates a compressed air into hot and cold streams with temperature difference reaching over 250°C. Although unintended, the detailed flow behavior inside a Ranque-Hilsch vortex tube and flow reversal in the cylindrical chamber

share similitudes. The velocity profile was measured for both air and water operated Ranque-Hilsch vortex tube. Based on this study, there was a remarkable agreement between theoretical estimation and experimental results. Furthermore, the unintended consequence of the vortex flow behavior needed more analysis; utilizing 3-D stereo-PIV at the nominal Re = 13,639, three cross-sectional areas were chosen. Figure 6-6 shows the three cross-sectional areas z/D = 3, 6, and 13 carefully studied looking for evidence of the reverse flow and captured it and all three cross-sectional areas to show reverse flow. Stereo-PIV is a powerful tool able to capture in great detail how each droplet behaves and map the axial velocity field flow. The discovery of this unintended behavior is so astronomically important that more research and analysis had to be completed to satisfy the minds of the experts.

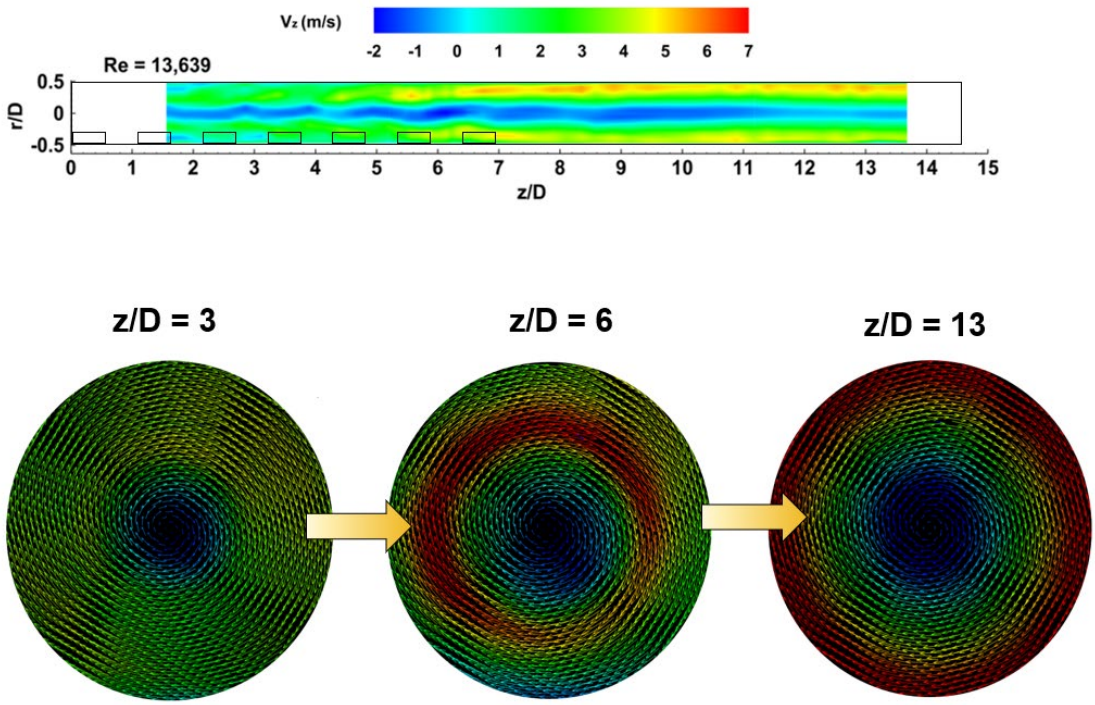


Figure 6-6: 3-D stereo-PIV cross-sectional areas at z/D = 3, 6, and 13.

The next step is to understand the vortex flow behavior where the reverse flow exists. The original premise was that the $S_N$ was the $S_{N\_critical}$, as shown in Figure 6-7. The axial velocity from 3-D stereo-PIV results disproved this premise.

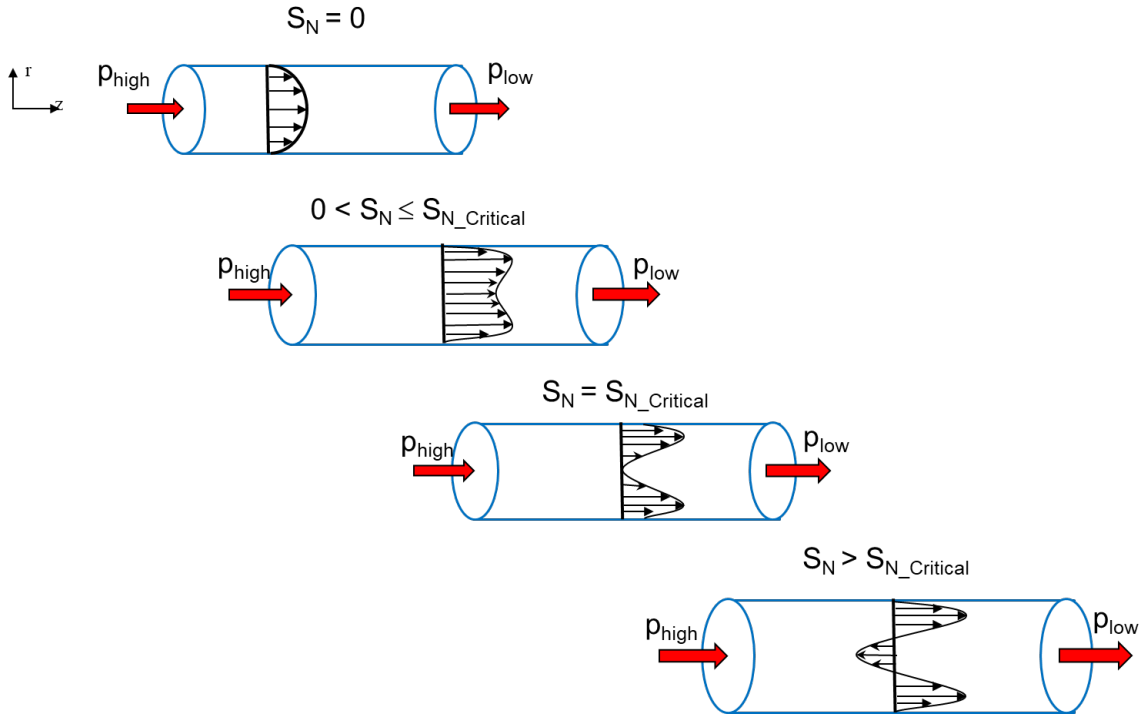


Figure 6-7:The Swirl number behavior in a cylindrical chamber.

### 6.2.5. Navier-Stoke Equation

One way to check that the reverse flow manifest in the cylindrical chamber is to apply the Navier-Stokes, Centrifugal Force, and Centrifugal Velocity equations:

$$\rho\left(\frac{\partial v_r}{\partial t}+ v_r\frac{\partial v_r}{\partial r}+\frac{v_\theta}{r}\frac{\partial v_r}{\partial \theta}-\frac{{v_\theta}^2}{r}+v_z\frac{\partial v_r}{\partial z}\right)=\rho g_r-\frac{\partial p}{\partial r}+\mu\left\{\frac{\partial}{\partial r}\left(\frac{1}{r}\frac{\partial}{\partial r}[rv_r]\right)+\frac{1}{r^2}\frac{\partial^2 v_r}{\partial \theta^2}-\frac{2}{r^2}\frac{\partial v_\theta}{\partial \theta}+\frac{\partial^2 v_r}{\partial z^2}\right\} \quad (6\text{-}3)$$

$$F=m\omega^2 r=\frac{mv^2}{r} \quad (6\text{-}4)$$

$$v=r\omega \quad (6\text{-}5)$$

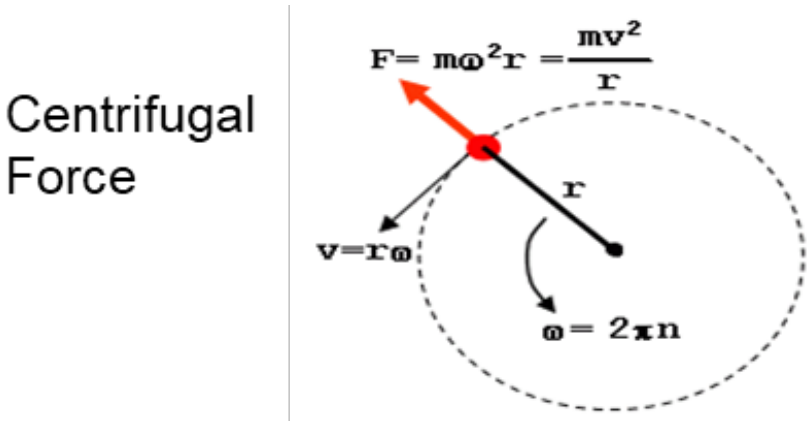


Figure 6-8: Centrifugal Force Schematic.

For the Navier-Stoke equation the following assumptions were made:

- $v_z$=0 and $\frac{\partial}{\partial z}$= 0, because no flow or variation of properties in the z-direction.
- $\rho g_r$ = 0, because there is no body force, no buoyancy and is homogeneous.
- $v_r$=0, because r-component direction.
- $\frac{\partial}{\partial \theta}$=0, because circumferentially symmetric flow, properties do not vary with $\theta$.

Therefore, Navier-Stoke equation reduced to:

$$\frac{\partial p}{\partial r} \sim \rho \frac{{v_\theta}^2}{r} \tag{6-6}$$

Once preliminary values were entered, the results were a radial pressure drop estimate of 140 Pa, which is comparable to the gauge pressure at the inlet of approximately 340 Pa. Clearly illustrated by figure.

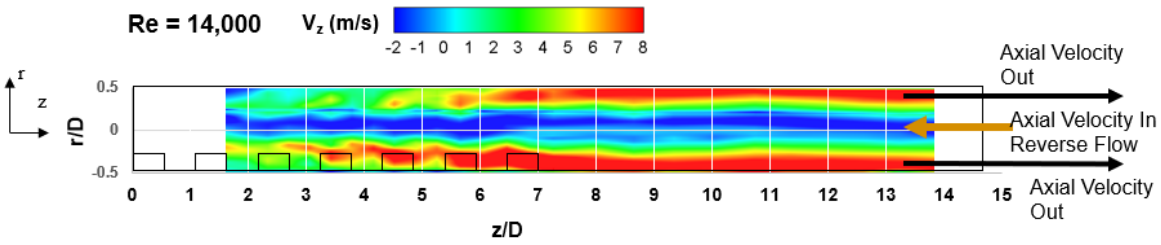


Figure 6-9: Radial pressure drop estimate.

The investigation continues with the data acquisition, this step allows a view of each droplet's axial velocity measurement to make sure the data can tell the same story of the reverse flow. The plot shows 12 data points collected at Re = 13,639 and plotted using Excel, as shown in Figure 6-10. The plot does tell the same story: reverse flow is visible, indicating the high pressure at the center of the cylindrical chamber traveling upstream. The reverse flow covers about one-third of the cylindrical chamber diameter. Additionally, the axial velocity peaks, along the tube, gets closer to the wall downstream as expected. The reverse flow is approximately 20% of tube diameter, near the centerline and the magnitude of outer-wall velocity increases after the last air inlet.

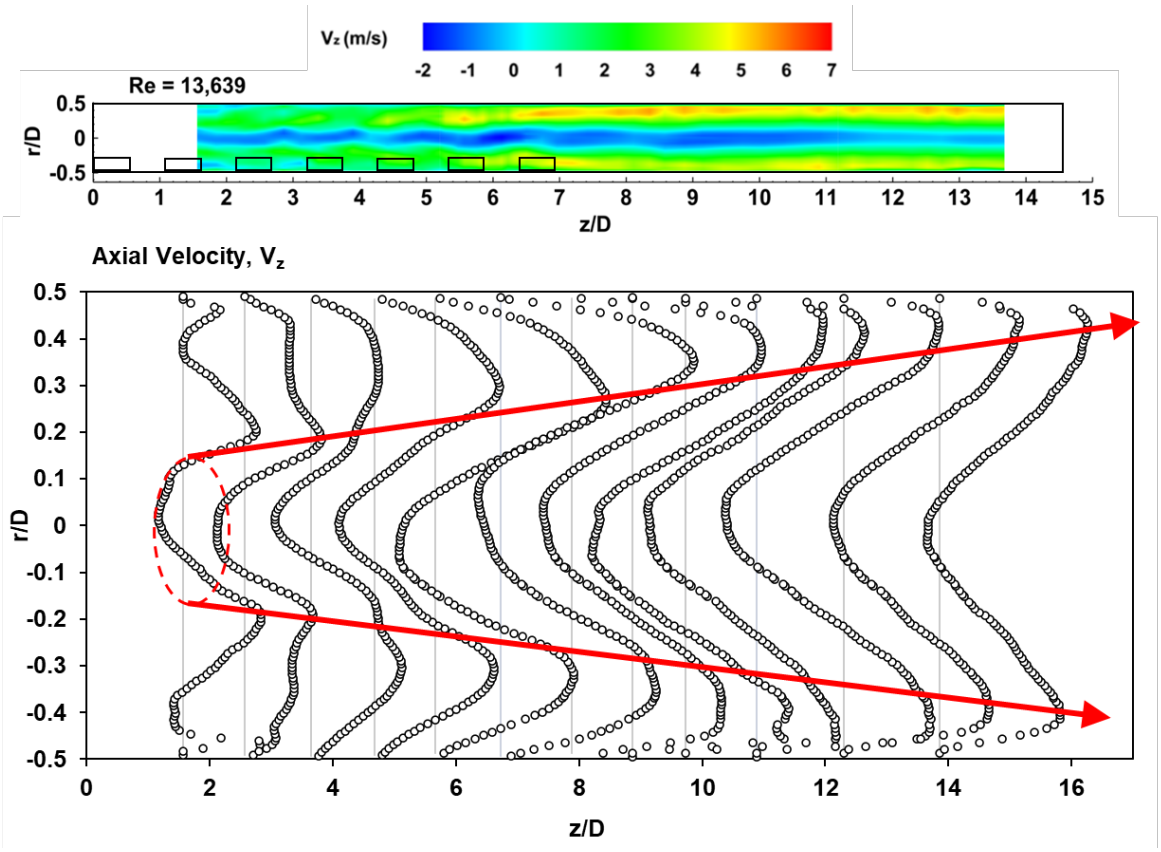


Figure 6-10: Axial velocity distribution at 12 data points of cylindrical chamber without elbow.

Next a video of the vortex flow cooling was taken. The goal was to insert a wire with a piece of light string attached at the end of the wire. The wire is then inserted at three different locations to see the string behavior, as shown in Figure 6-11, at all three locations the string moves in the direction the flow is moving, once again showing that the reverse flow is moving towards the upstream.

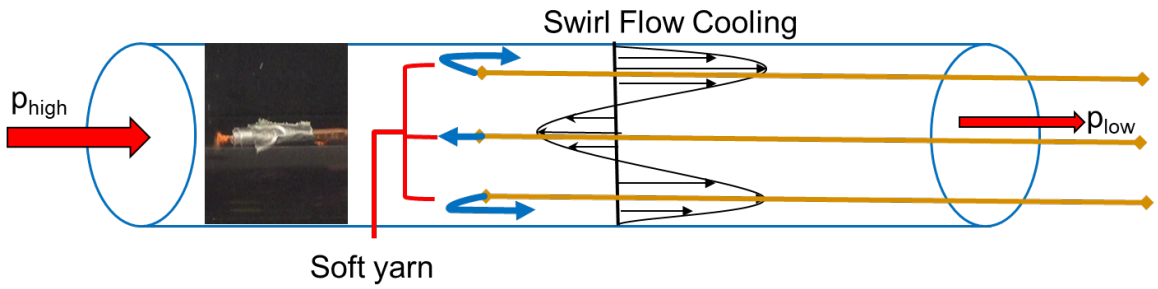


Figure 6-11: Video evidence of the reverse vortex flow using a wire and a soft yarn attached.

Another way to check if the reverse flow exists is to analyze the mass flow rate versus the z-distance, as seen in Figure 6-12. The goal is to plot the mass flow rate at all three Re numbers to verify that the mass flow rate going into the cylindrical chamber to create the vortex flow cooling matches the mass flow rate going out of the chamber. The mass flow rate and axial velocity equations are:

$$Q = AV_{z-avg}, where\ the\ V_{z-avg} = \frac{2}{r^2}\int V(r)r\,dr \quad (6\text{-}7)$$

As figure shows the mass flow rate going into the cylindrical chamber to create the vortex flow cooling matches the mass flow rate going out of the chamber, therefore the reverse vortex flow transpires inside the cylindrical chamber.

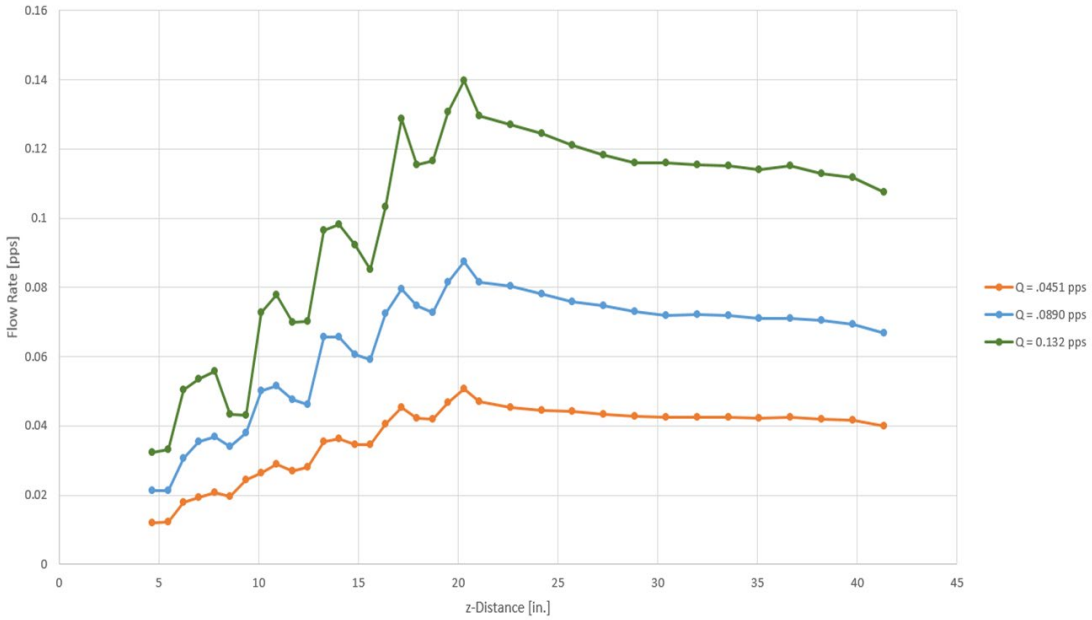


Figure 6-12: Mass flow rate vs. z-Distance at all three Re numbers of cylindrical chamber without elbow.

### 6.1.1. Vorticity Propagation

The vorticity is the rotating motion of the fluid and measurements taken at closely spaced locations with non-intrusive techniques to ensure accurate vorticity results. Eq. (*6-8*). Figure 6-13 data shows that vorticity increases closer to the wall due to the frictional effects and results, and also reveals that at Re = 6,911 the vorticity ranges from 10 to -60; at nominal Re = 13,639 the range increases from 25 to -125; and finally, when Re = 20,228, the vorticity ranges from 50 to -200. The rotating vortex in the stereo-PIV can be easily detected and is seen shrinking to the core within the chamber length, with a slight increase in magnitude.

$$\vec{\omega} = \vec{\nabla} \, x \, \vec{v} \qquad (6\text{-}8)$$

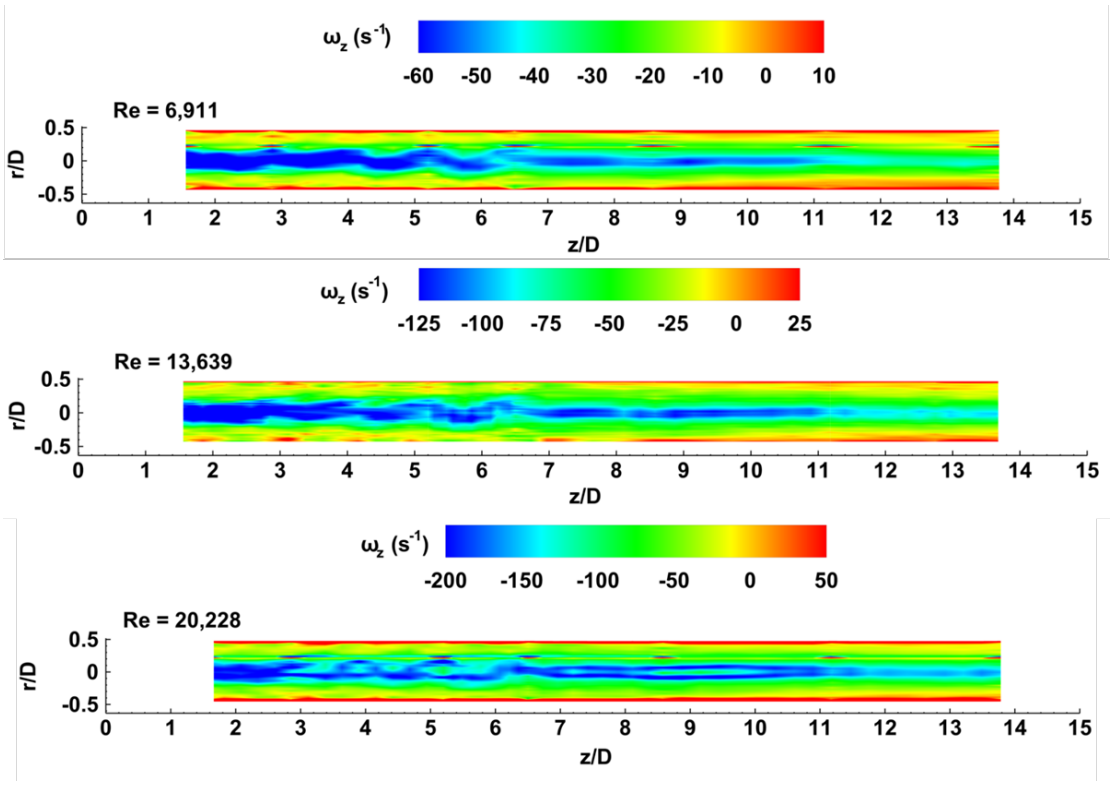


Figure 6-13: Vorticity of the cylindrical chamber without elbow.

### 6.1.2. Turbulent Intensity Propagation

The turbulence intensity associated with eddies in the turbulent flow is calculated by the medium kinetic energy per unit mass. In other words, turbulent kinetic energy is defined as the sum of the square of the velocity fluctuations equivalent to the rms (root-mean-square), as shown in Eq. (*6-9*). The turbulent kinetic energy allocation in Figure 6-14 provides a more comprehensive view of the large-scale turbulence that occurs in the vortex chamber. The highest absolute velocity transpires through the tangential component that influences the outer-wall region of the chamber and where the radial component is accountable for the core assembly.

$$k = \frac{1}{2}\left(V_{r,rms}^2 + V_{\phi,rms}^2 + V_{z,rms}^2\right) \quad (6\text{-}9)$$

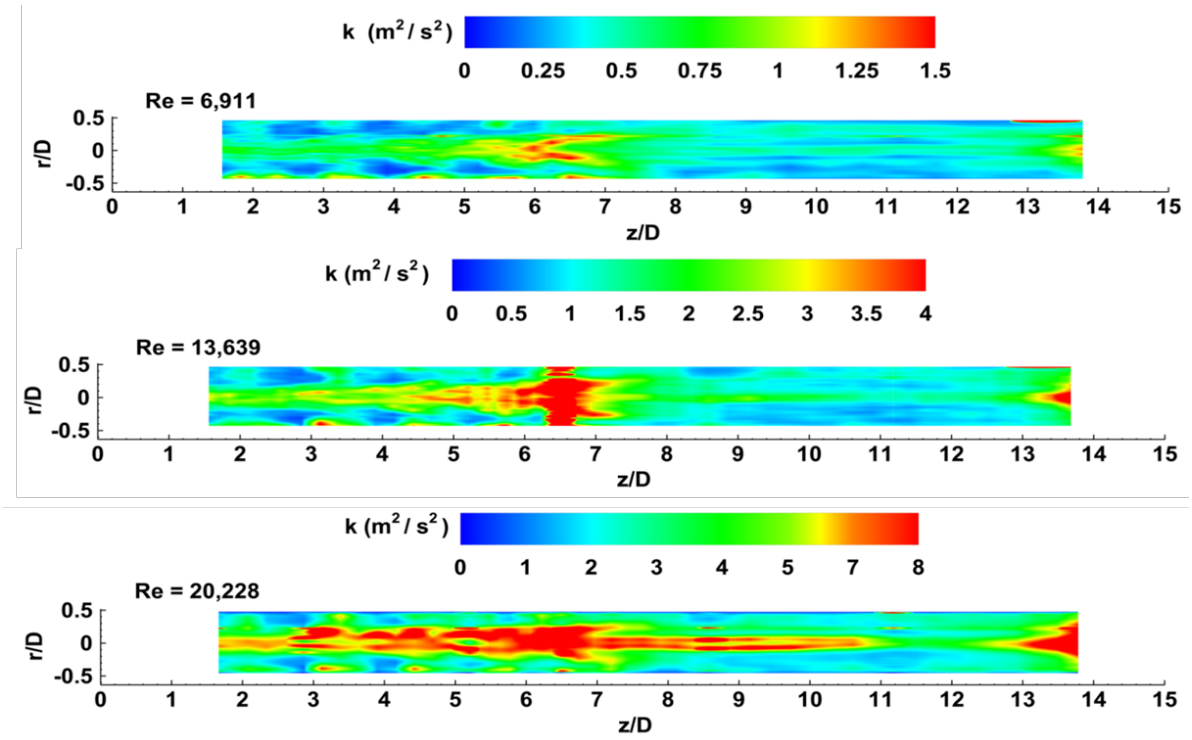


Figure 6-14: Turbulent intensity of the cylindrical chamber without elbow.

## 6.2. Cylindrical Chamber with Elbow Results and Discussion

This original approach will yield knowledge about velocity distribution using a cylindrical chamber with an elbow that best represents the geometry of a turbine blade; quantitative correlations among Nu number, circumferential and axial velocity fields, and $S_N$; and advantageous Nu number that provides optimum heat transfer and highest $S_N$. This experimental study is creative and original because it addresses critical knowledge gaps in internal vortex flow cooling systems for the first stage of the turbine blade. By examining the trend of investigations relating to internal vortex flow cooling phenomena, one key trend is apparent: the movement away from experimental investigation and substantial increase in computational investigation due to the desire for quick, easy, and affordable means of quantifying vortex decay. However, a history of failed computational

analyses has proven that the true characteristics of vortex flow cooling, a great example is the newly found reverse flow in the inner core that has been discovered in earlier experiments are not easily captured by traditional turbulent models. Validating this research solution will allow the vortex flow cooling to be more thermally efficient by correlating the advantageous Nu number and $S_N$ distribution.

Part one of the experimental study was without the elbow, which allowed a better understanding of the test article, material, seeder, hardware, and software. However, to intentionally validate the true behavior of the vortex flow cooling, one must design a test article that truly represents the internal cooling design of a turbine blade. Therefore, for the next experiment, the test article comprises a cylindrical chamber with an elbow, and the same exact dimensions as the previous model, as well as the same material, hardware, and software.

The schematic of the cylindrical chamber attached to the elbow used for vortex flow cooling is shown in Figure 6-15. The air mixed with olive oil droplets passes through the plenums and makes its way into the acrylic cylindrical chamber via the air inlets to generate the vortex flow cooling.

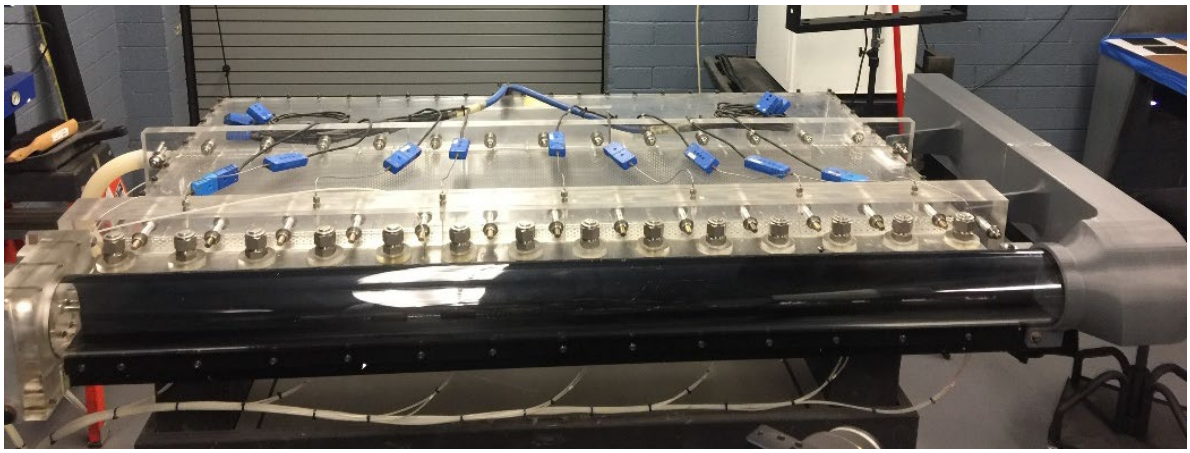

Figure 6-15: Cylindrical chamber with elbow attached.

For this part of the experiment the same procedure as experiment one is implemented. The same instrumentation, hardware, software, and calibration are employed. All 33 data points measurements are obtained utilizing 3-D stereo-PIV, data acquisition is process by LaVision software, data files are transfer to MATLAB for further l=clean up, then Tecplot 360 for data visualization.

### 6.2.1. Swirl Number Outcomes

Three Re numbers (nominal and ±50%) are presented at Re = 7,000, 14,000, and 21,000. The data points are taken at 33 locations within a short distance from each other. All data points are collected either in the middle of the air inlets and in between air inlets, as shown in Figure 6-1. The $S_N$ distribution is presented in Figure 6-16, where the $S_N$ peaks are decreasing at downstream chamber axial locations as z/D increases. Magnitudes of the $S_N$ are quite high between air inlet two and three because of the proximity of this inlet to one air inlet end face, which restricts the axial component of the vortex flow. As a result, axial flow momentum is relatively small in this section of the cylindrical chamber, giving high $S_N$ results. Between z/D = 7 and 15, $S_N$ magnitudes seem

to be steadily decreasing, lower $S_N$ results contribute to the local axial velocities becoming more significant. The maximum $S_N$ produced at Re = 21,000 is 3.3, indicating that at these locations a high flux circumferential momentum relative to flux axial momentum exists [88].

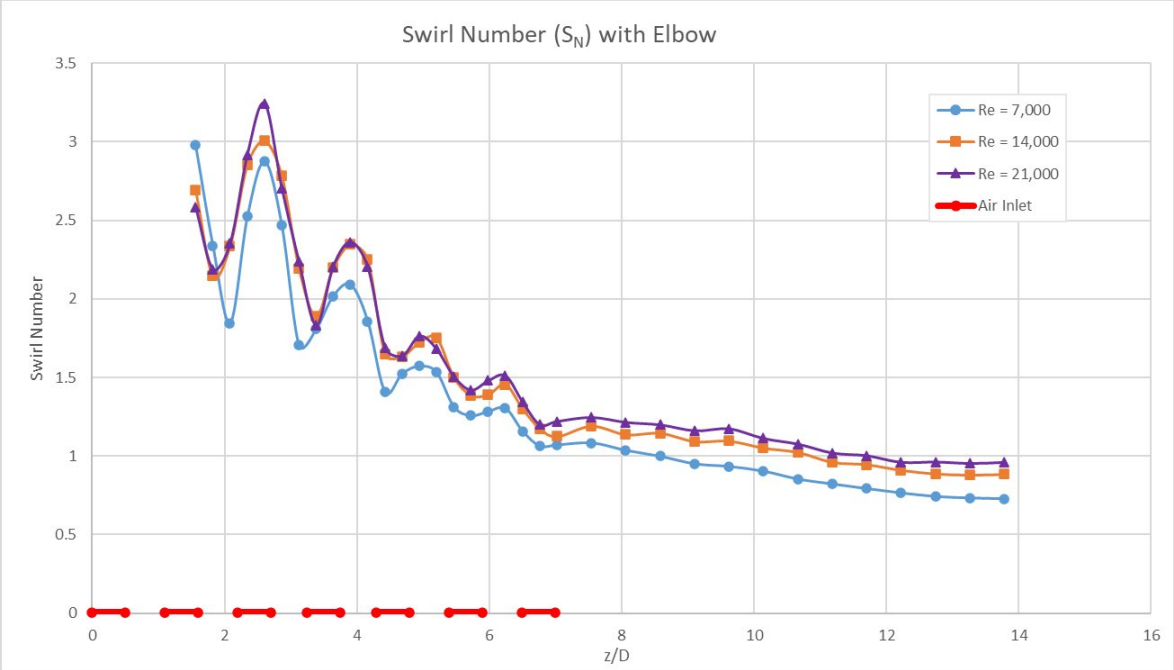


Figure 6-16: Swirl Number distribution of cylindrical chamber with elbow.

### 6.2.2. Circumferential Velocity Outcomes

The experiment shows that the circumferential velocity decreases downstream and that the maximum circumferential velocity shifts towards the center of the chamber with downstream distance. As anticipated the velocity is zero in the chamber axis, increases towards upstream and decreases again toward the chamber wall. The maximum velocity magnitude decreases with distance from the inlet because of viscous dissipation, as shown in Figure 6-17.

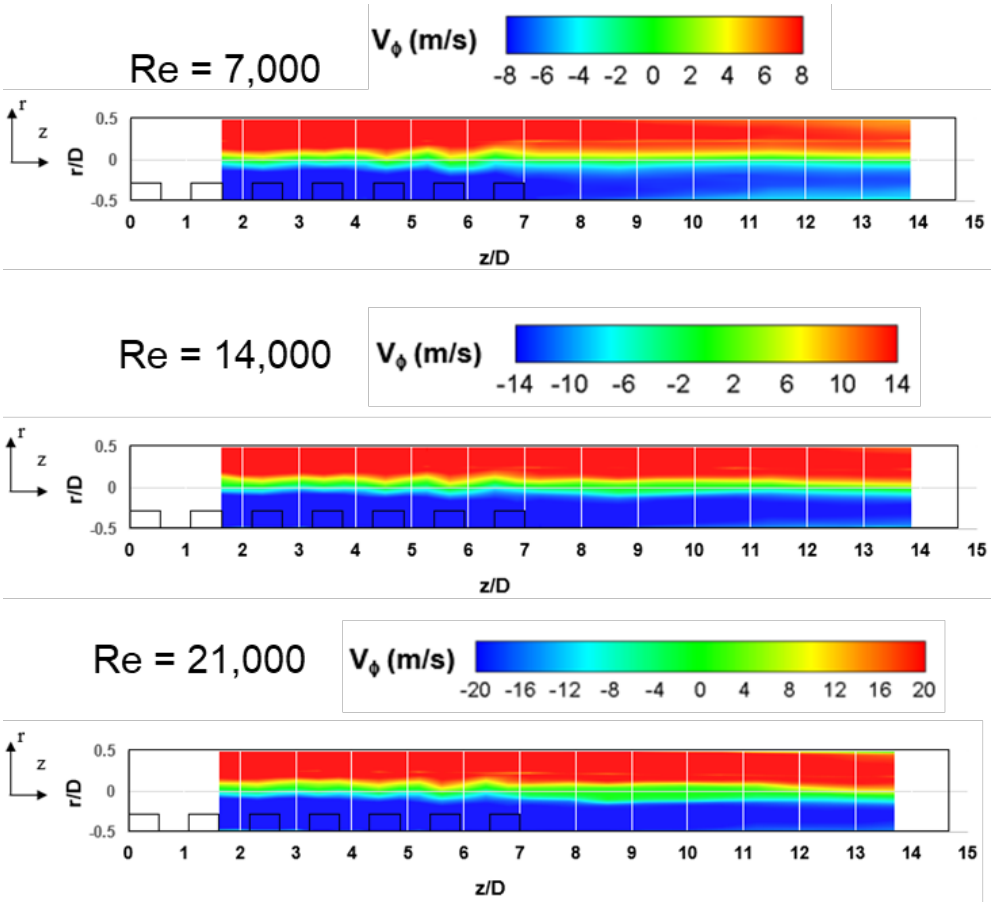


Figure 6-17: Circumferential velocity distribution of the cylindrical chamber with elbow.

### 6.2.3. Axial Velocity Outcomes

The axial velocity is higher towards the outer wall region and increases within the chamber length, reaching a maximum in the second half of the chamber. The Axial velocity ($V_z$) strengthens as Re number increases and expands toward the outer wall region as shown in Figure 6-18. The $V_z$ ranges between -1 and 5 m/s where the highest values are shown right at the middle of the cylindrical chamber right after air inlet number 7. At Re = 14,000, $V_Z$ ranges from -2 to 8 m/s as expected in a cylindrical chamber from upstream to downstream. The highest $V_z$ are observed at Re = 21,000 due to the fact there is more mass flow coming in allowing the Vz to stay well distributed along the

chambers wall. It is detected that the outer wall region velocity increases downstream and reaches a maximum in the second half of the chamber. Additionally, $V_Z$ is higher towards the outer wall region.

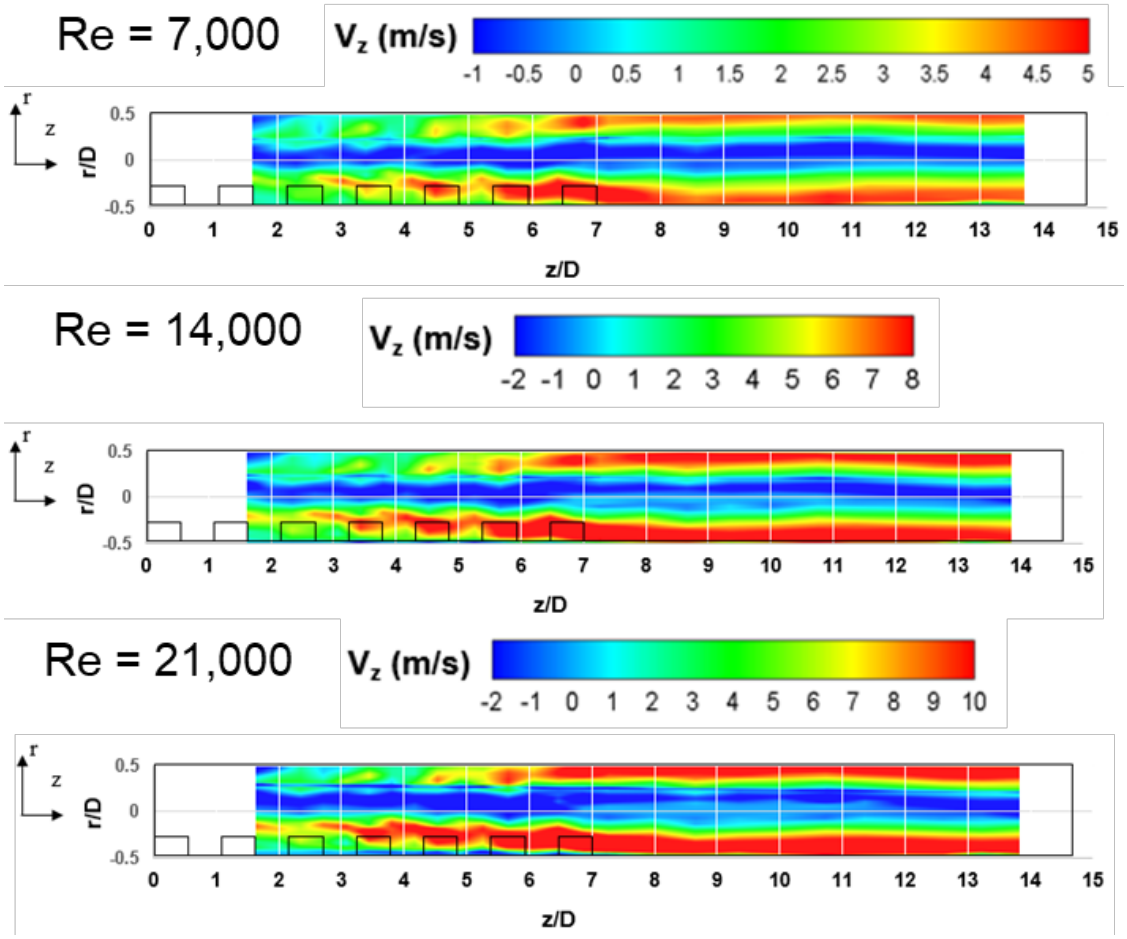


Figure 6-18: Axial velocity distribution of the cylindrical chamber with elbow.

Reverse flow was visible and checked with the same level of detail as done in experiment one without the elbow. Starting with 3-D Stereo-PIV velocity field shows the reverse flow. Followed by mass flow rate inspection and confirm that the mass flow rate going in is compatible to the mass flow rate going out.

### 6.2.4. Vorticity Magnitudes

Figure 6-19 data show that vorticity increases closer to the wall due to the frictional effects and results, and also reveal that at Re = 7,000 the vorticity ranges from 10 to -60; at nominal Re = 14,000 the range increases from 25 to -125; and finally, when Re = 21,000, the vorticity ranges from 50 to -200. The rotating vortex in the stereo-PIV can be easily detected and is seen shrinking to the core within the chamber length, with a slight increase in magnitude. Vorticity is less concentrated near the wall towards the downstream.

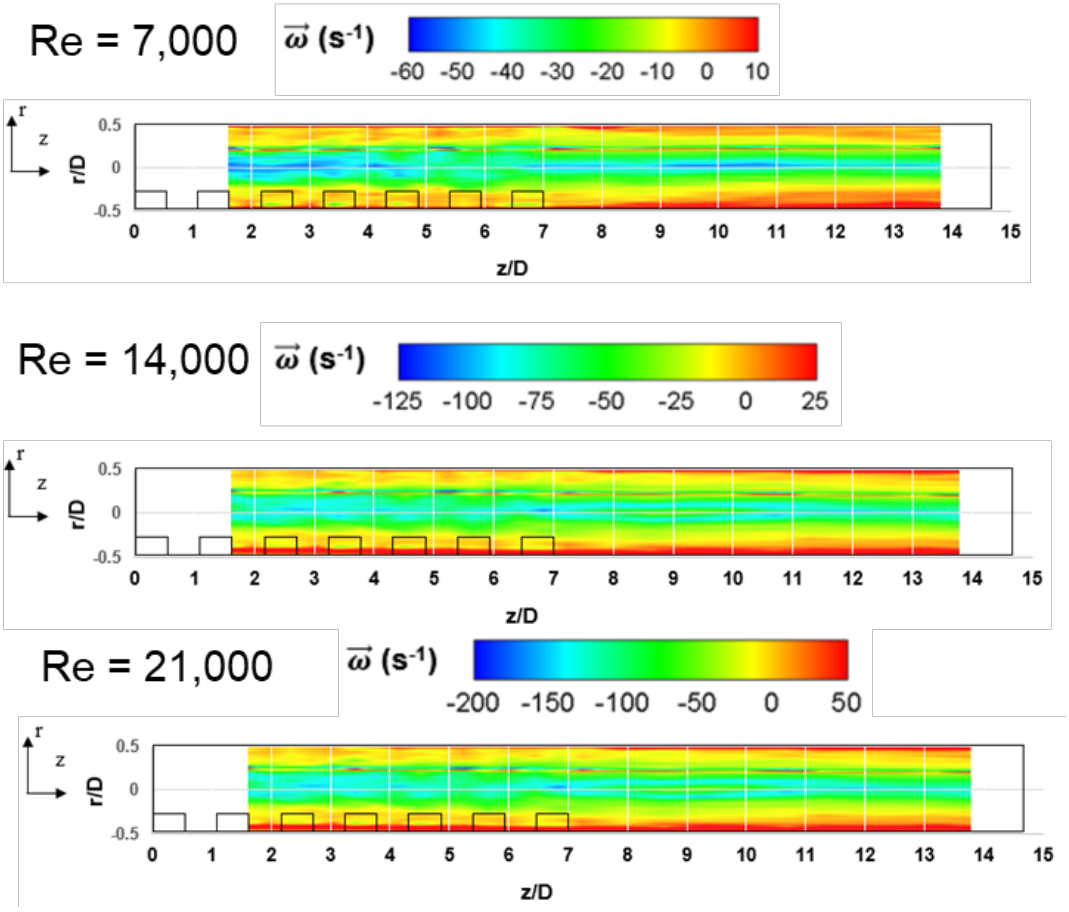


Figure 6-19: Vorticity magnitudes of the cylindrical chamber with elbow.

### 6.2.5. Turbulent Intensity Magnitudes

The distribution, as shown in Figure *6-20*, provides a detailed view where large-scale turbulence occurs in the chamber. Additionally, the individual rms components show their influence on these structures. The tangential component influences mostly the outlying chamber region, and the radial component is accountable for the core assembly, where the highest absolute velocity transpires.

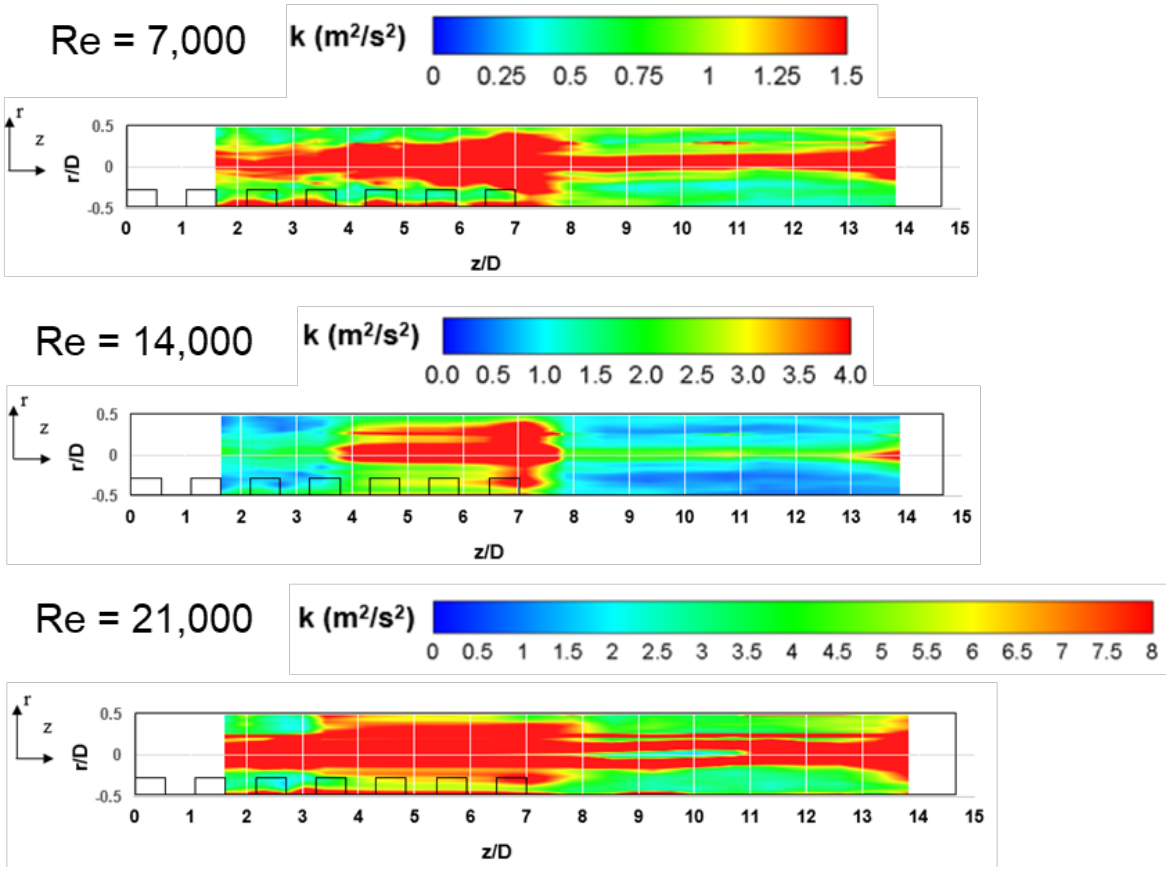


Figure 6-20: Turbulent intensity magnitudes of cylindrical chamber with elbow.

## 6.3. Comparison of Vortex Flow Cooling of Cylindrical Chamber with and without Elbow at Re = 7,000, 14,000, and 21,000

Comparison of vortex flow cooling behavior is shown to analyze the differences and similarities. These distributions and magnitudes are measured around the entire cross section of the cylindrical chamber circumference using the 3-D PIV at 33 data points as described earlier.

### 6.3.1. Swirl Number Comparison

Overall high $S_N$ results indicate proximity to the air inlet, which restricts the axial component of the flow. As a result, as shown in Figure *6-21*, axial flow momentum is relatively small in this portion of the cylindrical chamber, giving high $S_N$. Values as high as 3.5 and 2.5, with and without the elbow, respectively, indicate high nondimensional circumferential moment of momentum relative to non-dimensional axial momentum. The $S_N$ magnitudes with and without the elbow are decreasing gradually and steadily along the length of the chamber. The highest $S_N$ peak at z/D = 1.5, was measured when the cylindrical chamber has no elbow at 3.5. Therefore, the highest $S_N$ peak with elbow measured at z/D = 1.5, was 2.33.

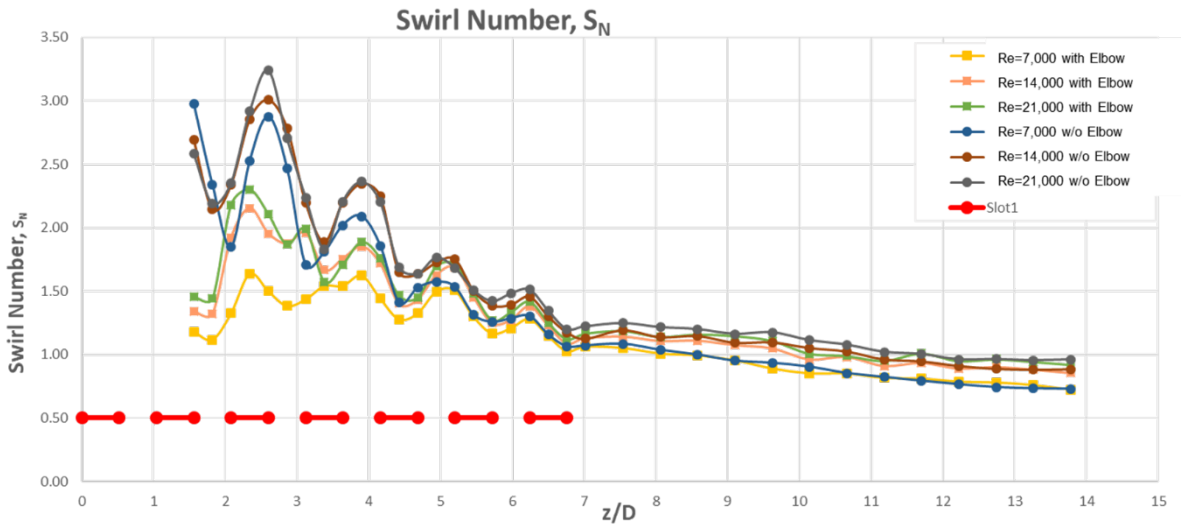


Figure 6-21: Swirl Number magnitudes of cylindrical chamber with and without elbow at all three Re numbers.

### 6.3.2. Circumferential Velocity Comparison

Figure 6-22 shows results of the cylindrical chamber with and without elbow circumferential velocity showing the magnitude of the outer-wall velocity increasing. The cylindrical chamber with an elbow circumferential velocity increase at a higher rate due to being the largest component of the velocity vector, a typical trend of vortex flow cooling.

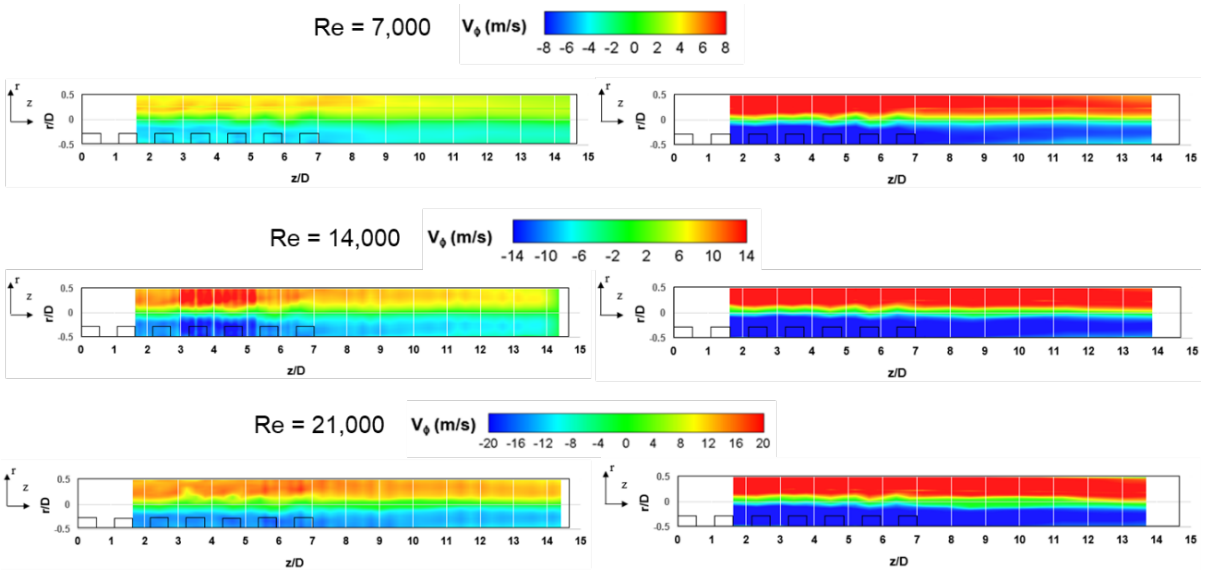


Figure 6-22: Circumferential velocity distribution of cylindrical chamber with and without elbow at all three Re numbers.

### 6.3.3. Axial Velocity Comparison

Figure 6-23 shows results of the cylindrical chamber with and without elbow axial velocity showing the magnitude of the outer-wall velocity increasing. In the cylindrical chamber with an elbow, axial velocity increases at a higher rate, due to being the largest component of the velocity vector, a typical trend of vortex flow cooling.

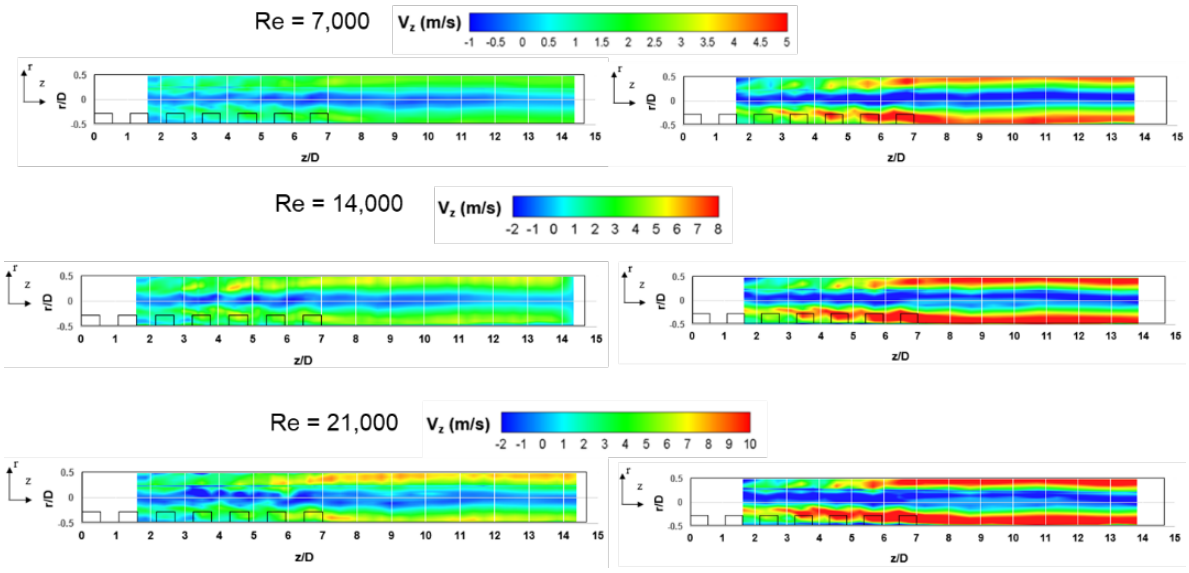


Figure 6-23: Axial velocity distribution of cylindrical chamber with and without elbow.

### 6.3.4. Mass Flow Rate Comparison

The mass flow rate going into the cylindrical chamber matches with mass flow rate going out of the chamber. Figure 6-24 shows the PIV results compared with experimental measurements for both experiment with and without elbow.

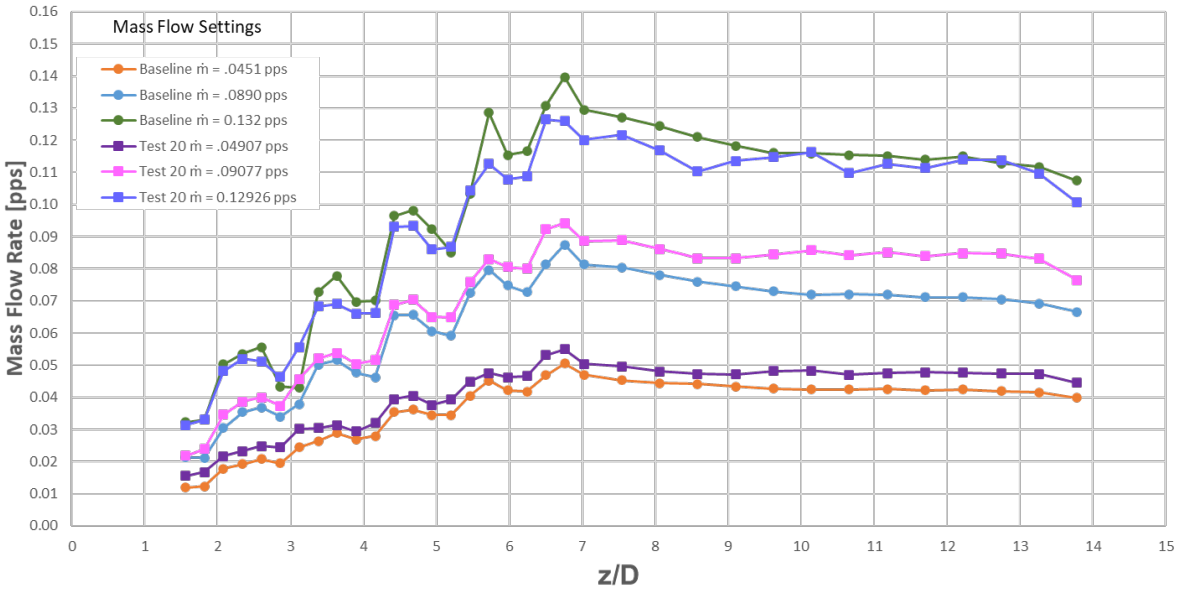


Figure 6-24: Mass flow rate vs. z/D of cylindrical chamber with and without elbow.

### 6.3.5. Normalized-Vz at z/D = 11 Comparison

Figure 6-25 presents the normalized axial velocity against the cylindrical chamber length, both with and without the elbow. The normalized axial velocity at z/D = 11 of the cylindrical chambers with an elbow has higher axial velocity overall than the chamber without elbow, as shown in Figure 6-25. Result demonstrates the pressure decreases downstream on the outer chamber wall, the reverse flow at the centerline is increasingly visible. The reverse vortex flow is present and quite visible in both experiments, with and without the elbow.

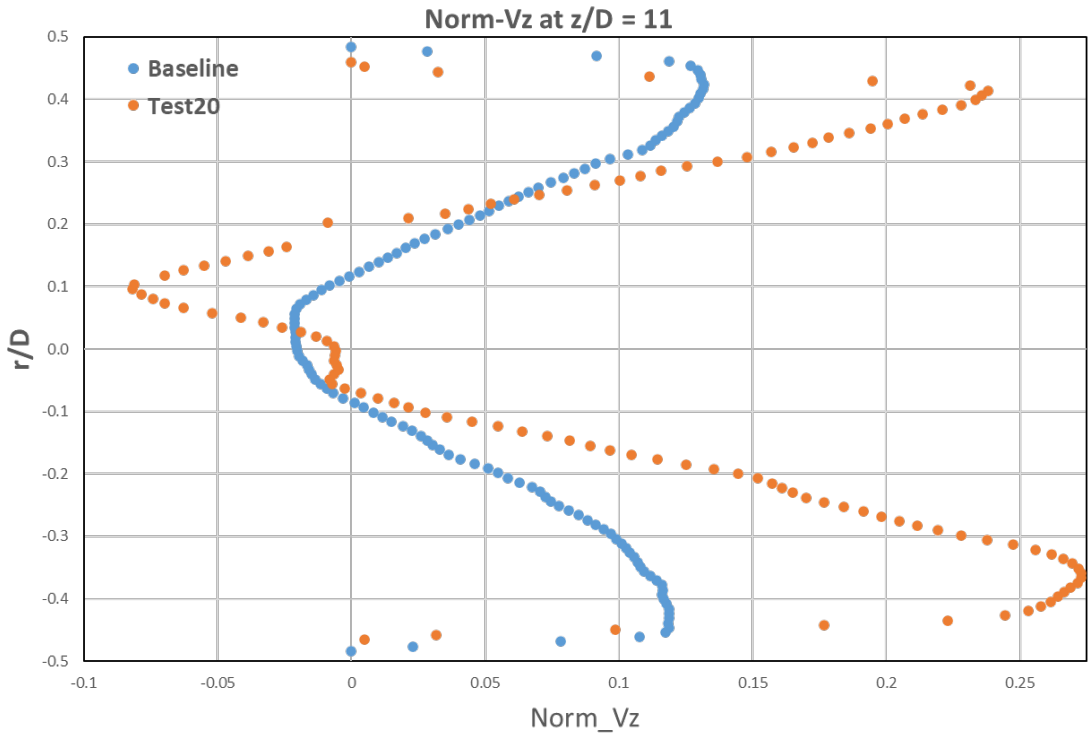


Figure 6-25: Normalized $V_z$ at z/D = 11 of cylindrical chamber with and without elbow.

### 6.3.6. Vorticity Comparison

The vorticity magnitudes are presented in Figure 6-26, the results for cylindrical chamber without elbow generated higher magnitudes. Both experiments generated lower values concentrated near the wall downstream the chamber.

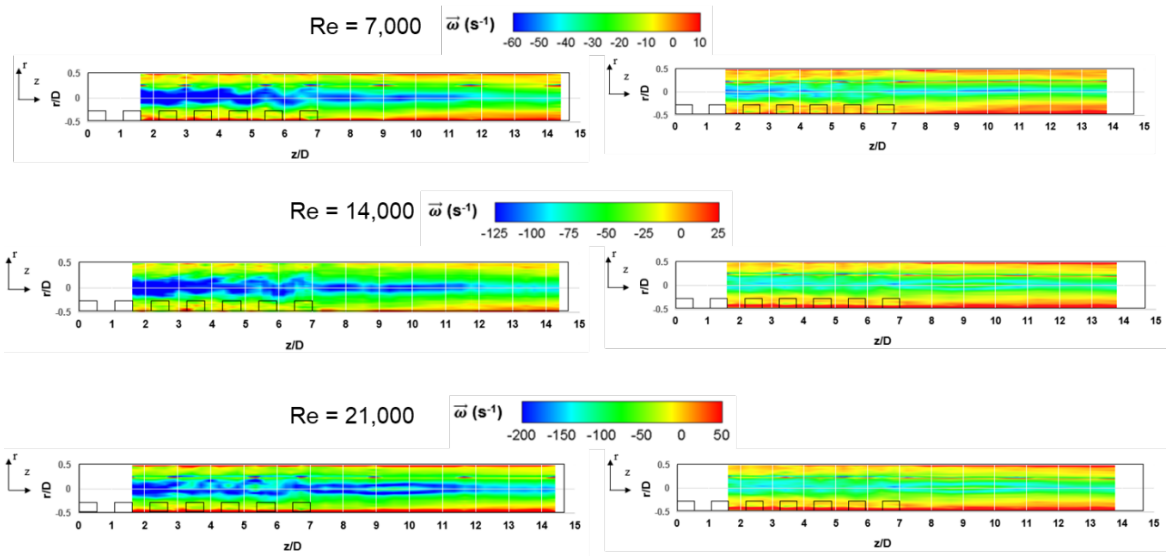


Figure 6-26: Vorticity comparison of cylindrical chamber with and without elbow.

### 6.3.7. Turbulent Intensity Comparison

The turbulent intensity comparison of the cylindrical chamber with and without the elbow provides a more detailed view, as shown in Figure 6-27, where large turbulence occurs in the vortex chamber. The higher the Re number, the higher turbulent intensity at the end of air inlet number 7 where the magnitude of the vortex flow is at its peak.

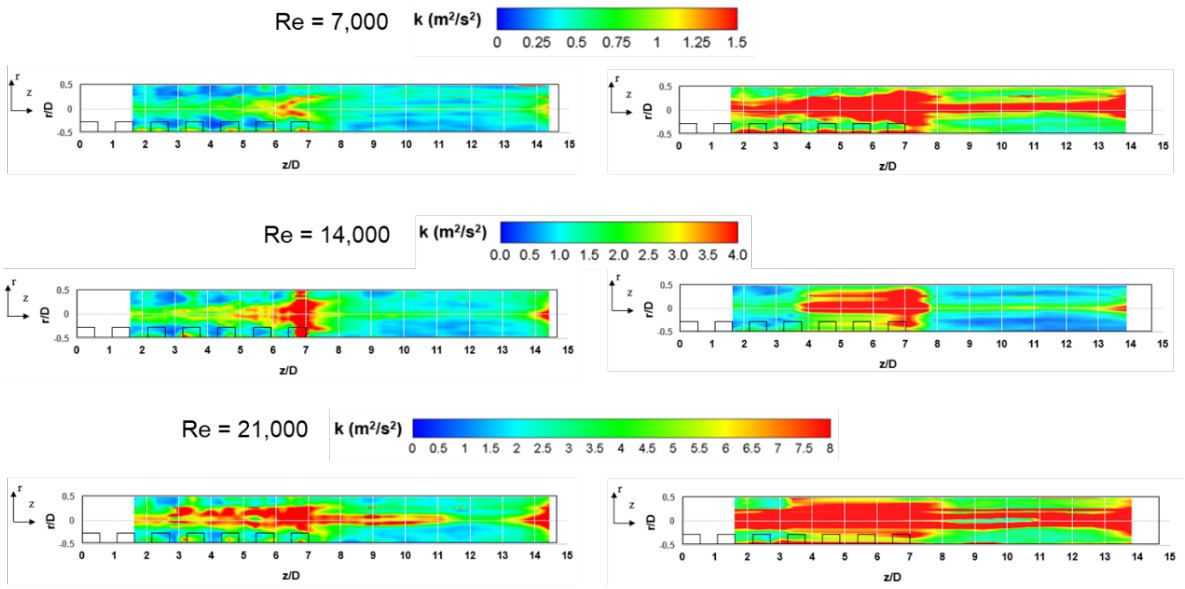


Figure 6-27: Turbulent intensity comparison of cylindrical chamber with and without elbow.

## 6.4. TLC Painted Cylindrical Chamber with and without Elbow Results and Discussions

The second experiment is to gain understanding of the heat transfer benefits of the vortex flow cooling utilizing liquid crystals replicating the internal vortex flow of a turbine blade. One of the objectives of this thesis is to expand the heat transfer studies employing the liquid crystal technique implemented with the practical range of Re numbers of 7,000, 14,000, and 21,000. The goal is to validate a design solution that allows the vortex flow cooling to be more thermally efficient by correlating the advantageous Nu number and $S_N$ distribution.

### 6.4.1. TLC Painted Cylindrical Chamber without Elbow Nusselt Number Calculations

The heat transfer results are presented from a surface Nusselt number distribution. The comparisons of the heat transfer effectiveness from all three Re data were converted to a Nusselt number based on the temperatures. Figure 6-28 depicts that the Nusselt numbers begin to vary near each air inlet in both axial and circumferential directions. The thermal paint test shows that the hot spots are located at the beginning of the chamber and at the end of the chamber length, as shown in Figure 6-29. Correlation of the changing of TLC color versus the Nu peaks is accurate, more air inlets equated higher vortex and Nusselt numbers at each air inlet [83].

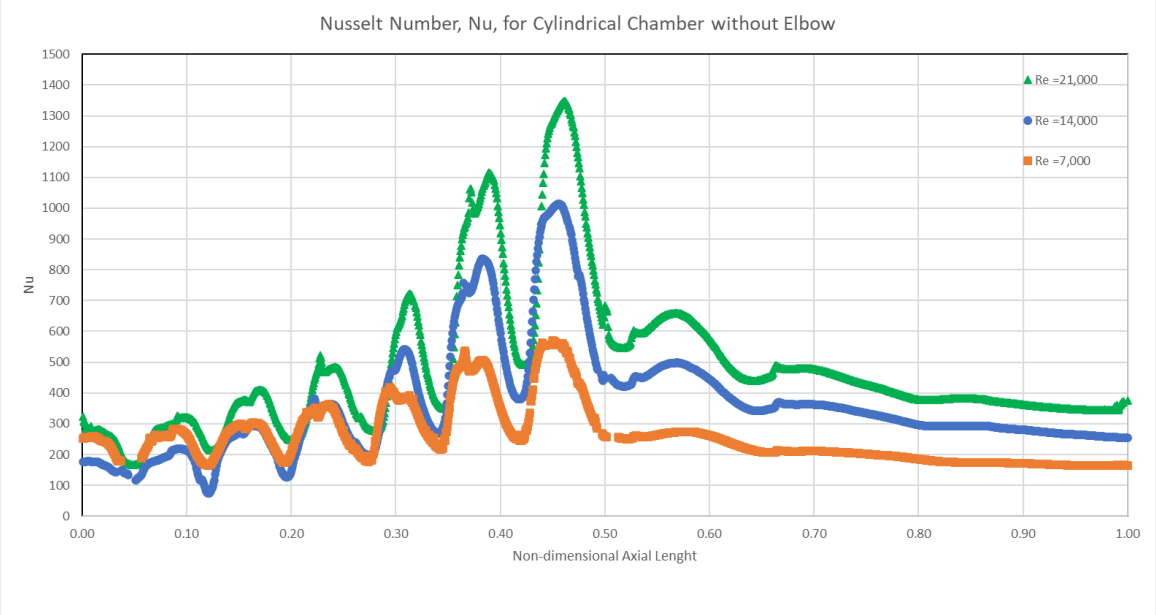


Figure 6-28: Nusselt number magnitudes for PLC painted cylindrical chamber without elbow.

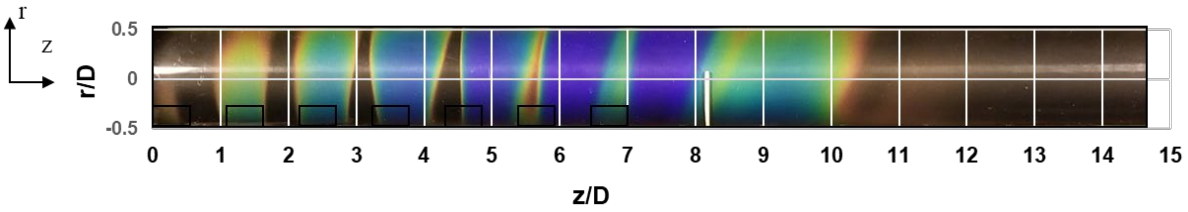


Figure 6-29: Color changing on PLC painted cylindrical chamber without elbow, at Re = 14,000.

### 6.4.2. TLC Painted Cylindrical Chamber with Elbow Nusselt Number Calculations

All three Re numbers (nominal and ±50%) are presented at Re = 7,000, 14,000, and 21,000. The data is taken at two locations using two cameras to measure the entire length of the chamber Nusselt number. The comparisons of the heat transfer effectiveness from all three Re data were converted to a Nusselt number based on the temperatures, as shown in Figure 6-30. As predicted, the Nusselt numbers begin to vary near each air inlet in both axial and circumferential directions. For most of the first half of the cylindrical chamber length the Nu results between the Re = 7,000 and 14,000 produced similar values. Around air inlet six and seven that the magnitude from Re = 14,000 produced higher Nu values. Nu values at Re = 21,000 started below the other two Re numbers, yet it peaks higher at air inlet seven. All three Re show a tempering down of Nu values downstream the chamber.

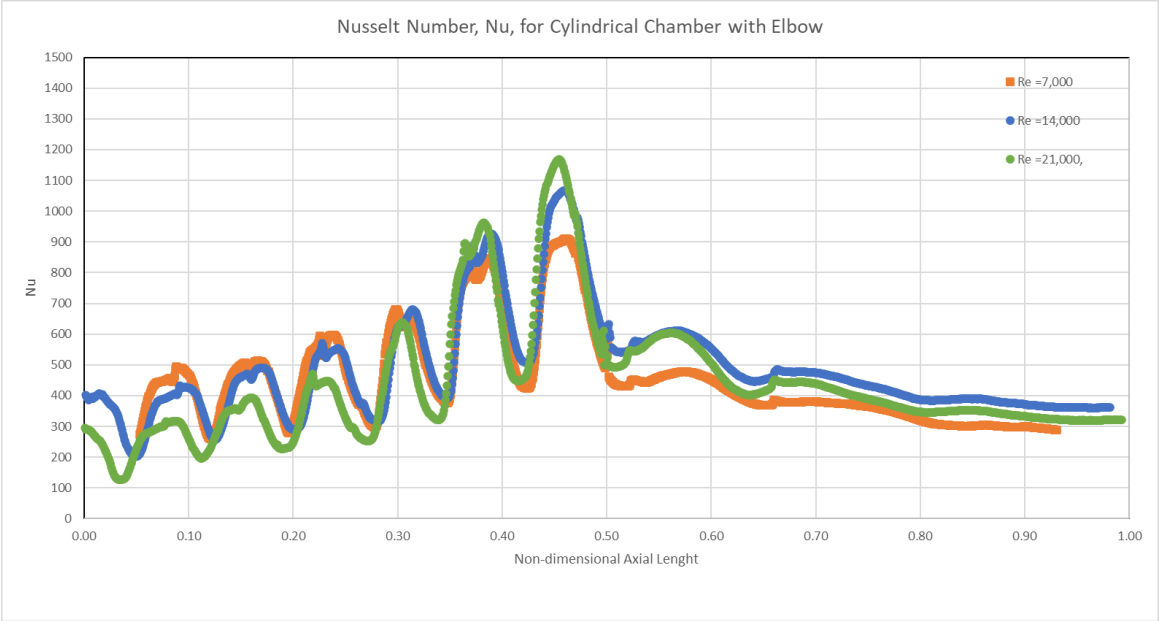


Figure 6-30: Nusselt number magnitudes for PLC painted cylindrical chamber with elbow.

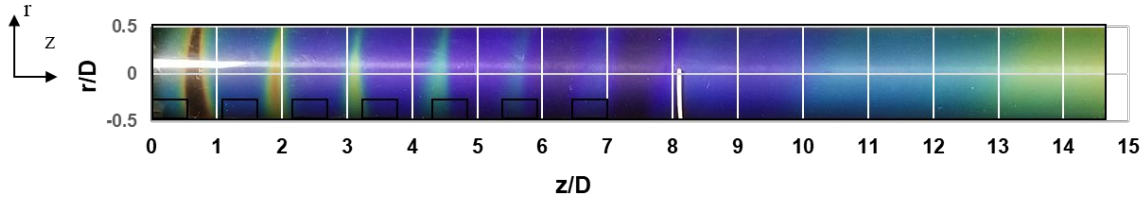


Figure 6-31: Nusselt number magnitudes for PLC painted cylindrical chamber with elbow at Re = 14,000.

As predicted, the Nusselt numbers begin to vary near each air inlet in both axial and circumferential directions. For Re = 7,000 local Nusselt numbers are steadily increasing, from z/D 0.15 to 0.5. As they fluctuate along the entire interior concave surface of the vortex chamber, the Nusselt number average is 260. The focus of this data is to illustrate local Nusselt number flux at only one Re number. It is observed that the largest Nusselt number flux, as well as the maximum values, is around the entire circumference

of the vortex chamber. Another observation is that the Nusselt number varies in the axial and circumferential directions in all seven air inlets at different time rates. Figure 6-31 shows the distribution of Nusselt number at Re =14,000 with an average of 367 and occurs at a higher rate downstream the chamber when compared to the location upstream. Re=21,000 heat transfer distribution was slower than any other Re number in this experiment, as the flow rate was too high for the mesh heater, taking longer than predicted. The Nu results at Re = 21,000 have an average of 559, which is a much higher peak at the middle of the chamber.

### 6.4.3. Nusselt Number Comparison

Complex Nu variations are evident in Figure 6-32, specially just downstream of the air inlets located at z = 0.00 – 0.50. The Nu results are nicely distributed along the chamber's length, these distributions paint a good picture of how the heat transfer is behaving. Not only the Nu highest values in the middle region of the chamber length due to arrays of Görtler vortex pairs, but gradients of the Nu numbers are evident in both experiments chamber with and without elbow. The Nu values from the cylindrical chamber without the elbow are the highest. Nu number peaks are above each air inlet, which is an expected trend.

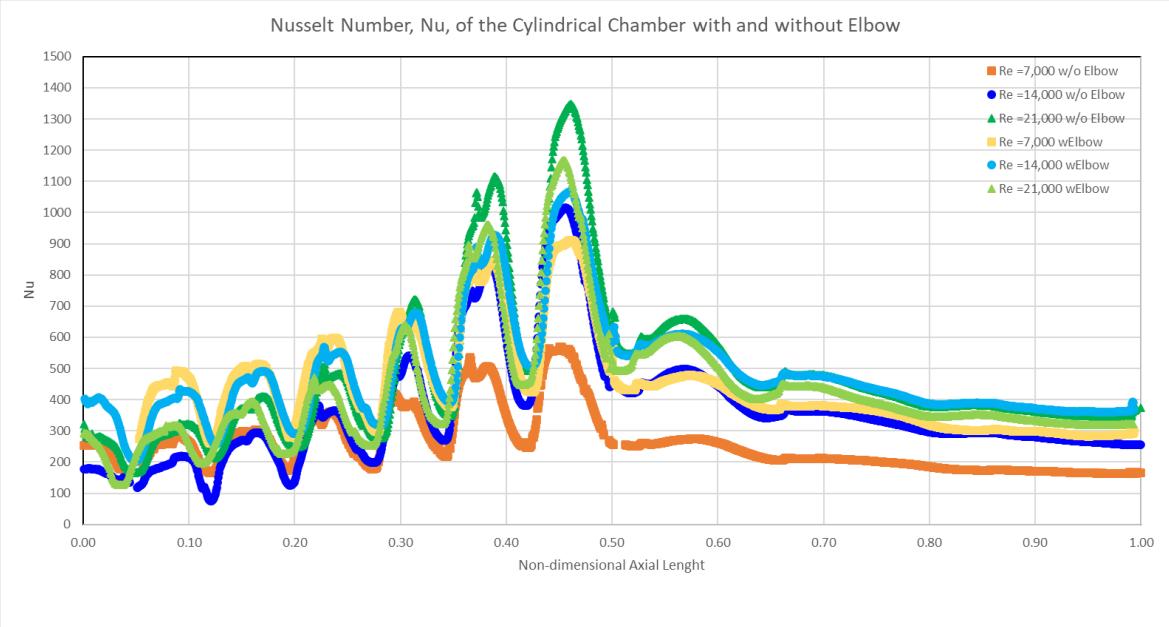


Figure 6-32: Nusselt number magnitudes for PLC painted cylindrical chamber with and without elbow.

Figure 6-32 shows the lowest Nu values came from Re = 7,000 without elbow, at z = 0 – 0.35 and max and min Nu numbers of 163 and 569, respectively. Another observation, Nu values stayed low with an insignificant peak. The highest Nu numbers come from the cylindrical chamber without an elbow at Re = 21,000, with a minimum Nu number of 167 and a maximum Nu value of 1348. The Nu numbers are ideal, and they are maintained throughout the entire chamber length, but in real life application this design is not feasible.

Looking only at the cylindrical chamber with an elbow, with Re = 7,000, the maximum Nu value is 911 and the minimum is 260. The distribution is gradually increasing until it reaches the highest peak at the middle of the chamber length. At Re = 21,000, the maximum Nu value is 1168 and a minimum of 127, which makes it less ideal due to the wider range and the lower value of the average Nu number than the nominal.

Figure 6-32 presents Nu magnitudes at nominal Re = 14,000, the minimum Nu number is 202 and the maximum is 1067, with a steady increment for the first half of the chamber length. The importance of this Nu number variation trend is that it maintains the Nu number distribution for the ¾ of the chamber length. Also, at the downstream of the chamber it has the highest Nu value than any other configuration and Re number, therefore making this experimental setup the best of all possible scenarios.

Overall variations are entirely consistent with the circumferential vorticity contours shown in previous plots. The high Nu number regions are due to the shear layer near the edge of the air inlets. This shear layer contains a shear layer vortex like the ones seen in many of the visualization images presented in this thesis. The results in all the Nu plots illustrate the excellent and spatial resolution obtained with the TLC methodology employed for the study.

## 6.5. Critical Swirl Number Findings of Cylindrical Chamber without Elbow

The presence of a reverse flow was surprising, yet satisfying, proving that new technology allows us to discover additional details of the vortex flow cooling behavior. This research study showed that at all Re numbers, the unintentional reverse flow manifested, and subsequently, more investigation was conducted to find the critical Swirl Number ($S_{N\_critical}$), as seen in Figure 6-33.

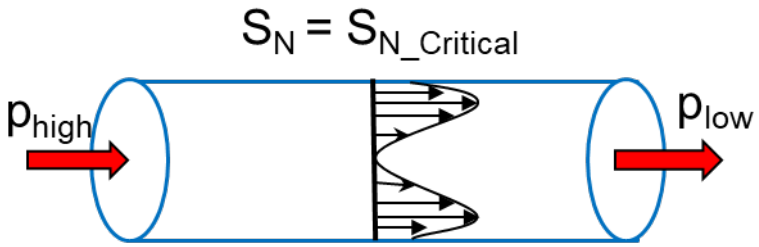


Figure 6-33: Critical Swirl Number schematic.

Finding the critical $S_N$ was not an easy task; the first assessment is that the Re number is directly proportional to the mass flow rate, as described in Eq. (*4-1*). The experiment was run using 3-D stereo-PIV at several descending Re numbers in decrement of 500, until a low Re of was found that did not produce a reverse flow. Since the lowest Re number of the original research was 7,000, the no reverse flow investigation started at Re = 6,500, 6,000, 5,500, 5,000, etc. The Re number with no reverse vortex flow is found to be 840, which calculated a total mass flow rate of 0.005 pps. Not having a reverse flow can only be found with a Re number that is 94% lower than the recommended nominal Re number of 14,000. In real life function, the low Re number of 840 with a low mass flow rate of 0.005 pps is not sufficient to cool down the gas turbine blade fast enough. Therefore, it is not recommended as one of the solutions for this type of application.

# CHAPTER 7 CONCLUSIONS

Velocity flow field and $S_N$ measurements were collected using 3-D Stereo-PIV technique from a cylindrical vortex chamber, which models an internal cooling passage located near the leading edge of a gas turbine blade and presented for Re from 7,000 to 21,000. Such results illustrate the outstanding accuracy and 3-D resolution obtained with the Stereo-PIV imaging techniques employed here. The 3-D Stereo-PIV measurements, in conjunction with MATLAB averaged velocity fields calculations, show important results at three different Reynolds numbers, non-dimensional axial location z/D, and circumferential location. These combinations and practices revealed distinct advantages over other cooling methods and demonstrated the increased vortex flow cooling effectiveness using only seven air inlets.

The circumferential and axial velocity distributions, measured experimentally with Stereo-PIV and solved with MATLAB assistance, were plotted using Techplot 360. The experiment shows that the circumferential velocity decreases downstream and that the maximum circumferential velocity shifts towards the center of the chamber with downstream distance. The axial velocity is higher towards the outer wall region and increases within the chamber length, reaching a maximum in the second half of the chamber. Results also show that the vorticity increases closer to the wall, and as well, that there are slight increases in magnitude downstream the chamber. Also, the

turbulence kinetic energy distribution of the axial rms is similar to the tangential rms; however, the axial rms is generally lower throughout the chamber length.

In conclusion, the magnitude of the outer-wall velocity increases due to the enlargement of the vortex flow core, and the $S_N$ is higher than expected. These two observations are very important behaviors observed from the Reynolds numbers from 7,000 to 21,000 based on the characteristics of incorporating seven inlets. The results established here demonstrate a better understanding of this complex flow phenomena. The $S_N$ increases are visible at each air inlet, and later, $S_N$ decreases as predicted, since there are no more air inlets available. Research shows that $S_N$ is largely dependent on the tangential injection. Such variation is entirely consistent with surveys of time-averaged circumferential velocity, axial velocity, circumferential vorticity, and turbulent kinetic energy. Additionally, $S_N$ increases influenced by the shear layer near the edge of the air inlet. For future research, optimizing the cylindrical chamber is recommended to reduce to a six air-inlet configuration, since $S_N$ values show that the seventh air inlet does not appear to have any effect. Consequently, applying this concept will be more favorable for manufacturing practices because it reduces the amount of time spend in complicated precision casting.

The experimental study produced valuable flow field and Nusselt number distributions, and furthermore, it confirms that the selected vortex flow cooling design in a cylindrical chamber with an elbow provides higher $S_N$ and Nu numbers at nominal Re number. This test article design utilizes seven tangential air inlets on the pressure side of the gas turbine blade, which is the highest heat transfer surface of a blade. The primary research objective was to study gas turbine blade leading-edge using CFD, 3-D Stereo-

PIV, and TLC techniques, and all techniques were performed. The heat transfer coefficient distribution on the test surface was obtained by using TLC. The heat transfer measurements predicted at the beginning of the experiment was 700, experiment demonstrated on a seven-air inlet model a higher internal heat transfer coefficient than predicted in relation to the leading-edge passage. The heat transfer behaves in a uniform distribution, resulting in this seven-air inlet design being more advantageous than a conventional two-air inlet channel.

The versatility of the vortex cooling design to redistribute a different path of heat load profile without major casting changes was demonstrated by increasing the air inlets from two to seven. Additionally, the span of the outer-wall velocity flow fields increases, due to the enlargement of the vortex flow core, and as well, the swirl number, $S_N$, is higher than expected. The TLC heat transfer test results exemplify how the Nu were measured favorably at the middle length of the chamber and values decline downstream. The upstream temperatures of the chamber were cooler up to the mid-length and became almost identical to those of the downstream half of span. The mid-chamber Nu span from 600 to 1200 is the most important variation and attributed to being after all seven-air inlet. As flow moves away from these seven air inlets, Nu numbers become approximately uniform. These two techniques are very important behaviors for this range of Reynolds numbers because they establish a better understanding of complicated flow occurrences.

The actual heat load in the entire leading-edge of a gas turbine blade is extremely difficult to predict due to the complexity of the flow, which is highly three-dimensional. Therefore, tools such as CFD, TLC and 3-D Stereo-PIV are necessary to provide more detailed and accurate results. The blade internal vortex cooling flow is more versatile and

possesses a critical advantage that needs more study so that the design can be optimized to meet future gas turbine TRIT requirements.

The primary objective of this research has been met by performing the internal vortex flow cooling study that gas turbine blades categorically need to keep pace with the heat augmentation demands to increase pressure ratio.

The following conclusions can be drawn from analysis of the CFD:

- The vortex tube, also known as the Ranque-Hilsch vortex tube, is found in this design, even though it is unintentional consequence, the effect that separates a compressed air into hot and cold streams with temperature difference reaching over 250 °C.
- The detailed flow behavior inside a Ranque-Hilsch vortex tube and flow reversal in the cylindrical chamber share similarities.
- Based on this study there was an impressive presence of reverse axial flow at the core as illustrated in the experimental results.
- CFD simulation correlated the experiment results and validated the reverse flow with similar mass flow rate and pressure gradients of 0.0535 kg/s and 979 Pa, respectively.
- The CFD recreated the reverse flow at Re = 14,000.
- The CFD found that higher pressure input can contribute to lowering the temperature at the exit from the chamber, favoring the cooling process.

The following conclusions can be drawn from the cylindrical chamber without an elbow at nominal Re = 14,000 using 3-D stereo-PIV for velocity flow field and TLC for Nu analysis.

- A reverse vortex flow is noticed at all three Re numbers. At Re = 14,000 reverse vortex flow covers about one-third of the cylindrical chamber diameter.
- The critical $S_N$ is the one that gives positive augmentation of blade internal heat transfer with reverse vortex flow relative to a simple channel flow.
- The circumferential velocity is clearly the largest component of the velocity vector, typical of vortex flow cooling designs.
- The magnitude of the circumferential velocity towards the outer-wall velocity increases due to the enlargement of the reverse vortex flow core.
- The maximum axial velocity magnitudes are lower than those in the experiment with the elbow.
- The axial velocity decreases upstream on the outer cylindrical chamber wall and increases after the last air inlet.
- The axial velocity peaks as it gets closer to the wall.
- The RMS provides a more detailed view where large turbulence occurs at the middle section of the chamber length.
- Vorticity is higher and pronounced at the cylindrical chamber wall and shows the low value at the core of the vortex flow.
- The Nu number magnitudes are at the lower end of the spectrum when compared to the other Re number results. It produced a minimum of 74 and a maximum of 1015.

The following conclusions can be drawn from a cylindrical chamber with an elbow at nominal Re = 14,000 using 3-D stereo-PIV for velocity flow field and TLC for Nu analysis.

- Reverse vortex flow covers about one-third of the cylindrical chamber diameter and there is no reason to believe reverse flow can be removed for this application.
- The circumferential velocity is undoubtedly the component that occupies the velocity vector, typical of vortex flow cooling designs. Circumferential velocity decreases downstream.
- The magnitude of the circumferential velocity towards the outer-wall velocity increases due to the enlargement of the reverse vortex flow core.
- The maximum axial velocity magnitudes are high and increases downstream allowing the vortex flow to fully form from air inlet number 3.
- The axial velocity is shown to move towards the outer cylindrical chamber wall and increases after the last air inlet.
- The axial velocity peak is significantly higher as it gets closer to the wall.
- The RMS provides a clear view where large turbulence occurs at the middle section of the chamber length, it dissipates after air inlet number 7 and short appears at the end of the cylindrical chamber.
- Vorticity is a lot higher and pronounced at the cylindrical chamber wall for the entire duration of the chamber length.
- The Nu number magnitudes are the third highest from all the Re numbers. It produced a minimum of 202 and a maximum of 1067.

Overall results from PIV and liquid crystals worthy to mentioned are:

- PIV shows that there is a reverse flow at all three Re numbers, 7,000, 14,000, and 21,000.
- PIV indicated that the substantial $S_N$ is at Re = 21,000 with elbow attached because it produces a higher $S_N$ and Nu, regrettably it carries a crucial disadvantage because it requires a higher mass flow rate.
- PIV also showed that the $S_N$ distribution at Re = 14,000 behaves similarly to the Re = 21,000, and therefore Re = 14,000 is preferred since it will use less mass flow rate to cool down the blade for the same result. Regarding design efficiency for $S_N$ at Re = 14,000, this design is the most efficient.
- PIV results showed the circumferential velocity at Re = 14,000 is sufficient.
- PIV showed that the Axial velocity at Re = 14,000 was the ideal for this application since the high Axial velocity peaks start forming after air inlet 5 and maintain the peaks after air inlet 7 throughout the chamber's length. The peaks travel closer to the wall as the air travels downstream.
- PIV also shows vorticity.
- PIV presents turbulent intensity.
- Liquid crystal results showed Nu peak is the highest at Re = 21,000, yet the second highest Nu peaks came from Re = 14,000 with elbow attached, making the Re = 14,000 option the optimum Nu distribution.

The most advantageous test article that produced the optimum results is the design of the cylindrical chamber with seven air inlets with elbow attached at Re number

of 14,000 and a mass flow rate of 0.04179 kg/sec. Resulting the second highest $S_N$ of 3 at air inlet number 3 and a low $S_N$ of 1.5 at air inlet seven. Circumferential velocity reaching 15 m/s starting from air inlet 2. Axial velocity peak at 8 m/s starting at air inlet 3. Turbulent intensity is present one third of the chamber length and highest value is 4 $m^2/s^2$ from air inlet 4 through 7. Vorticity has an even distribution from air inlet two all the way down to the end of the chamber length with a low vorticity value of -125 $s^{-1}$ and a high value of 25 $s^{-1}$. The most advantageous Nu value came from Re = 14,000.

# REFERENCES


[1] Moon, H.K., O'Connell, T., and Glezer, B., "Heat Transfer Enhancement in a Circular Channel Using Lenghtwise Continuous Tangential Injection," *Heat Transfer,* vol. 6, pp. 559-564, 23-28 August 1998.

[2] Moon, H.K., O'Connell, T., and Glezer, B., "Channel Height Effect on Heat Transfer and Friction in a Dimpled Passage," *Journal of Engineering for Gas Turbines and Power, ASME,* vol. 122, pp. 307-313, 2000.

[3] Kosieniak, E., Biesiada, K., Kaczorowski, J., and Innocenti, M., "Corrosion Failures in Gas Turbines Hot Components," *Journal of Failure Analysis and Prevention,* vol. 12, pp. 330-337, 2012.

[4] Ligrani, P., "Heat Transfer Augmentation Technologies for Internal Cooling of Turbine Components of Gas Turbine Engines," *International Journal of Rotating Machinery,* vol. 1, pp. 1-33, 2013.

[5] Ligrani, P., Goodro, M., Fox, M., and Moon, H.-K., "Full-Coverage Film Cooling: Film Effectiveness and Heat Transfer Coefficients for Dense Hole Arrays at Different Hole Angles, Contraction Ratios, and Blowing Ratios," *Journal of Heat Transfer, ASME,* pp. 031707-1 - 031707-14, 2013.

[6] Ligrani, P., Goodro, M., Fox, M.D., and Moon, H.-K, "Full-Coverage Film Cooling: Heat Transfer Coefficients and Film Effectiveness for a Sparse Hole Array at Different Blowing Ratios and Contraction Ratios," *Journal of Heat Transfer, ASME,* vol. 137, pp. 032201-1 - 032201-12, 2015.

[7] Ligrani, P.M., Hedlund, C.R., Babinchak, B.T., Thambu, R., Moon, H.-K., and Glezer, B., "Flow Phenomena in Swirl Chambers," *Experiments in Fluids,* vol. 24, pp. 254-264, 1998.

[8] Kurz, R., "Gas Turbines Performance," *Proceedings of the Thirty-Fourth Turbomachinery Symposium,* pp. 131-145, 2005.

[9] Kumar, S. and Singh, O., "Thermodynamic Evaluation of Different Gas Turbine Blade Cooling Techniques," *Thermal Issues in Emerging Technologies,* pp. 237-244, 2008.

[10] Kusterer, K., Lin, G., Bohn, D., Sugimoto, T., Tanaka, R., and Kazari, M., "Leading Edge Cooling of a Gas Turbine Blade with Double Swirl Chambers," *Proceedings of ASME Turbo Expo 2014: Turbine Technical Conference and Exposition,* pp. 1-11, 2014.

[11] Ahn, J., Schobeiri, M.T., han, J.-C., and Moon, H.-K., "Effect of Rotation on Leading Edge Region Film Cooling of a Gas Turbine Blade with Three Rows of Film Cooling Holes," *International Journal of Heat and Mass Transfer,* vol. 50, pp. 15-25, 2007.

[12] Chung, H., Park, J.S., Sohn, H.-S., Rhee, D.-H., and Cho, H.H., "Trailing Edge Cooling of a Gas Turbine Blade with Perforated Blockages with Inclined Holes," *International Journal of Heat and Mass Transfer,* vol. 73, pp. 9-20, 2014.

[13] Gao, Z., Narzary, D.P., and Han, J.-H., "Film Cooling on a Gas Turbine Blade Pressure Side or Suction Side with Axial Shaped Holes," *International Journal of Heat and Mass Transfer,* vol. 51, pp. 2139-2152, 2008.

[14] Garg, V. and Gaugler, R., "Effect of Coolant Temperature and Mass Flow on Film Cooling of Turbine Blades," *International Journal of Heat and Mass Transfer,* vol. 40, no. 2, pp. 435-445, 1997.

[15] Glezer, B., Moon, H.K., and O'Connell, T., "A Novel Technique For The Internal Blade Cooling," *The American Society of Mechanical Engineers,* pp. 1-10, 10-13 June 1996.

[16] Glezer, B., Moon, H.K., Kerrebrock, J., Bons, J., and Guenette, G., "Heat Transfer in a Rotating Radial Channel with Swirling Internal Flow," *ASME,* pp. 1-7, 1998.

[17] Han, J.-C., and Chen, H.-C., "Turbine Blade Internal Cooling Passages with Rib Turbulators," *Journal of Propulsion and Power,* vol. 22, no. 2, pp. 226-248, 2006.

[18] Ligrani, P.M., Choi, S., Schallert, A.R., and Skogerboe, P., "Effects of Dean Vortex Pairs on Surface Heat Transfer in Curved Channel Flow," *Internationl Journal of Heat and Mass Transfer,* vol. 39, no. 1, pp. 27-37, 1996.

[19] Ligrani, P.M., Mahmood, G.I., Harrison, J.L., Clayton, C.M., and Nelson, D.L., "Flow Structure and Local Nusselt Number Variations in a Channel with Dimples and Protrusions on Opposite Walls," *International Journal of Heat and Mass Transfer,* vol. 44, pp. 4413-4425, 2001.

[20] Ligrani, P.M., Oliveira, M.M., and Blaskovich, T., "Comparison of Heat Transfer Augmentation Techniques," *AIAA JOURNAL,* vol. 41, no. 3, pp. 1-26, March 2003.

[21] Li, S.-J., Lee, J., Han, J.-C., Zhang, L., and Moon, H.-K., "Turbine Platform Cooling and Blade Suction Surface Phantom Cooling From Simulated Swirl Purge Flow," *Journal of Turbomachinery,* vol. 138, pp. 1-11, 2016.

[22] Kreith, F. and Margolis, D., "Heat Transfer and Friction in Turbulent Vortex Flow," *Applied Science,* vol. 8, no. A, pp. 1-17.

[23] Salem, A.R., Nourin, F.N., Abousabae, M., and Amano, R.S., "Experimental and Numerical Study of Jet Impingement Cooling for Improved Gas Turbine Blade Internal Cooling With In-Line and Staggered Nozzle Arrays," *Journal of Energy Resources Technology,* vol. 143, no. 1, p. 012103, 29 July 2020.

[24] Hedlund, C.R. and Ligrani, P.M., "Local Swirl Chamber Heat Transfer and Flow Structure at Different Reynolds Numbers," *Journal of Turbomachinary,* vol. 122, pp. 374-385, April 2000.

[25] Nasir, H., "Turbine Blade Tip Coolong and Heat," *Louisiana State University,* 2004.

[26] Morris, W.D. and Chang, S.W., "An Experimental Study of Heat Transfer in a Simulated Turbine Blade Cooling Passage," *International Journal of Heat and Mass Transfer,* vol. 40, no. 15, pp. 3703-3716, 1997.

[27] Zhang, J., Dong, L. and Zhou, L., "Simulation of Swirling Turbulent Flows and Heat Transfer in an Annular Duct," *Numerical Heat Transfer,* vol. 44, no. A, pp. 591-609, 2003.

[28] Hedlund, C.R. and Ligrani, P.M., "Heat Transfer in Curved and Straight Channels with Transitional Flow," *International Journal of Heat and Mass Transfer,* vol. 41, no. 3, pp. 563-573, 1998.

[29] Thambu, R., Babinchak, B.T., Ligrani, P.M., Hedlund, C.R., Moon, H.K., and Glezer, B., "Flow in a Simple Swirl Chamber With and Without Controlled Inlet Forcing," *Experiments in Fluids,* vol. 26, pp. 347-357, 1999.

[30] Chang, F. and Dhir, V.K., "Turbulent Flow Field in Tangentially Injected Swirl Flows in Tubes," *Heat and Fluid Flow,* vol. 15, no. 5, pp. 346-356, 22 May 1994.

[31] Haiyong, L., Hongfu, Q., Songling, L., and Cunliang, L., "Flow Field Investigation in a Trapezoidal Duct with Swirl Flow Induced by Impingement Jets," *Chinese Journal of Aeronautics,* vol. 24, pp. 8-17, 2011.

[32] Han, J.-C. and Wright, L.M., "Enhanced Internal Cooling of Turbine Blades and Vanes," *Turbine Heat Transfer Laboratory Department of Mechanical Engineering,* 2003.

[33] Kumar, N.A. and Kale, S.R., "Numerical Simulation of Steady State Heat Transfer in a Ceramic-Coated Gas Turbine Blade," *International Journal of Heat and Mass Transfer,* vol. 45, pp. 4831-4845, 2002.

[34] Yang, L., Ligrani, P.M., Ren, J., and Jiang, H., "Unsteady Structure and Development of a Row of Impingement Jets, Including Shear Layer and Vortex Development, Part 1: Turbulent Jets," *Proceedings of ASME Turbo Expo 2015: Turbine Technical Conference and Exposition,* pp. 1-14, 2015.

[35] Yang, L., Ren, J., Jiang, H., and Ligrani, P.M.,, "Unsteady Structure and Development of a Row of Impingement Jets, Including Shear Layer and Vortex Development, Part 1: Laminar Jets," *Proceedings of ASME Turbo Expo 2015: Turbine Technical Conference and Exposition,* pp. 1-11, 2015.

[36] Zhu, J. Wuhong, and Liu, X., "Numerical study of Fluid Flow and Heat Transfer Characteristics in the Leading Edge of Turbine Blades," *International Conference on Energy and Enviroment Technology,* pp. 431-434, 2009.

[37] Yang, L., Ligrani, P., Ren, J., and Jiang, H., "Unsteady Structure and Development of a Row of Impingement Jets, Including Kelvin–Helmholtz Vortex Development," *Journal of Fluids Engineering, ASME,* vol. 137, pp. 051201-1 - 051201-12, 2015.

[38] Hedlund, C.R., Ligrani, P.M., Glezer, B., and Moon, H.-K., "Heat Transfer in a Swirl Chamber at Different Temperature," *International Journal of Heat and Mass Transfer,* vol. 42, pp. 1081-1091, 1999.

[39] Hedlund, C.R. Ligrani, P.M. Moon, H.-K. and Glezer, B., "Heat Transfer and Flow Phenomena in a Swirl Chamber Simulating Turbine Blade Internal Cooling," *ASME,* vol. 121, pp. 804-813, October 1999.

[40] Lin, G., Kusterer, L., Bohn, D., Sugimoto, T., Tanaka, R., and Kazari, M., "Investigation on Heat Transfer Enhancement and Pressure Loss of Double Swirl Chambers Cooling," *Propulsion and Power Research,* vol. 2, no. 3, pp. 177-187, 2013.

[41] Sheen, H.J., Chen, W.J., Jeng, S.Y. and Huang, T.L., "Correlation of Swirl Number for a Radial-Type Swirl Generator," *Experimental Thermal and Fluid Science,* vol. 12, pp. 444-451, 1996.

[42] Takeishi, K., Komiyama, M., Oda, Y., and Egawa, Y., "Aerothermal Investigations on Mixing Flow Field of Film Cooling With Swirling Coolant Flow," *Journal of Turbomachinery, ASME,* vol. 136, pp. 1-9, 2014.

[43] Bakirci, K. and Bilen, K., "Visualization of Heat Transfer for Impinging Swirl Flow," *Experimental Thermal and Fluid Science,* vol. 32, pp. 182-191, 2007.

[44] Camci, C. and Glezer, B., "Color Response Modification of Encapsulated Liquid Crystals Used in Rotating Disk Heat Transfer Studies," *ASME,* pp. 1-10, 1995.

[45] Camci, C., Glezer, G., Owen, J.M., Pilbrow, R.G., and Syson, B.J., "Application of Thermochromic Liquid Crystal to Rotating Surfaces," *International Gas Turbine and Aeroengine Congress & Exhibition,* pp. 1-7, 1996.

[46] Camci, C., and Glezer, B., "Liquid Crystal Thermography on the Fluid Solid Interface of Rotating Systems," *ASME,* vol. 119, pp. 20-29, 1997.

[47] Ren, Z., Buzzard, W., and Ligrani, P.M., "Influences of Traget Surface Cylindrical Roughness on Impingement Jet Array Heat Transfer: Effects of Roughness Height Roughness Shape, and Reynolds Number," *Proceedings of the ASME 2016 International Mechanical Engineering Congress and Exposition,* pp. 1-10, 2016.

[48] Zhang, Y., Yuan, X., and Ligrani, P., "Film Cooling Effectiveness Distribution on First-Stage Vane Endwall with and without Leading-Edge Fillets," *International Journal of Heat and Mass Transfer,* vol. 66, pp. 642-654, 2013.

[49] Zhang, L., Yin, J., Liu, K., and Moon, H.-K, "Effect of Hole DIamater on Nozzle Endwall Film Cooling and Associated Phantom Cooling," *Proceedings of ASME Turbo Expo 2015: Turbine Technical Conference and Exposition,* pp. 1-12, 2015.

[50] Zhang, G., Liu, J., Sundén, B., and Xie, G., "Improvements of the Adiabatic Film Cooling by Using Two-Row Holes of Different Geometries and Arrangements," *Journal of Energy reseouces Technology,* vol. 142, no. 12, p. 122101, 12 June 2020.

[51] Yang, C.S., Kung, T.L., and Gau, C., "Heat Transfer Process Under a Film-Cooled Surface with Presence of Weak Swirling Flow in the Mainstream," *Experimental Thermal and Fluid Science,* vol. 32, pp. 632-640, 2007.

[52] Xie, G. and Suden, B., "Numerical Predictions of Augmented Heat Transfer of an Internal Blade Tip-Wall by Hemispherical Dimples," *International Journal of Heat and Mass Transfer,* vol. 53, pp. 5639-5650, 2010.

[53] Xie, G., Liu, J., Ligrani, O.M., and Suden, B., "Flow Structure and Heat Transfer in a Square Passage with Offset Mid-Truncated Ribs," *International Journal of Heat and Mass Transfer,* vol. 71, pp. 44-56, 2014.

[54] Xie, Y., Shen, Z., Zhang, D., and Ligrani, P., "Numerical Analysis of Flow Structure and Heat Transfer Characteristics in Dimpled Channels With Secondary Protrusions," *Journal of Heat Transfer, ASME,* vol. 138, pp. 1-6, 2016.

[55] Moritz, N., Kusterer, K., Bohn, D., Sugimoto, T., Tanaka, R., and Taniguchi, T., "Conjugate Calculation of a Film-Cooled Blade for Improvement of the Leading Edge Cooling Configuration," *Propulsion and Power Research,* vol. 2, no. 1, pp. 1-9, 2013.

[56] Mahmoon, G.I., Hill, M.L., Nelson, D.L., Ligrani, P.M., Moon, H.-K., and Glezer, B., "Local Heat Transfer and Flow Structure on and Above a Dimpled Surface in a Channel," *Journal of Turbomachinery, ASME,* vol. 123, pp. 115-123, 2001.

[57] Akiyama, O. and Kato, C., "Numerical Investigations of Unsteady Flows and Particle Behavior in a Cyclone Separator," *Journal of Fluids Engineering, ASME,* vol. 139, pp. 1-11, 2017.

[58] McLean, C., Camci, C., and Glezer, B., "Mainstream Aerodynamic Effects Due to Wheelspace Coolant Injection in a High-Pressure Turbine Stage: Part I—Aerodynamic Measurements in the Stationary Frame," *Journal of Turbomachinery, ASME,* vol. 123, pp. 687-696, 2001.

[59] McLean, C., Camci, C., and Glezer, B., "Mainstream Aerodynamic Effects Due to Wheelspace Coolant Injection in a High-Pressure Turbine Stage: Part II—Aerodynamic Measurements in the Rotational Frame," *Journal of Turbomachinery, ASME,* vol. 123, pp. 697-703, 2001.

[60] Yang, Z. and Hu, H., "An Experimental Investigation on the Trailing Edge Cooling of Turbine Blades," *Propulsion and Power Research,* vol. 1, no. 1, pp. 36-47, 2012.

[61] Wassermann, F., Grundmann, S., Kloss, M., and Schiffer, H.-P., "Swilr Flow Investigations on the Enhancement of Heat Transfer Processes in Cyclone Cooling Ducts," *Proceedings of the ASME 2012 Turbine Technical Conferences & Expositions,* pp. 1-15, 2012.

[62] Tieyu, G. and Jianying, G., "Heat Transfer Research on a Certain Gas Turbine Blade," *Crown,* vol. 11, 2011.

[63] Wang, X.W., Zhou, Y., and Wong, W.O., "Turbulent Flow Structure and Swirl Number Effect in a Cyclone," *Journal of Fluids Engineering, ASME,* vol. 133, pp. 1-10, 2011.

[64] Wu, H.-W., Zirakzadeh, H., Han, J.-C., Zhang, L., and Moon, H.-K., "Heat Transfer in a Rib and Pin Roughened Rotating Multi-Pass Channel with Hub Turning Vane and Trailing-Edge Slot Ejection," *Journal of Thermal Science and Engineering Applications,* pp. 1-48, 2017.

[65] Won, S.Y., Mahmood, G.I., and Ligrani, P.M., "Flow Structure and Local Nusselt Number Variations in a Channel with Angled Crossed-rib Turbulators," *International Journal of Heat and Mass Transfer,* vol. 46, pp. 3153-3166, 2003.

[66] Li, W., Li. X., Yang, L., Ren, J., Jiang, H., and Ligrani, P., "Effect of Reynolds Number, Hole Patterns, and Hole Inclination on Cooling Performance of an Impinging Jet Array—Part I: Convective Heat Transfer Results and Optimization," *Journal of Turbomachinery, ASME,* vol. 139, pp. 1-11, 2017.

[67] Boyce, M. P., "An Overview of Gas Turbines," *Gas Turbine Engineering Handbook,* vol. Fourth Edition, pp. 3-88, 2012.

[68] Boyce, M.P., "Axial-Flow Turbines," *Gas Turbine Engineering Handbook,* pp. 385-425, 2012.

[69] Donghui, L., Xinlin, X., and Fengxian, S., "Numerical Study on Heat Transfer Characteristics of Gas Turbine Coated Blades," *Institute of Electrical and Electronics Engineers,* vol. 10, pp. 4244-4813, 2010.

[70] Elnady, T., Hassan, I., Kadem, L., and Lucas, T., "Cooling Effectiveness of Shaped Film Holes for Leading Edge," *Experimental Thermal and Fluid Science,* vol. 44, pp. 649-661, 2013.

[71] Hu, J., Kong, X., Li, Z., Zhang, Y., and Xu, J., "Experimental Investigation of Aerodynamic Interaction Between Tip Leakage Flow and Spontaneous Tip Injection Flow Using 2D-PIV," *Experimental Thermal and Fluid Science,* vol. 54, pp. 127-135, 2014.

[72] Johnson, B., Tian, W., Zhang, K., and Hu, H., "An Experimental Study of Density Ratio Effects on the Film Cooling Injection from Discrete Holes by Using PIV and PSP Techniques," *International Journal of Heat and Mass Transfer,* vol. 76, pp. 337-349, 2014.

[73] Khalil, A., Kayed, H., Hanafi, A., Nemitailah, M., and Habib, M., "Numerical Predictions of Three-Dimensional Unsteady Turbulent Film-Cooling for Trailing Edge of Gas-Turbine Blade Using Large Eddy Simulation," *Journal of Energy Resources Technology,* vol. 141, no. 4, pp. 1-12, 27 February 2019.

[74] Pu, J., Ke, Z.-Q., Wang, J.-H., You, H.-D., and Du, Z.-N., "An Experimental Investigation on Fluid Flow Characteristics in a Real Coolant Channel of LP Turbine Blade with PIV Technique," *Experimental Thermal and Fluid Science,* vol. 45, pp. 43-53, 2013.

[75] Yelishala, S.C., Kannaiyan, K., Wang, Z., Metghalchi, H., Levendis, Y.A., and Sadr, R., "Thermodynamic Study on Blends of Hydrocarbons and Carbon Dioxide as Zeotropic Refrigerants," *Journal of Energy Resources Thecnology,* vol. 142, no. 8, p. 082304, August 2020.

[76] Wang, Z., Bai, Z., Yu, G., Yelishala, S., and Metghalchi, H., "The Critical Pressure at the Onset of Flame Instability of Syngas/Air/Diluent Outwardly Expanding Flame at Different Initial Temperatures and Pressures," *Journal of Energy Rewsources Technology,* vol. 141, no. 8, p. 082207, 2019.

[77] Forghan, F., Askari, O., Narusawa, U., and Metghalchi, H., "Cooling of Turbine Blade Surface With Expanded Exit Holes: Computational Suction-Side Analysis," *Journal of Energy Resources Technology,* vol. 138, no. 5, p. 051602, September 2016.

[78] Phil Ligrani, "Heat Transfer Augmentation Technologies for Internal Cooling of Turbine Components of Gas Turbine Engines," *International Journal of Rotating Machinery,* pp. 1-33, 2013.

[79] Lee, J., Ren, Z., Ligrani, P., Fox, M., and Moon, H.-K., "Crossflows From Jet Array Impingement Cooling: Effects of Hole Array Spacing, Jet-to-Target Plate Distance, and Reynolds Number," *Proceedings of ASME Turbo Expo 2014: Turbine Technical Conference and Exposition,* 2014.

[80] Noot, M.J. and Mattheij, R.M.M., "Numerical Analysis of Turbine Blade Cooling Ducts," *Mathematical and Computer Modeling,* vol. 31, pp. 77-98, 2000.

[81] Hai-yong, L., Song-ling, L., Hang-fu, Q., and Cun-liang, L., "Aerodynamic Investigation of Impingement Cooling in a Confined Channel with Staggered Jet Array Arrangement," *Experimental Thermal and Fluid Science,* vol. 48, pp. 184-197, 2013.

[82] Hassan, O. and Hassan, I., "Experimental Investigations of the Film Cooling Heat Transfer Coefficient of a Micro-Tangential-Jet Scheme on a Gas Turbine Vane," *International Journal of Heat and Mass Transfer,* vol. 64, pp. 401-417, 2013.

[83] Galeana, D. and Beyene, A., "Gas Turbine Blade Heat Transfer and Internal Swirl Cooling Flow Experimental Study Using Liquid Crystals and Three-Dimensional Stereo-Particle Imaging Velocimetry," *Journal of Energy Resources Technology,* vol. 143, no. 10, pp. 102106-1-9, 2021.

[84] Wieneke, B., "Generic a-posteriori uncertainty quantification for PIV vector fields by correlation statistics," *17th International Symposium on Applications of Laser Techniques to Fluid Mechanics,* pp. 1-9, 07-10 July 2014.

[85] Aswalekar, U.V., Solanki, R.S., Kaul, V.S., Borkar, S.S., and Kambale, S.R., "Study and Analysis of Vortex Tube," *International Journal of Engineering Science Invention,* vol. 3, no. 11, pp. 51-55, 2014.

[86] Bazgir, A., "Ranque-Hilsch Vortex Tube : A Numerical Study," *2nd International Conference of Science & Engineering In the Technology Era,* 2017.

[87] Mebrat A.A., Galeana D., and Beyene A. , "Vortex cooling of a gas turbine blade: comparison of single and bidirectional swirl formation," *Proceedings of ECOS 2022 - The 35rth International Conference On Efficiency, Cost, Optimization, Simulation and Environment,* 2022.

[88] Galeana, D. and Beyene, A. , "Experimental Study of Swirl Cooling Flow on a Circular Chamber Using 3-D Stereo-PIV," in *Power & Energy Conference & Exhibition ASME*, Lake Buena Vista, FL, USA, 2018.